Effects of Manifold Deformation and Permeability on the Performance of the Flexible and Rigid Porous Stratification Manifolds for Solar Storage Tanks

A Dissertation
SUBMITTED TO THE FACULTY OF
UNIVERSITY OF MINNESOTA
BY

SHUPING WANG

IN PARTIAL FULFILLMENT OF THE REQUIREMENTS
FOR THE DEGREE OF
DOCTOR OF PHILOSOPHY

Adviser: Dr. Jane H. Davidson

December 2016

Acknowledgements

First of all, I would like to express my sincere gratitude to my advisor Prof. Jane H. Davidson for her continuous support of my Ph.D study and her patience and motivation. Her guidance in developing research ideas and in technical writing helped me immensely. I am grateful for her encouragement especially during tough times in completing the Ph.D. dissertation.

Besides my advisor, I would like to thank the rest of my thesis committee: Prof. Lian Shen, Prof. Ellen Longmire, and Prof. Vinod Srinivasan, for their insightful comments and encouragement. I would like to thank Prof. Ellen Longmire for sharing her knowledge and providing suggestions on Particle Image Velocimetry (PIV) measurement.

I thank my colleagues at the Solar Energy Lab, Dr. Brandon Hathaway, Dr. Peter Krenzke, Dr. Rohini Bala Chandran, Dr. Adam Gladen, Krishna Sandeep Prata, Daniel Nigon, Jesse Fosheim, Dr. Josh A. Quinnell, Dr. Luke Venstrom, Jason Mallinak, Tejas Ulavi, and many others, for the enjoyable time we spent and the help and suggestions you provided.

Lastly, I would like to thank my parents for their unconditional support. Thank you.

Dedication

I dedicate this dissertation to my family, whose unselfish support makes it possible for me to complete this work.

Abstract

Promoting and maintaining a high degree of thermal stratification in solar storage tanks has well documented benefits for increasing the solar energy gain from solar heating systems [1–3]. This dissertation investigated the flexible fabric porous manifold and rigid porous-tube manifold proposed and tested in prior studies [4–10] for stratification enhancement.

A mathematical model for the flexible fabric manifold is developed that accounts the interaction between the surrounding fluid in the tank and the flexible manifold wall. The relationship between the tube deformation and the pressure difference across the wall is described by the semi-empirical “tube law”. This manifold model provides a physical understanding of the working mechanism of the flexible fabric manifold and disapproves the widely held hypothesis that the deformation of the manifold is beneficial. Modeling results indicate that the dimensionless permeability can be optimized for improved performance.

Following above findings, the effect of dimensionless permeability on the performance of the rigid porous-tube manifold are investigated in conditions representative of residential solar hot water systems. 2-D CFD simulation of the charging process reveals that optimizing the selection of the dimensionless permeability can improve the effectiveness of the manifold by eliminating suction (during intermediate charging) and releasing the fluid in the upper portion of the tank (during top charging). Furthermore, I show that the 1-D manifold model provides adequate prediction of the

radial velocity distribution on the manifold wall compared with the results from the 2-D simulation. Therefore, the 1-D model can be used as an efficient design tool. With simulation results from the 1-D model over a wide range of the Richardson number and the dimensionless permeability, a design guideline for selection of the dimensionless permeability according to the Richardson number and the charging mode are developed. A prototype of the rigid porous-tube manifold is constructed and tested in comparison to conventional inlets. Temperature distribution in the tank is measured by thermocouple trees and the velocity field near the manifold is measured by a PIV system. For intermediate charging, the manifold achieves 0.5 dimensionless exergy efficiency after 90 minutes of charging, while the exergy efficiency for inlet diffuser and inlet pipe are 0.15 and 0, respectively. For top charging, the performance of the manifold is comparable to the best performing inlet diffuser. The measured velocity field is consistent to the model predication, indicating a 90% reduction of the suction rate during intermediate charging compared with conventional inlet pipe, and showing that the fluid is released approximately in the upper 25% of the tank during top charging.

Table of Contents

List of Tables

List of Figures

Chapter 1

Introduction

This dissertation is a collection of three research papers on porous thermal stratification manifolds used in solar storage tanks. Each paper, as a chapter, includes a literature review, a description of the method employed in the study, a presentation and discussion of the results, and a conclusion. Flexible fabric porous stratification manifolds and rigid porous-tube manifold are investigated through modeling and laboratory testing. Together, these papers present a validated design guideline for the porous-tube manifold over a wide range of operating conditions, and show that the flexibility of the fabric manifold does not provide any advantage over the rigid porous-tube manifold.

In the first chapter of this dissertation, section 1.1 provides an overall background related to prior numerical and experimental studies on various types of stratification manifolds. Section 1.2 describes the objectives of this dissertation, and section 1.3 presents an outline of the organization of this dissertation.

1.1 Background

Sensible heat liquid storage tanks remain the most widely used energy storage system for solar hot water and combined hot water and space heating systems due to low cost, reliability, and simplicity [11,12]. The typical volume of storage tanks ranges from several hundred liters for residential systems to tens of thousands of liters for large

commercial systems, for example, for hotels and food processing factories. There are two types of storage tanks: direct storage tanks, in which incoming fluid mixes with tank fluid directly, and storage tanks with internal heat exchangers. This dissertation focuses on inlet flow distributors, commonly referred to as stratification manifolds, used in direct storage tanks, which are widely used in solar thermal systems.

Within the storage tank, thermal stratification (defined as the stable layering of fluid at different temperatures) is desirable. Various studies [1,3,12–14] have shown that maintaining a high degree of stratification can improve the system performance by 6 – 38% in terms of the annual solar fraction, which is the percentage of energy demand met by the solar thermal system. The inlet temperature to the collector, which is drawn from the bottom of the tank, is lower. Consequently, the heat loss of the collector to the ambient is lower. Moreover, with hotter fluid at the top of the tank, the quality of the energy delivered to the user is improved.

For a direct storage tank, a stratification manifold is required in order to promote and maintain a high degree of stratification. The goal of the manifold is to release the incoming fluid at the level of neutral buoyancy, where the incoming fluid temperature equals to the tank temperature. The manifold also needs to prevent suction (entrainment) of the tank fluid into the manifold. The main challenge of designing a manifold is the operating condition of the tank including the inlet flow rate, inlet temperature, and tank temperature varies throughout the day because of the intermittent nature of solar irradiation and user consumption. Top charging occurs when the incoming fluid temperature is greater than the highest temperature in the tank. In this case, the incoming fluid should be introduced to the top of the tank to avoid mixing. Intermediate charging

occurs when the incoming fluid is warmer than that in the lower portion of the tank but is cooler than that in the upper portion. For this scenario, the fluid should be introduced between temperature layers in the tank. The designer of the manifold should consider both top charging and intermediate charging.

Various manifold designs have been proposed and tested in the last four decades, including rigid porous-tube manifold [9,10,15], flexible porous fabric manifolds [4–6,16,17], rigid porous manifolds with hydraulic resistance elements [4–6,16,17], vertical pipe with discrete horizontal openings with and without non-return valves [7,8,18,19].

Experimental tests suggest that a flexible fabric manifold has better or identical performance compared to the rigid porous manifold with hydraulic resistance elements [6,17] and vertical pipe with non-return valves [7,8] under both top charging and intermediate charging conditions. Despite promising performance, its working mechanism is poorly understood. In the prior descriptions of a fabric manifold [4,5], researchers suggested that the ability of the manifold to collapse or inflate depending on the pressure difference across the wall is the key characteristic that allows the fabric manifold to eliminate suction (entrainment) and to adapt to different charging conditions. However, there is a lack of theory to support this hypothesis. To address this issue, I developed a theoretical basis for fluid flow in a flexible manifold [20].

The rigid porous-tube manifold is conceptually a simpler design. It is constructed with an inlet diffuser and a rigid porous tube without internal hydraulic resistance elements. Prior to the present work, this manifold concept was not evaluated adequately. Prior studies [9,10] were largely limited in scope to the top charging. The behavior of a

porous tube under intermediate charging, and the effects of permeability on performance were investigated in the present work [21,22].

1.2 Objectives

The first objective of the present study is to provide a physical interpretation of the working mechanism of the flexible fabric manifold and to identify important design parameters using a mathematical model that correctly accounts the interaction between the fluid and the flexible manifold wall. The second objective is to develop a design guideline for the manifold through transient CFD simulations that account for the mixing process in the tank as well as the behavior of the manifold, focusing on key design parameters. The third objective is to validate the developed design guideline through prototype testing in comparison with conventional inlets.

1.3 Thesis Organization

Chapter 2 presents a one-dimensional model for the flexible fabric manifold. The model takes into account the interaction between the fluid and the elastic manifold wall using a “tube law” model [23,24]. The “tube law” provides a semi-empirical correlation between the local cross-sectional area of the manifold and the local pressure difference between and manifold and the tank. Modeling results show that contrary to the widely held hypothesis, the flexibility and the deformation of the flexible manifold do not have a significant impact on the manifold performance. The key design parameters are the dimensionless permeability, which represents the relative through-wall flow resistance, and the Richardson number, which represents the operating condition.

In chapter 3, transient CFD simulations of the charging process in a storage tank with a rigid porous-tube manifold are presented. In light of the finding in chapter 2., Chapter 3 focuses on the selection of the optimum permeability in terms of the manifold performance evaluated based on the dimensionless exergy efficiency. The 1-D porous-tube manifold model is compared to the 2-D CFD results with regards to the predicted radial velocity distribution across the manifold wall. The 1-D model provides adequate results in predicting manifold performance. A design guideline is developed through a parametric study using the 1-D model. The recommended range of dimensionless permeability for a wide range of Richardson number are presented for both top charging and intermediate charging.

Chapter 4 is experimental study of a rigid porous-tube manifold designed according to the developed design guideline to achieve a balanced performance under both top charging and intermediate charging. Vertical temperature distribution in the tank is measured using thermocouple trees, and the velocity field in a region adjacent to the manifold outer wall are measured using a particle image velocimetry (PIV) system.

Chapter 5 summarizes the findings from Chapters 2–4. Possible areas of future investigation are presented

Chapter 2

Fluid-Structure Interaction in the Flexible Porous Stratification Manifold

Abstract:

A model of the flexible porous manifold that captures the interaction between the flow field and the deformation of the manifold is developed and applied to understand how the fabric manifold works for conditions expected in solar water heaters. Contrary to the widely held hypothesis that the change of cross-sectional area induced by the fluid-structure interaction is beneficial, the numerical results demonstrate the change of cross-sectional area has no significant impact on the effectiveness of the manifold. In comparison to a rigid porous manifold, the performance of the flexible manifold is slightly worse because the collapse of the manifold encourages entrainment. The dimensionless permeability plays a crucial role in determining the performance and can be selected to limit entrainment and release fluid near the vertical level of neutral buoyancy.

2.1 Introduction

Promoting and maintaining a high degree of thermal stratification in the storage tank of solar thermal systems can improve the system level thermal performance and economics [1,3,12]. Stratification increases the energy and exergy available to serve the

Note: The content of this chapter was published as in Ref. [20]

load, increases collector efficiency by decreasing the inlet temperature, and can reduce pumping power by allowing optimization of the storage charging period. To achieve thermal stratification, a number of internal inlet flow distribution manifolds, including the rigid porous manifold with vertical hydraulic resistance elements [4,5,16,17,25], flexible porous manifolds [5–8], and rigid pipes with check valves [7,18], have been proposed and tested. The purpose of these devices is to release the fluid entering the tank at the vertical position of neutral buoyancy and to prevent entrainment of the fluid from the tank into the manifold. The behavior of the rigid porous manifold is well understood based on both modeling [5,25] and experiments [5,16,17,26]. Though there are a number of excellent experimental studies of the flexible porous manifold, its behavior is poorly understood, due in large part to the lack of a theoretical basis for understanding the fluid-structure interaction.

The typical flexible porous manifold is a straight tube made of fabric. It may be used in conjunction with an inlet diffuser to provide a uniform inlet velocity distribution. It has been postulated that the flexible manifold automatically forms a vertical cross-sectional area distribution that enforces a pressure balance across the fabric, thereby eliminating entrainment [5]. Based on this unproven hypothesis, the effectiveness of the flexible porous manifold has been thought to be insensitive to the operating conditions (i.e., inlet temperature and flow rate, and temperature distribution in the tank), unlike other manifolds with rigid structures. As demonstrated experimentally [5–7], the hydrodynamic stress exerted on the flexible tube can deform the tube. Even though the concept was initially proposed over thirty years ago [4], there has been little progress toward understanding the interaction between the flow field and the deformation of the

tube, and there is no theoretical basis for selection of the key design parameters such as flexibility and permeability of the fabric.

In this study, we develop a model of the flexible porous manifold and use it to illustrate how the manifold works for conditions expected in practice. The conservation equations of mass, momentum, and energy are derived following the one-dimensional theory of flows in channels of variable cross-sectional area [27]. The relationship between the cross-sectional area and the differential pressure across the manifold surface is described by the "tube law" [23], which provides closure to the model. We investigate how the change of cross-sectional area induced by the fluid-structure interaction affects the effectiveness of the manifold for a range of permeability, and show the pressure-matching hypothesis is incorrect.

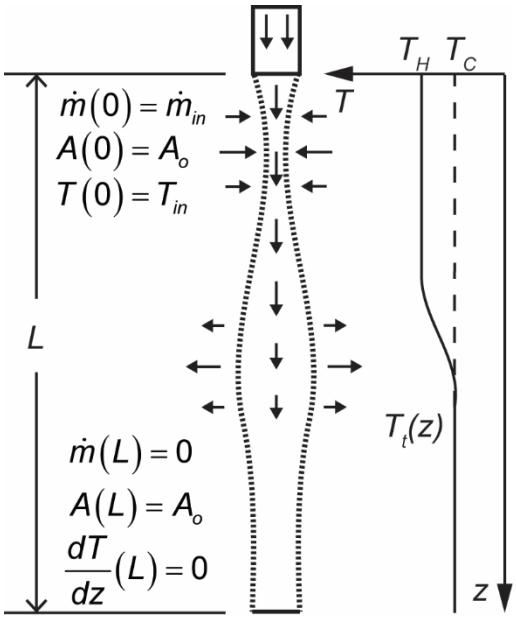

Figure 2.1 One-dimensional flexible manifold model domain. The dash line represents the fabric porous wall. The solid line represents the attached inlet pipe and solid bottom of the manifold. The arrows illustrate the direction of the flow.

2.2 Theoretical Development

We consider the tank configuration shown in Fig. 2.1. The manifold is assumed to be a flexible porous tube of length L, undeformed diameter D, thickness δ, and permeability K. It is installed vertically in a water storage tank with known distributions of pressure $p_t(z)$ and temperature $T_t(z)$. Heated water at temperature T_{in} and mass flow rate $\dot{m}_{in}$ enters the top of the manifold at $z = 0$ and descends into the porous tube. The water exits the tube in the radial direction; the lower end of the tube at $z = L$ is sealed, and assumed impermeable and insulated. The velocity through the wall is controlled by the pressure drop ($\Delta p = p - p_t$). When Δp is positive, the fluid in the manifold flows through the wall into the tank, and conversely when Δp is negative, the fluid from the tank is sucked (entrained) into the manifold. Entrainment is always undesirable as it creates mixing within the manifold. Ideally, the outward radial flow occurs only in a narrow region at the height of neutral buoyancy. In the model, the manifold is allowed to deform freely except at the top ($z = 0$) and the bottom ($z = L$), where the tube is assumed to be clamped in place. The cross-sectional area of the manifold A varies along the length of the tube in response to the change in Δp.

To model the behavior of such a manifold, one must consider the coupled fluid conservation equations for mass, momentum, and energy, and the equation describing the relationship between cross-sectional area and differential pressure, which is referred to as the ‘tube law’. The conservation equations for mass, momentum, and energy are derived following the one-dimensional theory of flows in channels of variable cross-sectional area [27]. The 1-D steady model is consistent with approach used by Sharp and Loehrke

in their original proposal and theoretical model of the fabric stratification manifold [5,17]. It assumes the velocity, pressure, and temperature depend on height but are uniform circumferentially at each vertical position. The hydrostatic pressure and temperature distribution in the tank are held constant, assuming the volume of the tank is much greater than the volume of the manifold. The model allows us to investigate the fluid-structure interaction in flexible tubes without a full 3-D model of the transient flow in the tank. Specifically, the model predicts the shape of the tube in terms of $A(z)$ and the vertical distribution of the radial flow in and out of the manifold. The location and magnitude of the flow into and out of the tank are indicators of mixing used to judge the relative performance of flexible and rigid porous manifolds. The model allows us to answer the fundamental question whether deformation of the manifold is beneficial to controlling the flow rate. It also allows us to conduct a parametric study to identify important attributes (dimensionless parameters) that affect the behavior of the manifold.

Mass conservation is given by

$$\frac{d\dot{m}}{dz} = \begin{cases} -2\sqrt{\pi A_o}\,\dfrac{\rho_{in} K}{\mu}\dfrac{\Delta p}{\delta}, A \le A_o \\ -2\sqrt{\pi A}\,\dfrac{\rho_{in} K}{\mu}\dfrac{\Delta p}{\delta}, A > A_o \end{cases} \tag{2.1}$$

where A_o is the cross-sectional area when the tube is undeformed. The radial flow through the wall is described by the Darcy's law and is a function of height. An important assumption of Eq. (2.1) is that when the tube collapses ($A \le A_o$), the perimeter and permeability do not change. The assumption is reasonable because deformation is primarily due to transverse bending as the tube collapses [24]; there is no appreciable torsion, in-plane shear or tensional stresses. Moreover, the local curvature is normally

much greater than the length scale of the fabric pattern. Therefore, the structure of the fabric (e.g. the orientation and spacing of the yarns in the woven or knitted pattern) does not change. When the tube inflates, it is stretched and the diameter increases, but for most fabrics, the change in permeability can be neglected. Studies on fabric permeability [28–31] show the permeability is approximately linear to the porosity. Assuming the fiber/yarn is incompressible (i.e. the solid volume does not change as the manifold inflates), the porosity is proportional to the square root of the cross-sectional area. The predicted area increase, as discussed in the results section, is less than 20% for the majority of the cases. Correspondingly, the increase of porosity and permeability is less than 10%. Thus, we make the reasonable assumption that the change in permeability is negligible.

The 1-D momentum equation is

$$\frac{d\Delta p}{dz} = \left(\rho - \rho_t\right) g - \frac{\dot{m}}{\rho_{in} A^2}\frac{d\dot{m}}{dz} + \frac{\dot{m}^2}{\rho_{in} A^3}\frac{dA}{dz} \tag{2.2}$$

The first term on the right hand side captures the effect of buoyancy. The second and third terms represent the effects of flow through the porous wall and the change of cross sectional area on the momentum balance. Wall friction is neglected.

The interaction between the fabric and the surrounding fluid is described by an empirical “tube law”, given by Eq. (2.3). The “tube law” has been used widely to represent the relationship between Δp and cross sectional area for flows in collapsible tubes [24,32,33].

$$\Delta p = \mathrm{P}(A) - F_o \frac{d^2 A}{dz^2} \tag{2.3}$$

The first term on the right hand side represents the contribution of the tube's transverse stiffness, commonly referred to as the "local tube law" [24]. The "local tube law" P(A) can be determined empirically [34–36] or derived from theory [23]. As illustrated in Fig. 2.2 [24], when $\Delta p > 0$, the tube inflates symmetrically (state (a)). Because inflation requires stretching, a large Δp is necessary to inflate the tube. Thin-walled tubes can only support a limited compression load. With a small negative Δp the tube collapses into an ellipse (state (b)). When Δp is reduced below a critical value Δp_b, the tube may buckle forming a non-circular shape with two or more lobes [10, 26] (state (c)). In the buckling state, a small change in Δp can induce a large change in A because transverse bending is the dominant mechanism for deformation. If Δp is less than a second critical value ($\Delta p < \Delta p_c$), the opposite walls contact each other. The stiffness of the tube increases drastically. As a result, substantially greater compression loads are required to further reduce the cross-sectional area (state (d)).

The second term on the right hand side of Eq. (2. 3) represents the effect of the axial elasticity of the tube, which is proportional to the initial axial stretching force F_o [36]. For the limiting case of $F_o = 0$, tube deformation is determined by the "local tube law". A higher F_o leads to a less compliant tube because both ends of the tube are fixed in place.

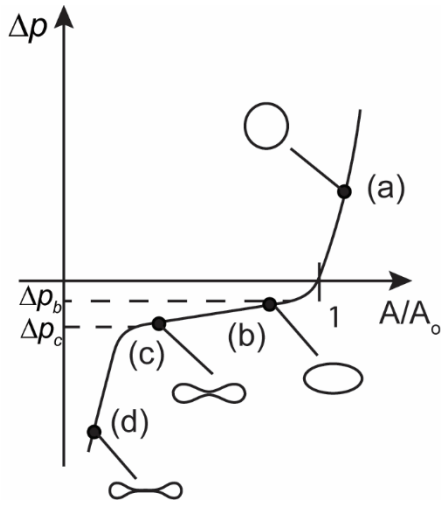

Figure 2.2 Illustration of local tube law [23]. Subplots on the curve are the corresponding tube shapes.

For long thin-walled ($D/L >> 1$ and $\delta/L << 1$) elliptical tubes, the tube law derived from the thin shell theory is given by [23]

$$\Delta p = S_e\left(\frac{A}{A_o}-1\right)-F_e\frac{d^2}{d^2 z}\left(\frac{A}{A_o}\right) \tag{2.4}$$

The effective stiffness S_e and effective axial pre-stretching F_e are given by

$$S_e = \frac{8k_o S_j}{D^3},\ \ j = c,b,i \tag{2.5}$$

where *c* represents the contact state, *b* represents the buckling state, *i* represents the inflated state, and

$$F_e = \frac{k_2 F_o}{2\pi}. \tag{2.6}$$

The dimensionless parameters k_o and k_2 are related to the eccentricity (minor radius/major radius) of the tube. For nearly circular tubes, these parameters are [23]

$$k_o = e^{4\sigma_o} \tag{2.7}$$

$$k_2 = \frac{5}{36} e^{4\sigma_o} \tag{2.8}$$

where σ_o is the eccentricity factor. For a circular tube, $\sigma_o \to \infty$. Hence, a circular tube is infinitely stiff based on this model. To model a manifold that is approximately circular and yet flexible, we choose $\sigma_o = 1.45$. The corresponding eccentricity is 0.90.

If linear elastic behavior is assumed, in the buckling state, the (bending) stiffness S_b for a thin-walled tube is

$$S_b = \frac{E\delta^3}{12(1-\nu)} \tag{2.9}$$

where E is the Young's modulus and υ is Poisson's ratio. In the inflated state and in the contact state, the manifold is more resistant to deformation, and the effective stiffness S_e is much higher. Lacking data, we assume $0 \le A \le 0.3A_o$ is the contact region. We assume the stiffness in the contact state and the inflated state are an order of magnitude larger than the bending stiffness in the buckling state, similar to what is reported for thin-walled latex tubes [34,36].

The energy conservation equation includes convection through the wall, and the axial conduction within the fluid.

$$\frac{dT}{dz} = \begin{cases} \dfrac{Ak_f}{\dot{m}c_p}\dfrac{d^2T}{dz^2}, & \Delta p \ge 0 \\ -\dfrac{(T-T_t)}{\dot{m}}\dfrac{d\dot{m}}{dz} + \dfrac{Ak_f}{\dot{m}c_p}\dfrac{d^2T}{dz^2}, & \Delta p < 0 \end{cases} \tag{2.10}$$

The thermophysical properties of the fluid are evaluated based on the inlet temperature. The inclusion of the conduction is mainly to raise the order of the equation, so that

additional boundary conditions can be applied at the end of the manifold domain ($z = L$). Physically, the heat transfer is dominated by convection.

The boundary conditions at the top inlet $z = 0$ are

$$\dot{m} = \dot{m}_{in} \ , T = T_{in} \, , \ A = A_o \tag{2.11}$$

and at the lower end of the manifold are

$$\dot{m} = 0 \ , \frac{dT}{dz} = 0 \, , \ A = A_o \tag{2.12}$$

Nondimensionalization of the governing equations provides insight to the physics of the problem. The following dimensionless variables are used to derive the dimensionless governing equations:

$$\dot{m}^* = \frac{\dot{m}}{\dot{m}_{in}} ; z^* = \frac{z}{L} ; \ T^* = \frac{T - T_C}{T_H - T_C} ; \ P^* = \frac{p - p_t}{\dot{m}_{in}^2 / \rho_{in} A_o^2} ; A^* = \frac{A}{A_o} \tag{2.13}$$

The dimensionless mass conservation equation is

$$\frac{d\dot{m}^*}{dz^*} = \begin{cases} -\tilde{K} P^* , A^* \le 1 \\ -\tilde{K} \sqrt{A^*} P^* , A^* > 1 \end{cases} \tag{2.14}$$

In this expression, the dimensionless permeability of the manifold is defined as:

$$\tilde{K} = \frac{2\sqrt{\pi A_o} K \dot{m} L}{\mu A_o^2 \delta} = \frac{\dot{m}_{in}^2 / \rho_{in} A_o^2}{\mu \delta \bar{u} / K} \tag{2.15}$$

Here $\bar{u}$ is the average Darcy velocity through the manifold wall based on the inlet mass flow rate,

$$\bar{u} = \frac{\dot{m}_{in}}{2\sqrt{\pi A_o} L \rho_{in}} \tag{2.16}$$

In essence, $\bar{u}$ is the velocity if the radial flow is uniform over the entire manifold surface. Accordingly, the denominator of Eq. (2.15), $\mu\delta\bar{u}/K$, represents a differential pressure scale in the radial direction. The numerator $\dot{m}_{in}^2/\rho_{in}A_o^2$ is the scale of the pressure drop in the axial direction because the buoyancy eventually overcomes the vertical momentum of the incoming flow. According to the theory of diffuser design [37], if $\tilde{K} \ll 1$, the radial flow distribution over the entire height will be uniform. As $\tilde{K}$ is increased, a larger portion of the incoming fluid will be released in a thinner vertical band near the level of neutral buoyancy and the radial flow will vary along the height of the tube.

The non-dimensional momentum equation is given by Eq. (2.17):

$$\frac{dP^*}{dz^*} = Ri_L\left(T_t^* - T^*\right) - \frac{\dot{m}^*}{A^{*2}}\frac{d\dot{m}^*}{dz^*} + \frac{\dot{m}^{*2}}{A^{*3}}\frac{dA^*}{dz^*} \tag{2.17}$$

For buoyancy dominant flows (i.e., for Richardson number $Ri_L = \frac{\rho_{in}^2 g A_o^2 L \beta_{in}\left(T_H - T_C\right)}{\dot{m}_{in}^2}$ >>1), the flow through the porous wall and the change of cross-sectional area are expected to have little impact on the momentum balance and ultimately pressure distribution in the manifold. For the range of flow rates used for solar water heating systems, Ri_L is on the order of 100 or larger.

The dimensionless tube law is given by

$$P^* = \tilde{S}\left(A^* - 1\right) - \tilde{F}\frac{d^2A^*}{d\left(z^*\right)^2} \tag{2.18}$$

where the dimensionless stiffness $\tilde{S} = \frac{S_e \rho_{in} A_o^2}{\dot{m}_{in}^2}$ is the ratio of transverse stiffness of the manifold and kinetic energy of the inlet flow. The dimensionless axial pre-stress

$\tilde{F} = \dfrac{F_e \rho_{in} A_o^2}{L^2 \dot{m}_{in}^2}$ is the ratio of axial pre-stress and kinetic energy of the inlet flow. The tube stiffness increases with increasing $\tilde{S}$ and $\tilde{F}$. For elastic knit fabrics, for example, a full plating single Jersey knit fabric with elastic fiber [38], $\tilde{S}$ = 100 (E = 40 kPa). We consider $20 \leq \tilde{S} \leq 2000$, covering a range for extremely elastic fabrics to densely knit or woven fabrics that are less flexible. In the prior experiments [5–7], the flexible manifolds were installed without substantial axial stretching force. Thus, we consider $\tilde{F}$ between 0.05 and 5, representing a small axial pre-stretching effect.

The dimensionless equation for energy conservation is

$$\frac{dT^*}{dz^*} = \begin{cases} \dfrac{A^*}{Pe_L \dot{m}^*} \dfrac{d^2 T^*}{d\left(z^*\right)^2}, P^* \geq 0 \\ -\dfrac{\left(T^* - T_t^*\right)}{\dot{m}^*} \dfrac{d\dot{m}^*}{dz^*} + \dfrac{A^*}{Pe_L \dot{m}^*} \dfrac{d^2 T^*}{d\left(z^*\right)^2}, P^* < 0 \end{cases} \tag{2.19}$$

where $Pe_L = \dfrac{\dot{m}_{in} c_p L}{A_o k_f}$ is the Peclet number. For typical flow rates, the convective heat transfer is much greater than the conductive heat transfer and $Pe_L >> 1$.

The dimensionless boundary conditions at $z^* = 0$ are

$$\dot{m}^* = 1,\ A^* = 1,\ T^* = T_{in}^* \tag{2.20}$$

and at $z^* = 1$ are

$$\dot{m}^* = 0, A^* = 1,\ \frac{dT^*}{dz^*} = 0 \tag{2.21}$$

The dimensionless temperature distribution in the tank $T_t^*\left(z^*\right)$ is prescribed as

$$T_t^* \equiv \frac{T_t - T_C}{T_H - T_C} = \frac{1}{1+\exp\left[a\left(2z^* - 1\right)\right]} \tag{2.22}$$

where the coefficient (a) controls the thickness of the thermocline. In this study, a is set to 10, which is representative of conditions in prior experimental studies in which that tank was stratified in two temperature zones [5,6].

The governing equations (Eqs. 2.14, 2.17-2.19) are first converted to a set first order differential (ODE) equations and then solved using the MATLAB ODEs solver—'bvp4c'. The maximum mesh size is set to 2000 and the absolute and relative tolerances are 1×10^{-6} and 1×10^{-3}, respectively.

Table 2.1 Physical parameters used in the model and the ranges of the dimensionless parameters

Physical parameters	**Symbol**	**Value**
Manifold inner diameter	D	0.0762 (m)
Manifold height	L	1 (m)
Manifold wall thickness	δ	0.001 (m)
Manifold permeability	K	4.5×10^{-12} – 4.5×10^{-10} (m^2)
Young's modulus	E	8 - 800 (kPa)
Poisson's ratio	v	0.4
Eccentricity factor	σ_o	1.45
Axial pre-stretching force	F_o	6.5×10^{-4} – 0.18 (N)
Operating conditions	**Symbol**	**Value**
Temperature of the bottom half of the tank	T_C	20 (℃)
Temperature of the top half of the tank	T_H	50 (℃)
Temperature of the inlet	T_{in}	35 (℃)
Inlet mass flow rate	$\dot{m}_{in}$	0.068 – 0.135 (kg/s)
Dimensionless parameters	**Symbol**	**Value**
Stiffness	$\tilde{S}$	20 – 2000
Axial pre-stress	$\tilde{F}$	0.05 – 5
Permeability	$\tilde{K}$	0.005 – 0.5
Richardson number	Ri_L	100 – 400
Peclet number	Pe_L	9645

2.3 Results

Table 2.1 lists the values of the physical parameters and operating conditions as well as the values of the corresponding dimensionless parameters considered in the present study. As shown in Fig. 2.1, the manifold is 1 m long with a 0.0762 m diameter. The thickness of the fabric is 1 mm. The original shape of the manifold is elliptical with an eccentricity of 0.90 ($\sigma_o = 1.45$). The Young's modulus E of elastic knitted fabrics is on the order of 10 kPa [38], and we investigate $8 \leq E \leq 800$ kPa, representing extremely elastic fabrics to non-stretchy fabrics. Poisson's ratio does not change significantly for different knit fabrics [38], and is assumed to be 0.4. The permeability K of the fabrics that have been considered in prior work [5–7] was not reported. Considering fabrics used for filtration applications [39], we consider $4.5\times10^{-12} \leq K \leq 4.5\times10^{-10}$ m^2. This range is relevant to a wide range of fabrics. As an example, the permeability of a plain-woven nylon monofilament fabric with 14% opening area and 45μm yarn diameter is 2×10^{-12} m^2 [39].

The manifold is simulated for solar charging of a stratified water storage tank. The tank is stratified into two equal volumes, each with uniform temperature with T_H = 50℃ and T_C = 20℃. The inlet water is at an intermediate temperature T_{in} = 35℃. Based on a representative flow rate for conventional solar collectors (0.015 kg/s/m^2) and 4.5 m^2 collector area (for a residential application) [40], the inlet flow rate for a base case is 0.068 kg/s and $Ri_L = 400$. We also simulate cases for $100 \leq Ri_L \leq 400$, where the effect of the change of cross-sectional area is expected to be greater as can be seen in Eq. (2. 17). A system with a lower flow rate than the conventional range will have a greater

Richardson number, a greater dimensionless stiffness as well as axial press-stress. For this reason, the effect of the manifold deformation and the magnitude of the deformation are expected to be much smaller than a system with conventional or higher flow rate.

The magnitude of the relevant dimensionless parameters, namely, the dimensionless stiffness $\tilde{S}_b$, the dimensionless axial pre-stress $\tilde{F}$, the dimensionless permeability $\tilde{K}$, and the Richardson number Ri_L each play an important role in determining the deformation of the manifold. Figure 2.3 illustrates the effects of these parameters on the dimensionless area A^* ratio along the height of the manifold for a baseline case. The baseline case is representative of a conventional operating flow rate for a hot water heating system (Ri_L = 400, $\dot{m}_{in}$ = 0.068 kg/s), and an elastic ($\tilde{S} = 20$, E = 8 kPa), moderately permeable fabric ($\tilde{K} = 0.1$, $K = 9\times10^{-11}$ m^2) which is installed in the tank without significant axial pre-stretching ($\tilde{F} = 0.05$, $F_o = 6.5\times10^{-4}$ N). Under these conditions, the manifold is most compliant within the range of the parameters investigated. To show the effects of each dimensionless parameter, one parameter is varied from the baseline case in each subplot of Fig. 2.3.

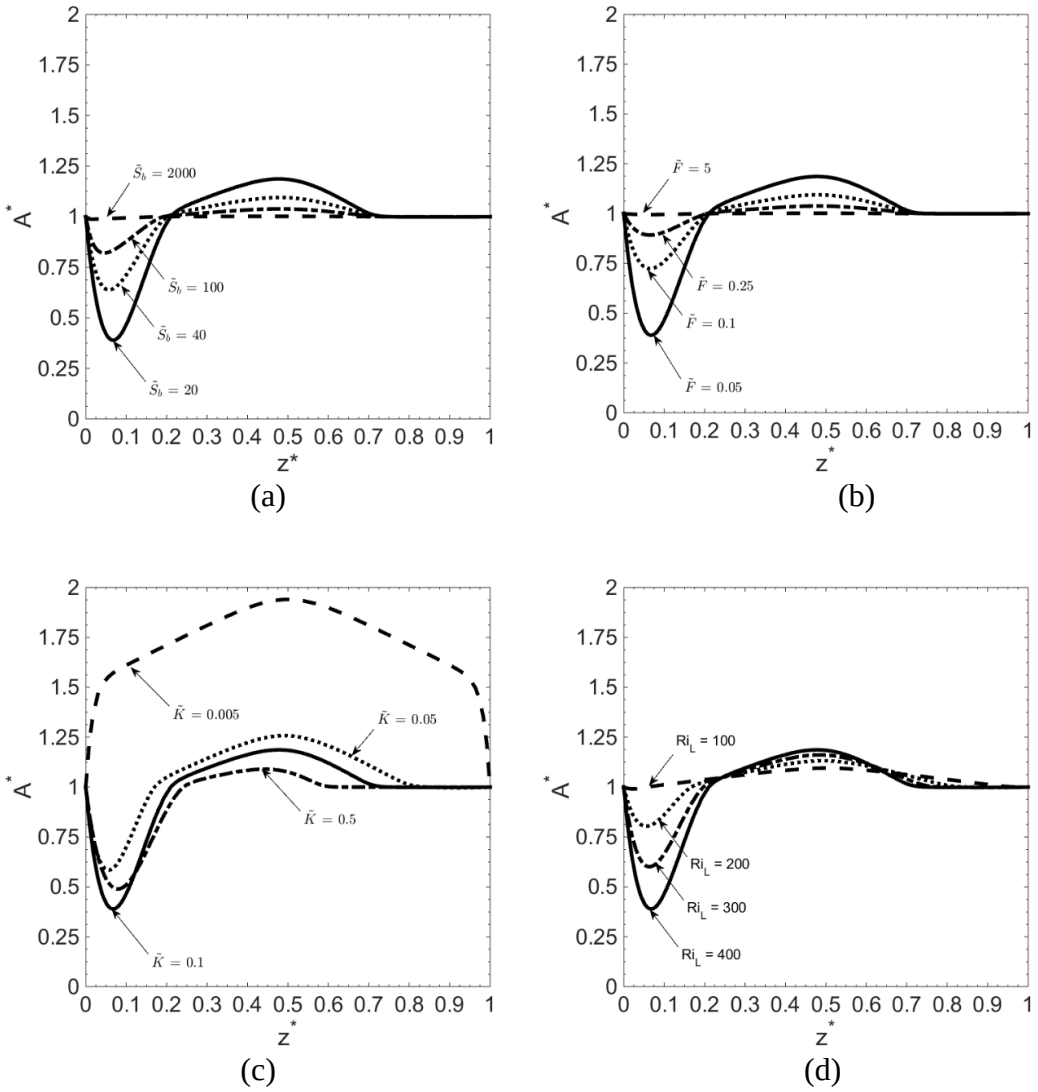

Figure 2.3 Dimensionless cross-sectional area A^* change vs. dimensionless axial position z^*: (a) effect of dimensionless stiffness $\tilde{S}$; (b) effect of dimensionless axial pre-stress $\tilde{F}$; (c) effect of dimensionless permeability $\tilde{K}$; (d) effect of Richardson number Ri_L.

Figure 2.3(a) shows the effect of the dimensionless stiffness $\tilde{S}_b$ at the buckling state on deformation. The inlet of the manifold is at $z^* = 0$. The level of neutral buoyancy is at $z^* = 0.5$ and the bottom of the manifold is at $z^* = 1$. Overall, the predicted shape of this manifold is consistent to prior experimental observations [5,6]. For values of $\tilde{S}_b <$

2000, the manifold collapses in the region close to the inlet and inflates in the mid-section, where the fluid in the manifold is neutrally buoyant with respect to the fluid in the tank. The bottom section of the manifold is not deformed, indicating the manifold and tank pressure are balanced. The area change due to inflation is smaller than that due to collapse because the dimensionless stiffness $\tilde{S}_b$ is much greater in the inflated state than in the buckling state. For $\tilde{S}_b = 20$, the manifold collapses substantially, reaching a minimum A^* = 0.38 (62% reduction in cross-sectional area) at z* = 0.08. The maximum inflation is approximately 20% (A^* = 1.2) at z^* = 0.5. Increasing $\tilde{S}_b$, which can be achieved by increasing the Young's modulus E of the fabric, reduces the magnitude of deformation. For instance, at $\tilde{S}_b = 100$ (E = 40 kPa), which represents a full plating single Jersey knit fabric with elastic fiber [38], the minimum and maximum A^* are 0.81 and 1.05, respectively. At $\tilde{S}_b = 2000$ (E = 800 kPa), the manifold is not deformed. The properties of the yarn and the fabric pattern determine the Young's modulus of the fabric. In general, knitted fabrics have a lower modulus compared to woven fabrics, which typically have E ~ O(1MPa) or greater [41]. Therefore, even though woven fabric is in general thinner than knitted fabric, the dimensionless stiffness $\tilde{S}_b$ is much greater. The simulation predicts manifolds made of woven fabrics are unlikely to deform under operating conditions of solar water heaters. This result is consistent with prior tests of fabric manifolds under similar operating conditions [6].

The influence of the axial pre-stress on deformation was not addressed in prior experimental characterization of flexible manifolds [7, 9, 10] and thus direct comparison

of this parameter to prior experiments is not possible. The numerical results presented in Fig. 2.3(b) indicate that deformation of the manifold is extremely sensitive to the dimensionless axial pre-stress $\tilde{F}$, which for a specific inlet flow rate and manifold geometry is determined by the axial pre-stretching force F_o. With $\tilde{F} = 5$ (F_o = 0.18 N), the manifold does not deform. Only for $\tilde{F} < 0.1$ ($F_o < 1.3\times10^{-3}$ N) is considerable deformation (>25% change of A^*) observed. From this result, we conclude that even a highly elastic fabric manifold will only deform if it is installed without axial stretching.

The dimensionless permeability $\tilde{K}$ affects the distribution of the differential pressure P^*, which is the driving force for deformation. The range of the dimensionless permeability investigated ($0.005 \leq \tilde{K} \leq 0.5$ or $4.5\times10^{-12} \leq K \leq$ to 4.5×10^{-10} m^2) represents relatively low permeable fabrics (e.g. a monofilament woven fabric with <4% opening area [39]) to highly permeable fabrics (e.g. a monofilament woven fabric with >38% opening area [39]). As shown in Fig. 2.3(c), for low permeability, i.e. $\tilde{K} = 0.005$ ($K = 4.5\times10^{-12}$ m^2), the entire manifold inflates, indicating a higher pressure in the manifold than in the tank, $P^*>0$. The maximum inflation occurs at $z^* = 0.5$, and is associated with a 95% larger cross-sectional area, equivalent to a 40% increase in the diameter of the tube. For $\tilde{K}$ from 0.05 to 0.5 ($K = 4.5\times10^{-11}$ to 4.5×10^{-10} m^2), the manifold collapses near the inlet, inflates in the mid-section, and remains undeformed at the bottom. The degree of inflation decreases monotonically with an increase of $\tilde{K}$ from 0.005 to 0.5. These results suggest that the dimensionless permeability will impact the radial flow ($d\dot{m}^*/dz^*$) distribution.

The impact of Richardson number Ri_L, which is the ratio of potential energy due to thermal buoyancy and the kinetic energy of the flow, on deformation is shown in Fig. 2.3(d). All four cases represent buoyancy dominated flows (i.e. Ri_L >>1). The results show that Ri_L has a crucial impact on manifold deformation. A lower Ri_L leads to less deformation (both collapse and inflation). For example, at Ri_L =100, A^* changes less than 10% over the height of the manifold. In comparison, for the baseline case Ri_L = 400, the manifold cross sectional area decreases by 62%. In the upper portion of the manifold, negative buoyancy ($T^* < T_t$) leads to a negative differential pressure that causes the manifold to collapse; in the lower portion of the manifold, positive buoyancy ($T^* > T_t$) creates a positive differential pressure that inflates the manifold. Higher Richardson numbers will yield larger deformation.

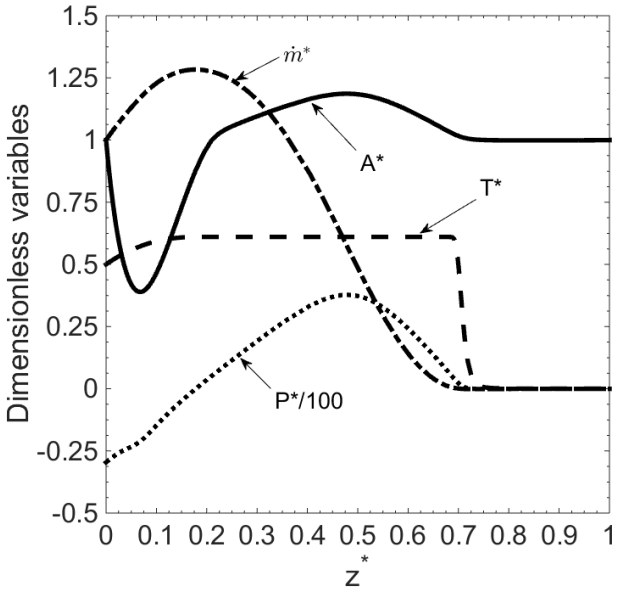

Figure 2.4 Predicted manifold performance for the baseline case. The dimensionless stiffness $\tilde{S}$ =20, the dimensionless axial pre-stress $\tilde{F}$ =0.05, the dimensionless permeability $\tilde{K}$ =0.1, and the Richardson number Ri_L = 400.

The previously held hypothesis is that the flexible manifold works based on a "pressure matching" mechanism [5–7], which requires the manifold to change its cross-sectional area to equalize the differential pressure across the wall. To test this hypothesis, we examine the baseline case for a very compliant manifold ($\tilde{S}_b = 20$, $\tilde{F} = 0.05$, $\tilde{K} = 0.1$, and $Ri_L = 400$). In Figure 2.4, the manifold cross-sectional area (A^*), differential pressure (P^*), axial flow rate ($\dot{m}^*$), and temperature (T^*) are plotted for this case. The values of P^* are scaled by 100 for better visualization. Although the manifold collapses significantly (over 62%), considerable suction, about 30% of the inlet flow rate, occurs. The manifold is clamped on a rigid tube at the inlet, $A^* = 1$ at $z^* = 0$. The manifold collapses increasingly along the flow direction z^*, reaching a minimum at approximately $z^* = 0.075$. At this height, A^* equals 0.38. Hence the manifold is likely to buckle into two or more lobes (refer to Fig. 2.2) and collapses nearly completely when $A^* \leq 0.3$. From $z^* = 0.075$ to 0.20, A^* increases and returns to the undeformed shape ($A^* = 1$). Between $z^* = 0.2$ and 0.73, the manifold inflates. The bottom of the manifold $z^* = 0.73$ to 1 is not deformed. The differential pressure P^* is lowest at the inlet, and increases along the flow direction z^* due to negative buoyancy ($T^* < T_t$). The manifold and tank pressure are balanced ($P^* = 0$), at $z^* \approx 0.18$. The slight mismatch between this height and the location where the manifold transitions from a collapsed state to an inflated state ($z^* = 0.2$) is due to the axial pre-stress. The manifold cross-sectional area is determined by the local differential pressure only if it is free of axial pre-stress ($\tilde{F} = 0$). In the mid-section of the manifold, $z^* = 0.2$ to 0.72, the manifold pressure is higher than the tank pressure. In the bottom region, $0.72 \leq z^* \leq 1$, the differential pressure is zero. The axial flow rate $\dot{m}^*$ increases if suction

occurs and decreases if manifold fluid is released into the tank. The buoyant plume creates suction in the region where the manifold collapses ($P^* < 0$). Suction stops at $z^* = 0.18$, and $\dot{m}^*$ increases to 1.3. The suction flow rate is about 30% of the inlet flow rate. In the mid-section, where the manifold inflates ($P^* > 0$), manifold fluid is released into the tank. But suction leads to mixing between the tank fluid and the incoming fluid. As a result, T^* increases from 0.5 at the inlet to 0.63 at $z^* = 0.18$, where suction stops. The sharp decrease in T^* at $z^* = 0.72$ represents the transition between the warmer incoming fluid and the cooler fluid at the bottom of the manifold, equal to the temperature in the bottom half of the tank. The bottom portion of the manifold does not deform.

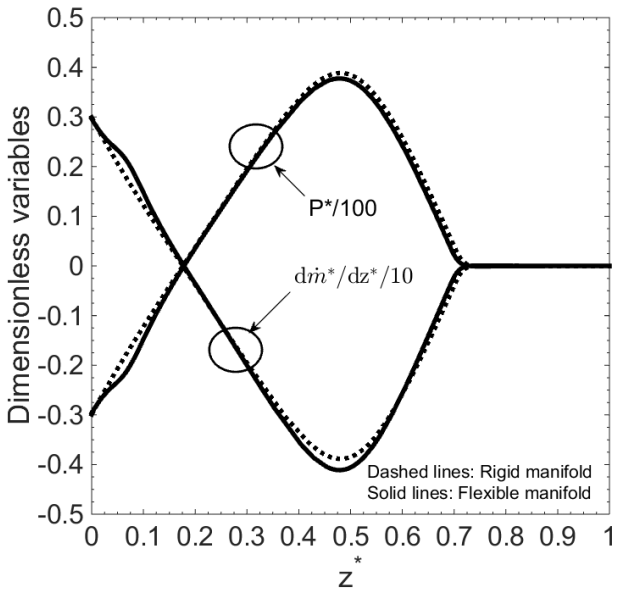

Figure 2.5 Comparison of dimensinless differential pressure P^* and the dimensionless radial flow distribution $d\dot{m}^* / dz^*$ between the flexible manifold and the rigid manifold

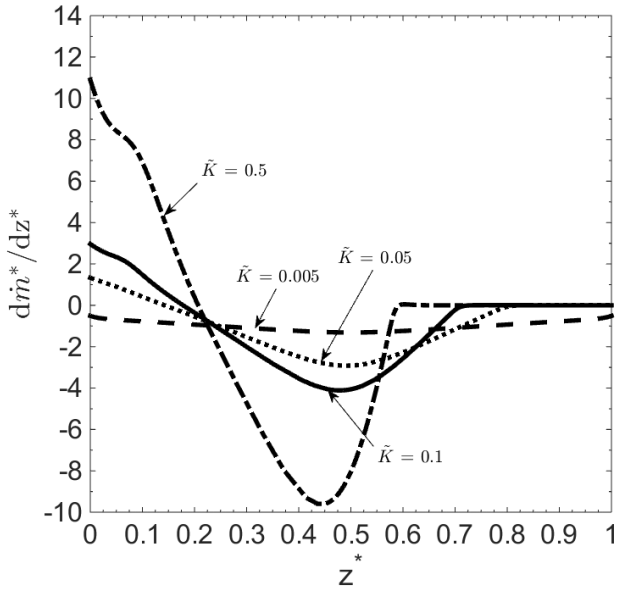

Figure 2.6 The effect of dimensionless permeability $\tilde{K}$ on the dimensionless radial flow distribution $d\dot{m}^*/dz^*$

The performance of the flexible manifold is compared to a rigid ($\tilde{S} \to \infty$ and $\tilde{F} \to \infty$) porous manifold with the same permeability $\tilde{K}$ = 0.1 and Richardson number Ri_L = 400. The distribution of $d\dot{m}^*/dz^*$ and P^* for the flexible and rigid manifold are compared in Fig. 2.5. The performance of the manifold is determined by its radial flow distribution $d\dot{m}^*/dz^*$. Ideally, all the incoming fluid should be released near the level of neutral buoyancy (z^* = 0.5) without any suction (i.e., $d\dot{m}^*/dz^* < 0$). The performance of the flexible manifold is close to that of the rigid porous manifold except near the inlet where entrainment is worse. The collapse of the manifold leads to a lower P^* that results in more suction. For $0.075 \le z^* \le 0.2$, the cross-sectional area increases from minimum and P^* gradually converges to that for the rigid manifold. This effect is similar to the Bernoulli effect in a converging-diverging flow channel. In the mid-section of the

manifold, the radial flow rate for the flexible manifold is higher than that for the rigid manifold because of greater suction.

The effect of dimensionless permeability $\tilde{K}$ is illustrated in Fig. 2.6, which shows the radial flow distribution along the manifold height. For a low permeability fabric ($\tilde{K}$ = 0.005), the manifold behaves like a diffuser, releasing the manifold fluid over the entire height at a constant radial flow rate. This result is expected because according to the theory of diffuser design [37], the uniformity of the radial flow along the flow direction (z^*) increases as the ratio of the axial pressure drop and the radial pressure drop (the differential pressure) decreases. This ratio is represented by the dimensionless permeability $\tilde{K}$. With a higher dimensionless permeability, a larger portion of the incoming fluid is released at the right level. For instance, with $\tilde{K}$ = 0.05 and 0.5, the manifold fluid is released between z^* = 0.2 and 0.81 and between z^* = 0.2 and 0.6, respectively. However, suction rate increases as the manifold becomes more permeable. At the inlet z^* = 0, the suction rate for $\tilde{K}$ = 0.5 is about 3.5 times of that for $\tilde{K}$ = 0.1, and is more than 7 times of that for $\tilde{K}$ = 0.05.

It is possible to optimize the manifold performance by selecting the permeability to limit suction and release most of the incoming fluid in a narrow vertical region of the height of neutral buoyancy. However, quantification of the optimum value for $\tilde{K}$ requires knowledge of the mixing process inside the manifold due to suction and the mixing process in the tank due to the release of the fluid. The complex transient fluid structure within the tank itself is not captured by the 1-D model. Additional study is required to fully characterize the effect of the manifold on the mixing process in a solar storage tank.

Nevertheless, from the present results we expect that suction is the most important parameter to control because it creates direct mixing between the incoming fluid and the tank fluid. We anticipate the optimum $\tilde{K}$ to be from 0.005 to 0.05.

2.4 Conclusion

Promoting and maintaining thermal stratification within the storage tank of solar thermal systems improves their overall thermal performance and economics. In the present work, we model the flexible porous manifold, which was first proposed by Loehrke and co-workers[4,5] and investigated subsequently by several groups [6–8] under the supposition that the flexibility of the manifold provides the benefit of adapting to the operational conditions. In prior work, it was postulated that a flexible fabric manifold automatically forms a vertical cross-sectional area distribution that enforces pressure balance between inside the manifold and in the tank, thereby eliminating entrainment of the tank fluid. We explore this hypothesis via the first model of the flexible tube to include the fluid-structure interaction. The 1-D model allows us to capture the interaction between a buoyant plume and the deformation of the manifold. The conservation equations of mass, momentum, and energy are derived following the one-dimensional theory of flows in channels of variable cross-sectional area. The relationship between the cross-sectional area and the differential pressure across the manifold surface is described by the "tube law". The model was applied for a range of porous materials and for operating conditions normally encountered in solar hot water systems. The results are presented in terms of the relevant dimensionless parameters, namely, dimensionless stress ($20 \le \tilde{S}_b \le 2000$), dimensionless axial pre-stress (

$0.05 \le \tilde{F} \le 5$), dimensionless permeability ($0.005 \le \tilde{K} \le 0.5$), and Richardson number ($100 \le Ri_L \le 400$).

The results show that contrary to the widely held belief that the change of cross-sectional area induced by the fluid-structure interaction is beneficial, the fluid-structure interaction does not have significant impact on the effectiveness of the manifold. In comparison to a rigid porous manifold, the flexile manifold may perform worse because the collapse of the manifold encourages suction from the tank into the manifold. Neither the flexibility nor the change of cross-sectional area has significant impact on overall performance. On the other hand, the dimensionless permeability $\tilde{K}$ of the manifold, which depends on the dimensional permeability *K* under a fixed inlet flow rate, has a profound impact on the manifold performance. If $\tilde{K}$ is too low, the manifold behaves as a diffuser, releasing the manifold fluid over the entire height of the tank; if $\tilde{K}$ is too high, significant suction occurs. With this knowledge, it is possible to select the permeability of the fabric to limit entrainment and release the incoming fluid to the desired height in the tank at the position of neutral buoyancy. A more complete computational study that includes the mixing processes in the tank is an important step toward optimization.

Chapter 3

Selection of Permeability for Optimum Performance of a Porous-Tube Thermal Stratification Manifold

Abstract

In this study, we investigate the ability of porous tubes to maintain thermal stratification in a water storage tank in comparison to a top-mounted inlet pipe. Transient distributions of temperature and velocity are presented for operating conditions and a tank geometry representative of solar domestic hot water systems using a transient two-dimensional computational fluid dynamic model. The stratification in the tank is quantified by a dimensionless exergy efficiency. The results demonstrate the importance of selection of the permeability of the manifold on performance. A porous manifold improves thermal stratification for intermediate charging, regardless of the choice of permeability. Over a large range of Richardson number, the manifold is most effective for a dimensionless permeability, defined by the ratio of the pressure drop across the porous wall to the axial pressure gradient, equal to 0.02. Such a manifold will deliver the fluid to the tank in a narrow band at the vertical position of neutral buoyancy and will prevent suction of warmer fluid stored at the top of the tank into the manifold. For top charging the porous manifold is comparable in performance to a well-designed inlet pipe.

Note: The content of this chapter was published as in Ref. [21]

Recommendations of selection of porous material based on dimensionless permeability are provided.

Keywords: sensible storage, exergy, water, heating, solar, stratification, model, manifold

3.1. Introduction

Thermal stratification of solar water storage tanks improves solar collector efficiency and the quality of hot water delivered to the load [1,12]. An ideally stratified tank would provide 15-37% higher solar fraction than that provided by a fully mixed tank [3,14]. Establishing and maintaining a high degree of thermal stratification requires control of the fluid motion within the tank. The need for flow control is most critical during charging when the inlet fluid is cooler than the fluid stored at the top of the tank. With a conventional top-mounted inlet pipe the fluid entering the tank forms a descending thermal plume which entrains tank fluid and creates large scale mixing (Fig.3.1a) [42,43]. The entrainment flow rate has been estimated to be seven times the inlet flow rate [44]. The descending plume may carry sufficient momentum to destabilize the density interface between layers of different temperature.

Numerous efforts have been devoted to develop stratification manifolds to prevent destabilization and mixing. Concepts include flexible fabric manifolds [5–8], rigid pipes with non-return outlet valves [8,18], and rigid porous manifolds with [4,5,16,25,45] and without [9,46] vertical hydraulic resistance elements. A manifold should deliver the inlet fluid to the tank at the level of neutral buoyancy and prevent mixing of tank and inlet fluid within the manifold itself. Mixing in the manifold occurs if fluid from the tank is

sucked into the openings in the manifold that are intended for outward flow into the tank (Fig. 3.1b). In addition, an effective manifold should maintain stratification even as the operating conditions change (i.e. inlet temperature, tank temperature distribution, and inlet mass flow rate). This adaptability to transient conditions is one of the most difficult design challenges. Furthermore, to construct the manifold low thermal conductivity material such as plastics is preferred, so that the degradation of stratification due to heat conduction through the manifold wall is minimized.

In the present study, we consider the performance and design of porous tube without internal resistance elements because it is arguably the most conceptually simple design. Such a tube could be made of a number of porous materials, including rolled screen, fabric, open cell plastic foam, or sintered porous plastic. Fluid from the collector enters the porous tube and then flows into the tank through the porous wall. The lower end of the tube is closed to prevent fluid from passing directly through the tube. The important design challenge is to select the permeability of the porous material so the inlet fluid enters the tank in a narrow region at the vertical height where the fluid is neutrally buoyant with respect to the storage fluid and suction into the manifold is minimized.

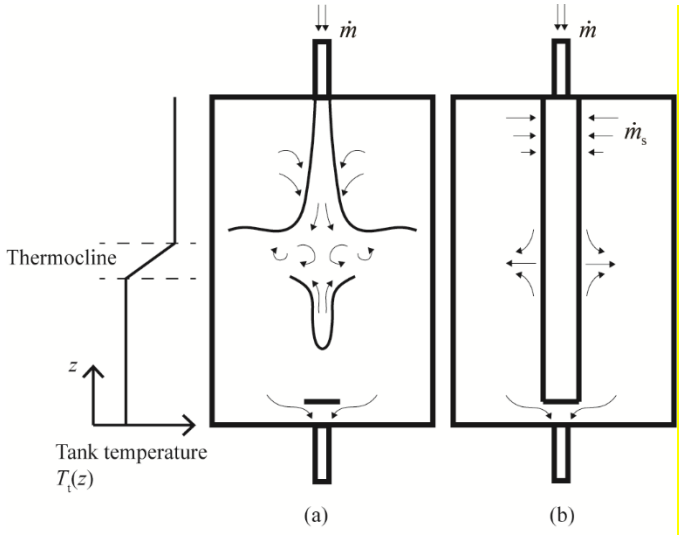

Figure 3.1 Sketch of the flow field during intermediate charging: (a) top-mounted inlet pipe with mixing created by entrainment and the vertical momentum of the descending jet; (b) porous-tube stratification manifold with flow out of the manifold into the thermocline with some suction at the top of the manifold where the tank pressure exceeds the pressure in the manifold.

Prior study of the porous-tube manifold provides valuable insights to its behavior but is limited in scope to numerical analysis [9] of charging a cooler tank (referred to as top charging because the desire is to place the incoming warmer fluid at the top of the tank), and experimental observations [10] of a specific manifold during top and intermediate charging (where the incoming fluid is at a temperature cooler than that stored at the top of a thermally stratified tank but warmer than that stored at the bottom of the tank). One difference between the current and the prior work is the arrangement of the manifold in the tank. In the prior work, the outlet of the manifold was connected directly to an outlet port at the bottom of the tank, allowing the inlet fluid to pass through the tank. In the present work, the manifold is closed at the bottom. This arrangement represents the anticipated situation in a solar storage tank. Numerical study [9] suggests that the porous tube is not beneficial for top charging. For intermediate charging, a flow visualization

study implies greater promise [10]. However, it is likely that the permeability in the prior work was not well matched with the operating conditions. With a permeability of 1×10^{-9} m^2 and thickness of 0.0065 m, the inlet fluid was released too high in the tank, likely due to suction into the top of the tube. The authors of the prior work state that the manifold worked by deforming in response to the pressure difference across the tube wall. However, no evidence of deformation was provided.

In the present work, we provide guidelines for the design of porous-tube manifold for two charging scenarios: 1) intermediate temperature fluid entering a stratified tank with warmer fluid at the top (intermediate charging), and 2) warm fluid entering a uniform temperature cooler storage tank (top charging). Together these scenarios capture the most important physics of the flow encountered during charging of solar water storage tanks. We show through numerical analyses how the permeability of the tube impacts its behavior under a wide variety of conditions and discuss the suitability of this type of manifold for solar water storage tanks. The stratification in the tank is quantified using dimensionless exergy efficiency. The effectiveness of the manifold is compared with the top-mounted inlet pipe.

3.2. Methodology

The two key dimensionless parameters important to the underlying physics of the fluid dynamics of the porous tube are the Richardson number and the dimensionless permeability. The Richardson number, Ri_L,

$$Ri_L = \frac{gL\beta_{in}\left(T_H - T_C\right)}{\bar{u}_{in}^2} \tag{3.1}$$

is the ratio between buoyancy and the kinetic energy of the inlet flow. It can be rewritten in terms of the inlet mass flow rate using $\bar{u}_{\text{in}} = \dot{m}_{\text{in}} / \pi R_{\text{i}}^2 \rho_{\text{in}}$. Because thermal stratification is achieved when the incoming fluid enters the tank at the level of neutral buoyancy, it is important to select the tube diameter for a fixed flow rate so fluid motion is dominated by buoyancy. We recommend Ri_{L} is on the order of 100 or larger.

The dimensionless permeability $\tilde{K}$,

$$\tilde{K} = \frac{2KL_{\text{mf}}\dot{m}_{\text{in}}}{\pi\mu\delta R_{\text{i}}^3} \tag{3.2}$$

is the ratio between the pressure drop across the porous wall and the pressure change in the axial direction inside the manifold. Its magnitude defines the behavior of the flow across the porous wall. When $\tilde{K} << 1$, the manifold behaves like a diffuser according to the theory of diffuser design [37] and fluid enters the tank over the entire height of the manifold. Because this behavior does not deliver the fluid to the height of neutral buoyancy it is not favorable to achieve stratification. As $\tilde{K}$ is increased, by for example increasing the permeability of the manifold, the inlet fluid will be released from the manifold in a narrower band at the level of neutral buoyancy, but with the detrimental effect of increased suction into the manifold. Thus there is a balance in the choice of $\tilde{K}$ between delivering the fluid to the correct height and preventing suction.

The Reynolds and Peclet numbers are additional relevant dimensionless parameters, but for the present application the behavior of the manifold is insensitive to variations in these parameters over the ranges expected in practice.

We first employ a two-dimensional computational fluid dynamic model to compare the flow dynamics and temperature distributions in water storage tank with and without a

porous-tube manifold. The two-dimensional model adequately predicts the velocity distribution at the outer surface of the manifold and the large-scale mixing in the tank. This approach is applied to study the impact of the dimensionless permeability on performance for a base case representative of domestic solar hot water systems. For the base case $Ri_L \sim 400$ and $\tilde{K}$ is varied over the range from 0.002 to 2. We then present a parametric study to illustrate the effect of manifold permeability for a wider range of Richardson number using a one-dimensional analysis.

3.2.1 Geometry and Operating Conditions

The geometry of the manifold and the tank are typical of a domestic hot water system. The cylindrical tank is sized for a system with two solar collectors [40]. The tank is 0.3 m^3, with a height to radius ratio of 3.5 (0.3 m radius, 1.05 m height) as recommended to help maintain thermal stratification [47]. The conventional tank (Figure 3.1a) uses a top-mounted inlet pipe without a manifold. Because it is well known that mixing occurs when the inlet fluid exits a small pipe and discharges into the tank, we simulate the addition of an inlet diffuser by assuming that the fluid enters the tank with a fully-developed velocity profile from a 0.077 m-diameter pipe. Fluid is returned from the tank to the collector loop from an identical pipe at the bottom of the tank; a baffle plate restricts the outlet flow to the lower section of the tank, as would be expected in practice if a top-mounted drop tube is installed. To achieve numerical stability and accuracy in the region near the inlet and outlet of the tank, the length of the pipe leading to the tank is seven times the radius, i.e., 0.27 m.

The manifold is a 0.077 m I.D., 0.089 m O.D porous tube connected directly to the inlet pipe (Figure 3.1b). The diameter is similar to that of a wide variety of manifolds

developed in prior work. Here, we arbitrarily assume the wall is 0.006 m thick and 60% porous. The manifold is assumed to be a material with low thermal conductivity. The lower end of the tube is closed and impermeable to fluid. The permeability of the tube is varied three orders of magnitude ($1\times10^{-11} \leq K \leq 1\times10^{-8}$ m^2, corresponding to $0.002 \leq \tilde{K} \leq 2$). This range is representative of candidate porous materials such as plastic foam, fabrics, and free-sintered plastic tubes [46,48,49]. Thermophysical properties, including thermal conductivity, of the inlet pipe and the manifold are set equal to those of CPVC [50] and are listed in Table 3.1.

The transient charging process is simulated for an inlet mass flow rate of 0.07 kg/s (based on 0.015 kg/s/m^2 for a collector area of 4.7 m^2). Initially, the fluid in the tank is assumed to be quiescent. The initial temperature distribution depends on the mode of charging. For the intermediate charging mode, the tank is thermally stratified in two equal volume layers with T_H = 50 °C and T_C = 20 °C. The initial thermocline between these layers is assumed to be 0.05 m thick at the mid-height of the tank ($z = (L_{out} + L_t)/2$). The inlet fluid temperature is set at an intermediate temperature, T_{in} = 35 °C. For the top charging mode, the tank is initially isothermal at 20 °C and $T_{in} = T_H$ = 50 °C. For each case considered, we simulate 900 s of charging, which is the time required to displace about 21% of the storage volume. The Reynolds number (Re_D) is 1648 for T_{in} = 35 °C and 1170 for T_{in} = 50 °C, respectively. The Richardson number (Ri_L) is 448 for intermediate charging and 422 for top charging, both are sufficiently high to potentially achieve high degree of stratification in the tank

Table 3.1. Thermophysical properties

Material properties of CPVC	Variables	Values (units)
Density of the solid	ρ_s	1530 (kg/m^3)
Specific heat of the solid	$c_{p,s}$	780 (J/kg/K)
Thermal conductivity of the solid	k_s	0.138 (W/m/K)
Material properties of water	**Variables**	**Values (units)**
Density of the fluid	ρ_f	$\rho_f = 838.466 + 1.400T - 0.003T^2 + 3.718\times10^{-7}T^3$ (kg/m^3)
Dynamic viscosity	μ	$\mu = 1.380 - 0.021T + 1.360\times10^{-4}T^2 - 4.645\times10^{-6}T^3 + 8.904\times10^{-6}T^4 - 9.080\times10^{-13}T^5 + 3.846\times10^{-16}T^6$ (Pa.s)
Thermal conductivity of the fluid	k_f	0.63 (W/m/K)
Specific heat of the fluid	$c_{p,f}$	4068.5 (J/kg/K)
Properties of the porous manifold	**Variables**	**Values (units)**
Porosity for the manifold	ε	0.6
Permeability for the manifold	K	10^{-11}–10^{-8}(m^2)

Because the transient 2-D simulation is computationally intensive, we use a 1-D model of the manifold to recommend values of dimensionless permeability for Richardson numbers from 100 to 1000.

3.2.2 Modeling

3.2.2.1 CFD model

The geometry is axisymmetric and therefore the CFD model is two-dimensional in the radial and axial directions. The computational domain is shown in Figure 3.2. The cross-hatched region represents the porous wall (not to scale). The figure is labeled to indicate where boundary conditions are applied. The computational domain for the conventional tank is identical with the exception of the absence of a manifold. The model is described by two regions: a porous region, which represents the permeable wall of the

manifold (when present), and a pure fluid region, which represents the water flowing through the manifold and in the storage tank. In the porous region, the mass conservation equation, the Darcy-Brinkman equation, and the energy conservation equation under the assumption of local thermal equilibrium (LTE) are applied:

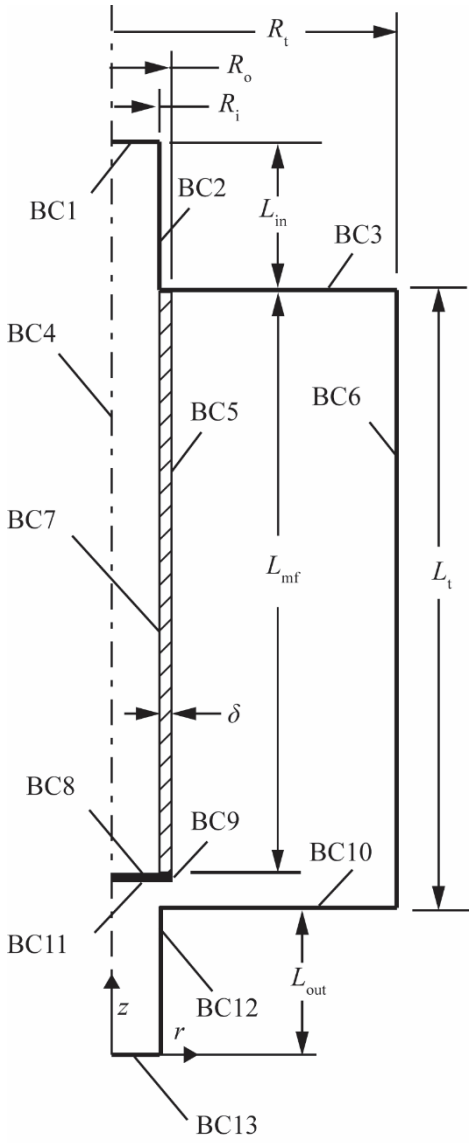

Figure 3.2 Computational domain with boundary conditions labeled for the convenience of the reader (not to scale)

$$\nabla \cdot \mathbf{u} = 0 \tag{3.3}$$

$$\frac{\rho_{\mathrm{f}}}{\varepsilon}\left(\frac{\partial \mathbf{u}}{\partial t}+\mathbf{u}\cdot\frac{\nabla \mathbf{u}}{\varepsilon}\right)=-\nabla p-\frac{\mu}{K}\mathbf{u}+\frac{\mu}{\varepsilon}\nabla^2\mathbf{u}+\rho_{\mathrm{f}}\mathbf{g} \tag{3.4}$$

$$\left(\rho c_p\right)_{\mathrm{eff}}\frac{\partial T}{\partial t}+\left(\rho c_{\mathrm{p}}\right)_{\mathrm{f}}\mathbf{u}\cdot\nabla T=k_{\mathrm{eff}}\nabla^2 T \tag{3.5}$$

The LTE approximation for conservation of energy is accurate for relatively slow transient processes [51] such as charging the storage tank at the mass flow rate assumed here. The effective properties of the porous medium are expressed as $\left(\rho c_{\mathrm{p}}\right)_{\mathrm{eff}}=\varepsilon\left(\rho c_{\mathrm{p}}\right)_{\mathrm{f}}+\left(1-\varepsilon\right)\left(\rho c_{\mathrm{p}}\right)_{\mathrm{s}}$ and $k_{\mathrm{eff}}=\varepsilon k_{\mathrm{f}}+\left(1-\varepsilon\right)k_{\mathrm{s}}$ [51].

In the pure fluid domain, the Navier-Stokes equations for incompressible flow and conservation of energy are applied:

$$\nabla\cdot\mathbf{u}=0 \tag{3.6}$$

$$\rho_{\mathrm{f}}\left(\frac{\partial \mathbf{u}}{\partial t}+\mathbf{u}\cdot\nabla\mathbf{u}\right)=-\nabla p+\mu\nabla^2\mathbf{u}+\rho_{\mathrm{f}}\mathbf{g} \tag{3.7}$$

$$\rho_{\mathrm{f}}c_{\mathrm{p,f}}\left(\frac{\partial T}{\partial t}+\mathbf{u}\cdot\nabla T\right)=k_{\mathrm{f}}\nabla^2 T \tag{3.8}$$

A fully developed Poiseuille velocity profile is prescribed at the inlet *(* $z=L_{\mathrm{in}}+L_{\mathrm{out}}+L_{\mathrm{t}}$ *)* indicated as BC1 in Figure 3.2.

$$u_{\mathrm{z}}=-\frac{2\dot{m}_{\mathrm{in}}}{\pi\rho_{\mathrm{in}}R_{\mathrm{in}}^2}\left[1-\left(\frac{r}{R_{\mathrm{in}}}\right)^2\right] \tag{3.9}$$

$$u_{\mathrm{r}}=0 \tag{3.10}$$

$$T=T_{\mathrm{in}} \tag{3.11}$$

At the outlet ($z = 0$), indicated as BC13 in Figure 3.2, the viscous stress and gauge pressure are set to zero,

$$p = 0, \quad \mu\left[\nabla\mathbf{u} + (\nabla\mathbf{u})^T\right]\cdot\mathbf{n} = \mathbf{0} \tag{3.12}$$

and

$$\frac{\partial T}{\partial z} = 0 \tag{3.13}$$

The non-slip velocity boundary condition and adiabatic thermal boundary condition are applied at all solid surfaces (BC2, 3, 6, and 8-12 in Figure 3.2).

$$\mathbf{u} = \mathbf{0} \tag{3.14}$$

$$\frac{\partial T}{\partial \mathbf{n}} = \mathbf{0} \tag{3.15}$$

For the interfaces between the pure fluid and the porous regions (BC5 and 7), continuity of velocity, pressure and temperature is enforced.

$$\mathbf{u}_{\mathrm{f}} = \mathbf{u}_{\mathrm{p}} \tag{3.16}$$

$$p_{\mathrm{f}} = p_{\mathrm{p}} \tag{3.17}$$

$$T_{\mathrm{f}} = T_{\mathrm{p}} \tag{3.18}$$

A symmetric boundary condition is applied at $r = 0$ (BC4):

$$u_{\mathrm{r}} = 0 \tag{3.19}$$

$$-p + \mu\nabla^2 u_{\mathrm{z}} = 0 \tag{3.20}$$

$$\frac{\partial T}{\partial r} = 0 \tag{3.21}$$

The fluid density ρ_f and viscosity μ , are modeled with third order polynomial functions of temperature based on regression of data for water. Specific heat and thermal conductivity of the fluid are fixed. The values and regression expressions for fluid thermophysical properties are listed in Table 3.1.

The 2-D model is implemented in the finite element software package COMSOL [52]. It was validated against experimental data extracted from the study on natural convection in partially filled porous cavities [53]. For the manifold model, a mapped mesh scheme is used. A mesh independent study was conducted on a coarse mesh (10230 elements), a normal mesh (17116 elements), and a fine mesh (19546 elements) mesh. The root mean square errors of temperature at t = 900 s and $r = R_t/2$ between the coarse mesh and the normal mesh, and between the normal mesh and the fine mesh are less than 4%. Therefore, the normal mesh is used for the reported data. An adaptive backward differentiation formula time stepping method is applied. The maximum time step is 0.05s with the relative tolerance set to 10^{-6}. The runtime using 8 cores and 16 GB RAM on a HP Linux cluster is 14-34 hours.

3.2.2.2 One-Dimensional model

The 1-D steady state model is similar to the model of a rigid porous manifold with vertically distributed orifice plates developed by Gari and Loehrke [5]. The major differences are the elimination of the vertical hydraulic resistance elements and the use of Darcy's Law to capture the flow across the porous wall rather than treating the wall as a series of orifices. The axial distributions of mass flow rate ($\dot{m}$), pressure difference

across the porous wall ($\Delta p = p - p_t$), and temperature in the manifold are determined by the governing conservation equations of mass, momentum, and energy:

$$\frac{d\dot{m}}{dz} = -2\pi R_o \rho_{in} u_r \tag{3.22}$$

where the radial flow rate u_r is described by the Darcy's law

$$u_r = \frac{K\Delta p}{\mu\delta}, \tag{3.23}$$

$$\frac{d\Delta p}{dz} = -\left(\rho - \rho_t\right) g - \frac{\dot{m}}{\rho_{in} A^2}\frac{d\dot{m}}{dz} \tag{3.24}$$

where $A = \pi R_i^2$ is the cross-sectional area of the manifold, and

$$\frac{dT}{dz} = \begin{cases} \dfrac{Ak_f}{\dot{m}c_p}\dfrac{d^2T}{dz^2}, & \Delta p \geq 0 \\ -\dfrac{\left(T - T_t\right)}{\dot{m}}\dfrac{d\dot{m}}{dz} + \dfrac{Ak_f}{\dot{m}c_p}\dfrac{d^2T}{dz^2}, & \Delta p < 0 \end{cases} \tag{3.25}$$

The boundary conditions at the inlet and bottom of the manifold are identical to those used for the 2-D CFD model. The inlet mass flow rate is set to vary the Richardson number. For each Richardson number, we model hundreds of values of permeability in order to recommend values for intermediate and top charging.

The governing differential equations are formulated in dimensionless form and converted to a set of first order differential equations (ODEs) which are solved using the MATLAB ODE solver—"byp4c". The maximum mesh size is set to 2000 and the absolute and relative tolerances are 1×10^{-6} and 1×10^{-3}, respectively. The 1-D approach is validated by comparison to the 2-D model for the base case.

3.2.3 Figures of Merit

For the CFD results we use two figures of merit to evaluate the performance of the porous manifold. Mixing in the tank generates entropy and reduces the exergy content of the storage tank [54–56]. The specific exergy carried by the fluid neglecting the kinetic and potential exergy is

$$\begin{aligned} e_{\mathrm{x}} &= \left(h - h_{\mathrm{o}}\right) - T_{\mathrm{o}}\left(s - s_{\mathrm{o}}\right) \\ &= c_{\mathrm{p}}\left[\left(T - T_{\mathrm{o}}\right) - T_{\mathrm{o}} \ln\left(\frac{T}{T_{\mathrm{o}}}\right)\right] \end{aligned} \tag{3.26}$$

where T_{o} is the dead state temperature set to the assumed supply temperature of 20 °C. The total exergy content in the tank is

$$E_{\mathrm{x}} = \iiint_{CV} e_{\mathrm{x}}\, dv \tag{3.27}$$

The dimensionless exergy efficiency E_{x}^{*} is expressed as

$$E_{\mathrm{x}}^{*} = \frac{E_{\mathrm{x,st}} - E_{\mathrm{x}}}{E_{\mathrm{x,st}} - E_{\mathrm{x,mix}}} \tag{3.28}$$

where $E_{\mathrm{x,st}}$ is exergy for a ideally stratified tank and $E_{\mathrm{x,\,mix}}$ is that for a fully mixed tank. The fully mixed tank temperature is based an overall energy balance of the tank.

$$T_{\mathrm{mix}} = \frac{\dot{m} T_{\mathrm{in}} t + \pi R_{\mathrm{t}}^{2} \int_{L_{\mathrm{out}}}^{L_{\mathrm{t}}+L_{\mathrm{out}}} \rho_{\mathrm{t}}\left(z\right) T_{\mathrm{t}}\left(z\right) dz}{\left(\pi \rho_{\mathrm{mix}} R_{\mathrm{t}}^{2} L_{\mathrm{t}} + \dot{m}\right) t} \tag{3.29}$$

Similarly, $E_{\mathrm{x,st}}$ is calculated using the ideal tank temperature distribution predicted by a plug flow model [57]. In a plug flow model, the tank is partitioned into segments of uniform temperatures. For ideal charging, the plug flow model always inserts incoming fluid at the level of neutral buoyancy, and shifts the position of all existing segments

between inlet and outlet. $E_x^* = 0$ is the maximum possible stratification efficiency, and $E_x^* = 1$ indicates the tank is completely mixed.

For intermediate charging, the ratio of the suction rate $\dot{m}_s / \dot{m}_{in}$ provides a measure of the ability of the manifold to prevent suction. Suction leads to mixing of the inlet fluid and the warmer fluid stored at the top of the tank and increases the vertical momentum of the descending plume, which in turn enhances mixing within and below the thermocline. The suction rate for porous manifold is calculated by integrating the mass flux into the manifold over its height,

$$\dot{m}_s = 2\pi R_o \int_{L_t + L_{out} - L_{mf}}^{L_t + L_{out}} -\rho \min\left(u_r|_{r=R_o}, 0\right) dz \tag{3.30}$$

The minimum operator, min( ), ensures that only flow sucked into the manifold (negative u_r) is included in the integrand. For an ideal manifold, $\dot{m}_s / \dot{m}_{in} = 0$. The ratio increases with increasing suction into the manifold.

For 1-D model, we use the predicted flow distribution across the wall of the porous manifold to guide our recommendation for dimensionless permeability. As discussed in section 3.3.2, the interpretation of the velocity distribution is guided by the 2-D CFD model which captures the interaction of the manifold with the fluid in the tank.

3.3. Results

The performance of the porous manifold is compared to that of the conventional inlet pipe for both intermediate charging and top charging. It is important to consider both modes of operation to fully understand the ability of the porous manifold to control mixing and to draw general conclusions regarding manifold design.

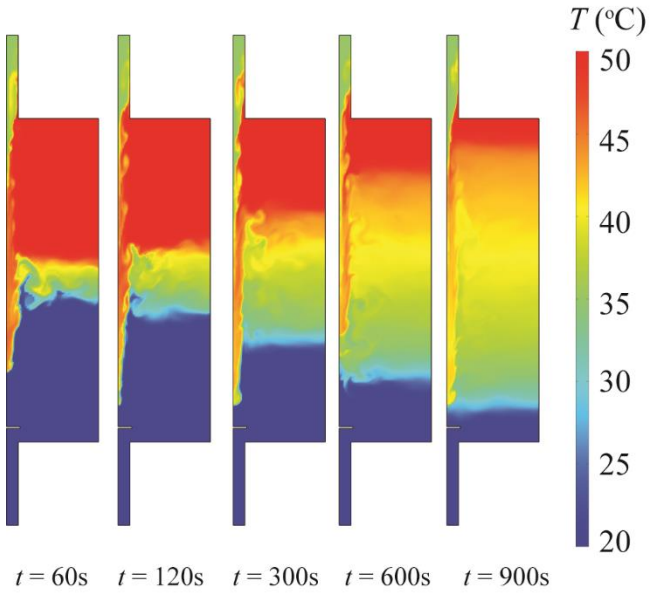

Figure 3.3 Transient temperature distributions for the inlet pipe under intermediate charging

3.3.1 Base Case

3.3.1.1 Intermediate charging

Transient temperature and velocity distributions for the inlet pipe (i.e., no manifold) are shown in Figures 3.3 and 3.4, respectively. When charging is initiated, the fluid entering the top of tank forms a negatively buoyant plume (downward in the direction of gravity) that descends through the warmer upper layer of fluid. As charging progresses, mixing at the shear layer of the descending plume increases the thickness of the thermocline and reduces the level of thermal stratification. As shown in Figure 3.3, the thickness of the thermocline grows most rapidly when charging is initiated. At t = 300 s, the thermocline thickness is about one-third of the height of the tank. At t = 900 s, when 21% of tank fluid has been replaced, the thermocline thickness is 80% of the height of the tank. To illustrate the nature of the flow field, the instantaneous velocity distribution at t

= 120 s is shown in Figure 3.4. The shear layer at the boundary of the descending plume is unstable leading to enhanced mixing. The warmer tank fluid at the top of the tank is entrained into the cooler plume as it descends, contributing to destruction of stratification in the top half of the tank. The plume reaches and penetrates the thermocline with a velocity of 0.2 m/s. Consequently, the thermocline is destabilized and mixing in and near the thermocline is enhanced.

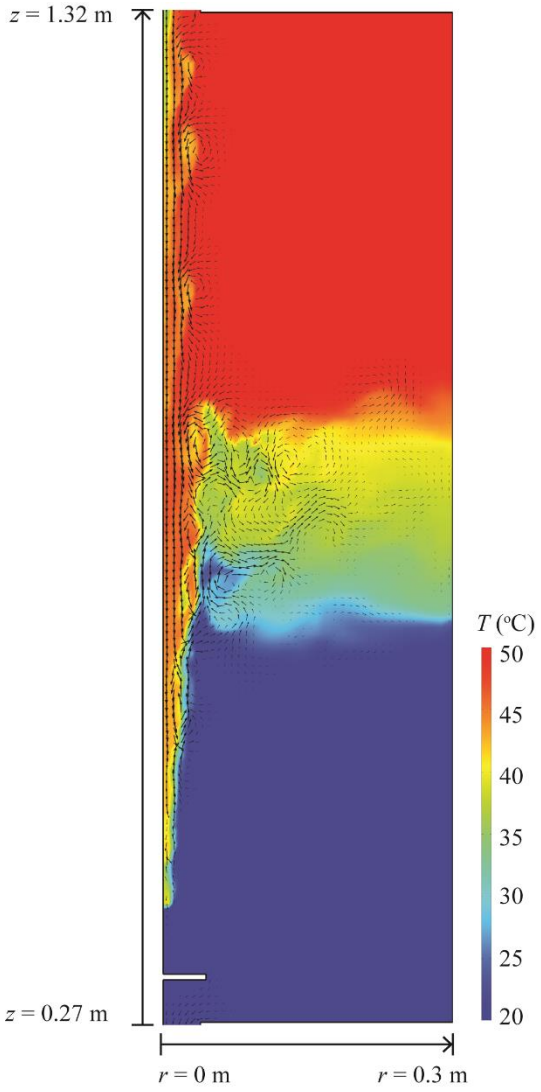

Figure 3.4. Flow field at t = 120 s for intermediate charging with a top-mounted inlet pipe (no manifold). Velocity vectors are shown as an overlay and the arrows are proportional to the logarithmic speed.

Performance of the porous manifold under the same charging scheme is shown for $0.002 \le \tilde{K} \le 2$ in Figures 3.5 through 3.7. The transient temperature distributions in Figure 3.5 demonstrate that the porous manifold slows the growth of the thermocline and mitigates the destruction of thermal stratification compared to the top-mounted inlet pipe. As illustrated in Figure 3.6, for all values of dimensionless permeability considered, a circulating flow is present within the manifold. The value of $\tilde{K}$ affects both the magnitude and position of inflow (suction) and outflow from the manifold. The best performance is achieved with $\tilde{K} = 0.02$. For this case, the manifold provides sufficient resistance across the wall to prevent suction yet it is sufficiently permeable to allow the fluid in the manifold to exit in a narrow region at the vertical position of neutral buoyancy and spread radially outward. With the manifold, the thickness of the thermocline is about half of the tank height at *t* = 900 s. Without a manifold, the thermocline thickness is more than 80% of the tank height at the same time. Higher permeability manifolds pull warm fluid from the top of the tank into the manifold and mixing occurs even before the fluid enters the tank. Less permeable manifolds with lower values of $\tilde{K}$ are undesirable because the height over which the inlet fluid is allowed to pass through the permeable surface into the tank is too large. In the extreme case with $\tilde{K} = 0.002$, the manifold behaves like a diffuser, allowing fluid to enter the tank along the entire height of the manifold.

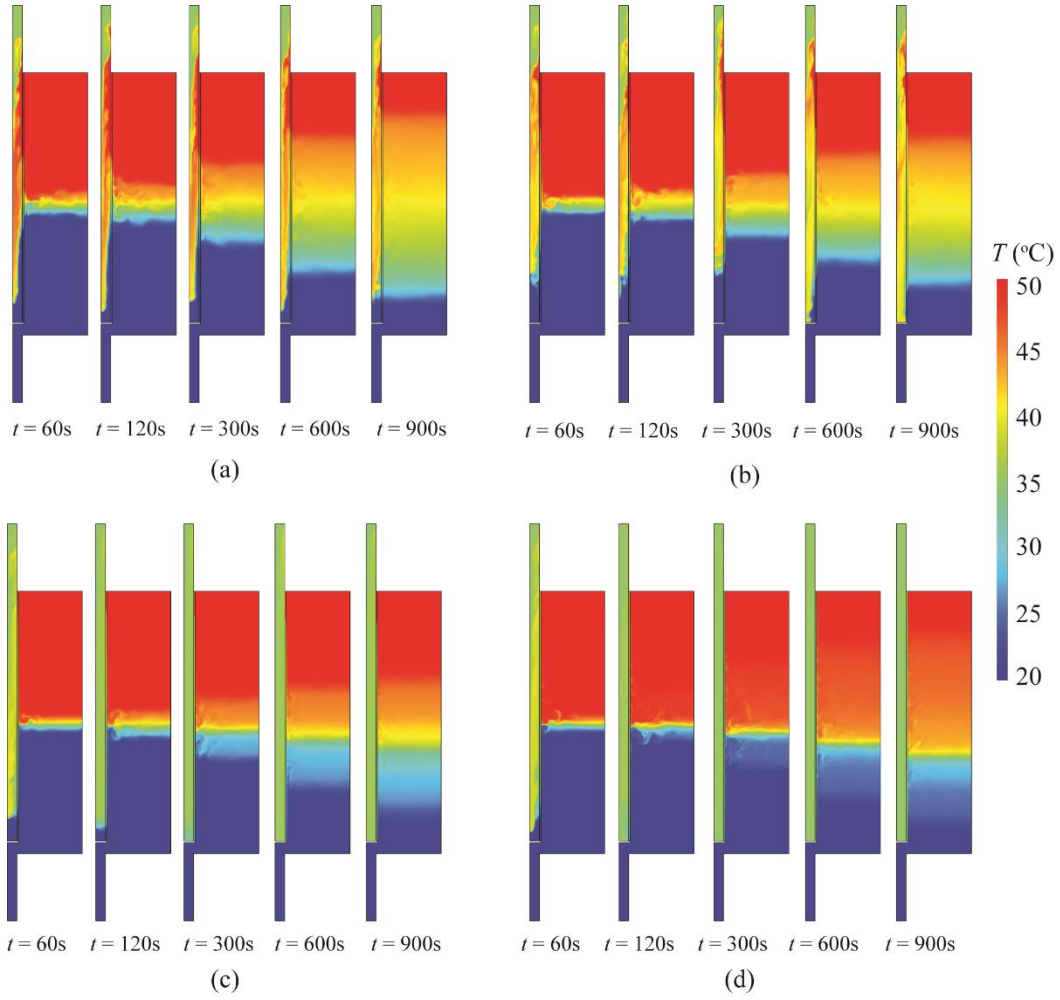

Figure 3.5. Effect of the dimensionless permeability on the transient temperature distribution for porous manifolds under intermediate charging: (a) $\tilde{K} = 2$; (b) $\tilde{K} = 0.2$; (c) $\tilde{K} = 0.02$; (d) $\tilde{K} = 0.002$

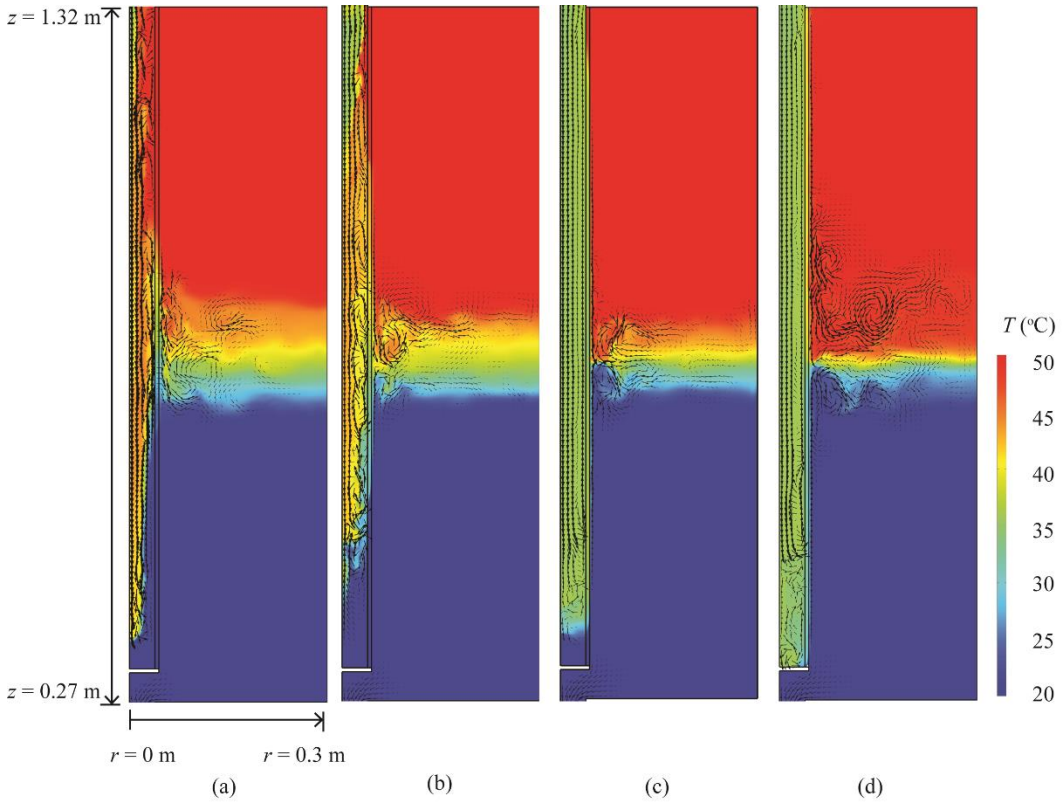

Figure 3.6. Flow field at t = 120 s for intermediate charging: (a) $\tilde{K} = 2$; (b) $\tilde{K} = 0.2$; (c) $\tilde{K} = 0.02$; (d) $\tilde{K} = 0.002$

To illustrate the magnitude of suction as $\tilde{K}$ is varied, the radial component of velocity is plotted in Figure 3.7 as a function of height of the tank at t = 120 s. Positive values of u_r indicate outflow from the manifold and negative values indicate suction. For $\tilde{K} = 0.002$, the manifold behaves like a diffuser allowing fluid to exit uniformly along the entire height of the manifold. For $\tilde{K} = 0.2$ and 2, fluid exits the manifold near the thermocline ($0.6 < z < 1.1$ m), but tank fluid is sucked into the manifold both above ($1.1 < z < 1.3$ m) and below ($0.3 < z < 0.6$ m) the thermocline. The suction destroys thermal stratification. For $\tilde{K} = 2$, $\dot{m}_s / \dot{m}_{in} = 2.7$ and small variations of the differential pressure along the porous surface of the manifold lead to large spatial variations of u_r. For $\tilde{K} = 0.2$

, $\dot{m}_s/\dot{m}_{in} = 0.94$. The best choice is $\tilde{K} = 0.02$; suction is virtually eliminated except in a small region near the very top of tank and $\dot{m}_s/\dot{m}_{in} = 0.04$. The combination of good control of suction and proper release of fluid at the height of neutral buoyancy yields the best performance.

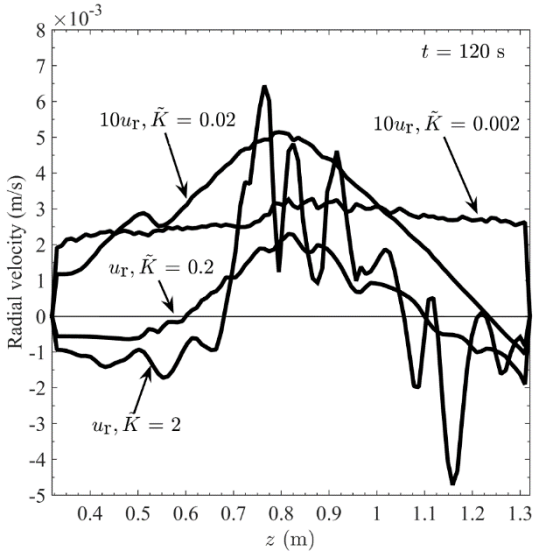

Figure 3.7. Radial velocity u_r versus height for porous-tube manifolds at t = 120 s

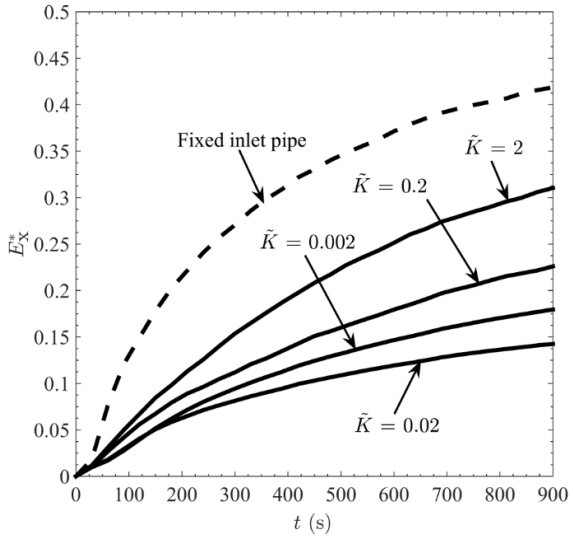

Figure 3.8. Comparison of the dimensionless exergy efficiency for the top-mounted inlet pipe and porous manifolds of varying permeability during intermediate charging

Figure 3.8 compares the performance of the top-mounted inlet pipe and the porous manifold on the basis of the dimensionless exergy efficiency E_x^*. For all manifolds, E_x^* increases as charging proceeds. Stratification is destroyed most quickly at the beginning of charging. All the porous manifolds provide better performance than the top-mounted inlet pipe for intermediate charging. Reducing the dimensionless permeability from 2 to 0.02 enhances the manifold performance as suction into the manifold is eliminated. Further decreasing $\tilde{K}$ to 0.002 decreases the performance because the manifold behaves like a diffuser. At t = 900 s, when 21% of the tank fluid is displaced, E_x^* is 0.14 for $\tilde{K} = 0.02$. For the inlet pipe, E_x^* is 0.41.

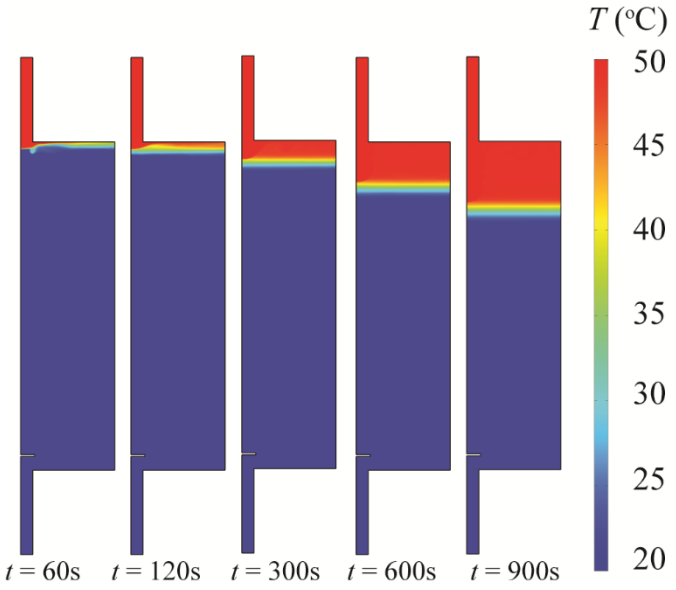

Figure 3.9. Transient temperature distributions for the top-mounted pipe under top charging

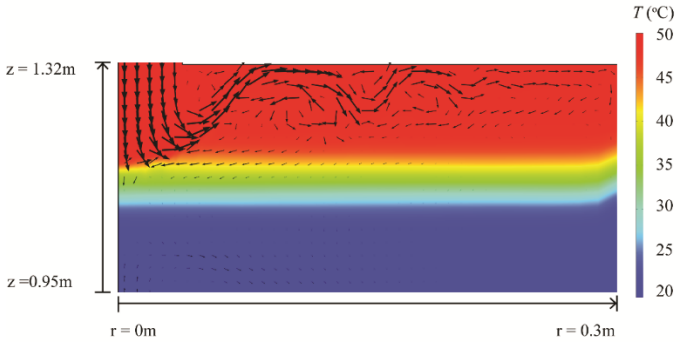

Figure 3.10. Flow field at t = 300 s for top charging with a top-mounted inlet pipe (no manifold). Velocity vectors are shown as an overlay and the arrows are proportional to the logarithmic speed.

3.3.1.2 Top charging

The physics of fluid dynamics during top charging differs significantly from intermediate charging. In this situation, the inlet fluid is positively buoyant (in the upward direction), and the top-mounted inlet pipe is sufficient to maintain a high degree of thermal stratification for a Richardson number of order 400. The transient temperature profiles for the inlet pipe without a manifold are shown in Figure 3.9. As charging proceeds, the tank becomes thermally stratified into two layers separated by a thin, stable thermocline. Figure 3.10 illustrates the fluid motion near the thermocline at t = 300 s. The vertical momentum of the inlet jet is insufficient to penetrate the thin thermocline. The inlet jet rebounds at the top of the thermocline, reaches the top wall of the tank, and then spreads horizontally as desired to promote stratification.

Comparison of the temperature distributions for the inlet pipe (Figure 3.9) and the porous-tube manifold (Figure 3.11) shows that the best performing manifold for intermediate charging, $\tilde{K} = 0.02$, creates more mixing during top charging than the inlet pipe or a porous-tube manifold with higher permeability. The manifold with $\tilde{K} = 2$

releases the inlet fluid near the top of the tank and the temperature distribution is very close to that achieved with no manifold (see Figure 3.12a). With reduced permeability, the momentum of the inlet flow carries the warmer fluid deeper into the manifold as it is released into the cooler tank (Figure 3.12 b-d). The depth of release increases with decreasing permeability. For the manifold selected for intermediate charging, about one-third of the tank is fully mixed to 40 °C at t = 900 s. The trend of decreasing performance with decreasing permeability is reflected in the values of the dimensionless exergy efficiency (Figure 3.13). The exergy efficiency for the fixed inlet pipe is 0.10 at t = 900 s in comparison to 0.48 for $\tilde{K} = 0.02$. The curves in Figure 13 exhibit slightly different trends than those for intermediate charging. In both charging scenarios, mixing is most intense when charging is initiated. With top charging, E_x^* reaches a maximum and then slowly decreases due to the formation of a stable thermocline and accumulation of warmer fluid in the upper region of the tank.

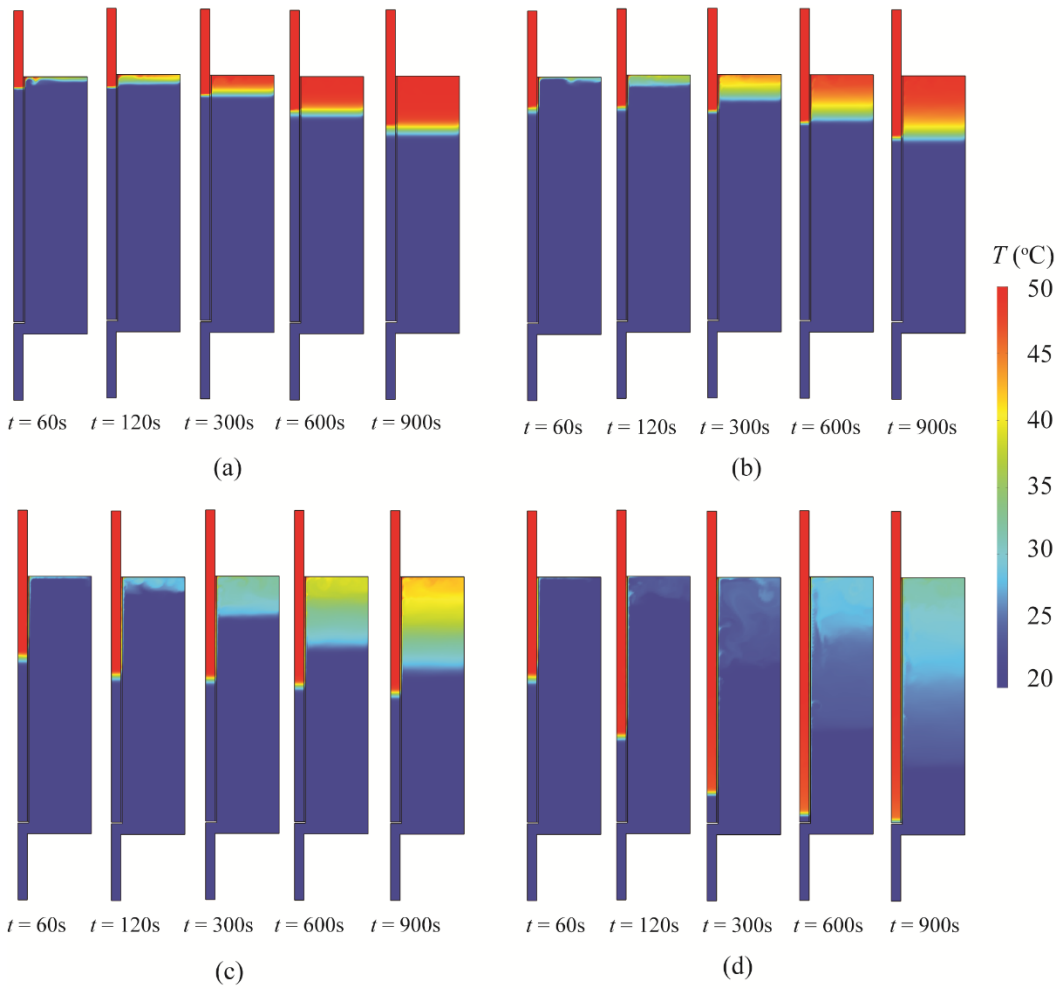

Figure 3.11. Effect of the dimensionless permeability on the transient temperature distribution for porous-tube manifolds under top charging: (a) $\tilde{K} = 2$; (b) $\tilde{K} = 0.2$; (c) $\tilde{K} = 0.02$; (d) $\tilde{K} = 0.002$

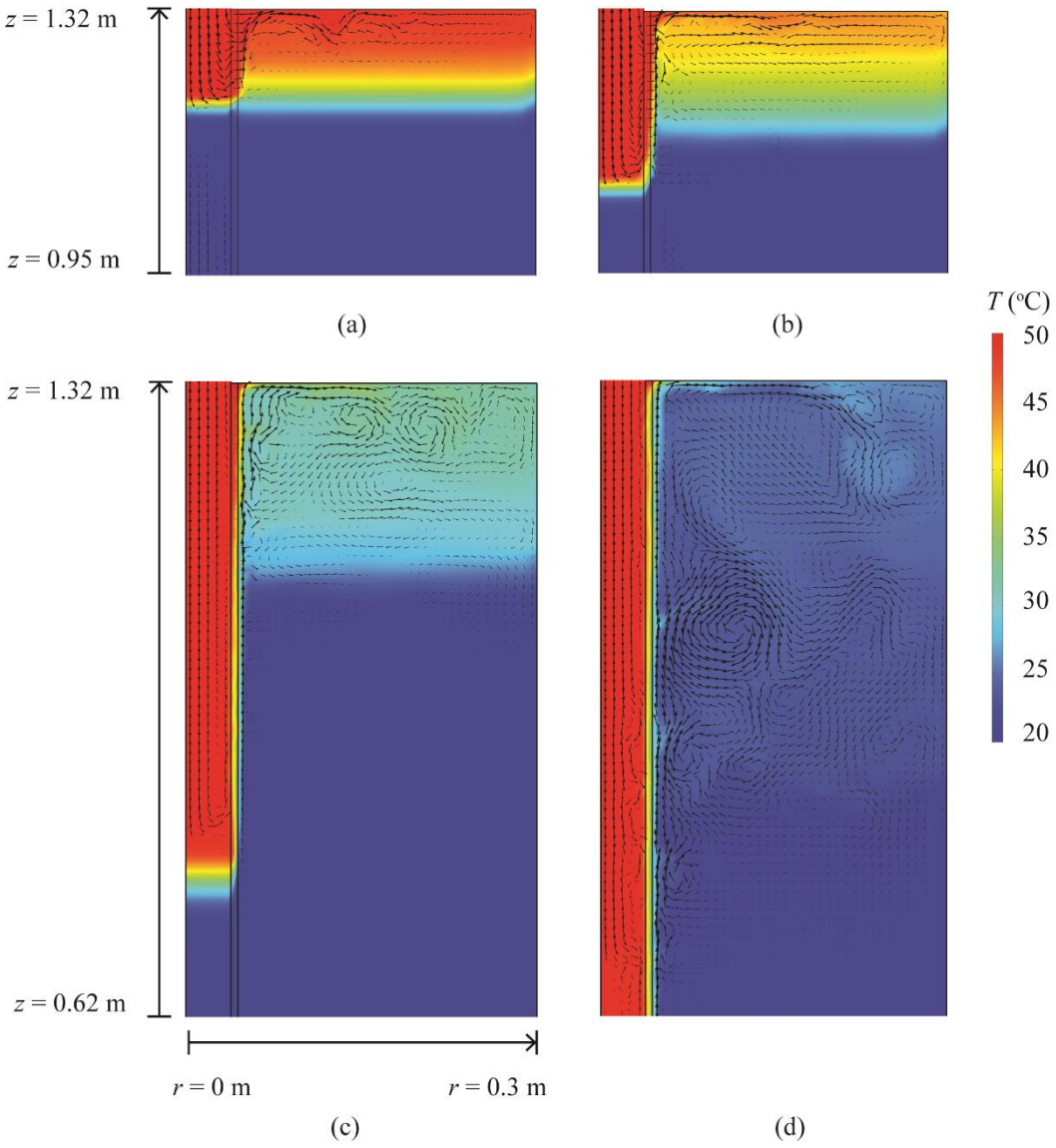

Figure 3.12. Effect of dimensionless permeability on the flow field at t = 300 s for top charging: (a) $\tilde{K} = 2$; (b) $\tilde{K} = 0.2$; (c) $\tilde{K} = 0.02$; (d) $\tilde{K} = 0.002$

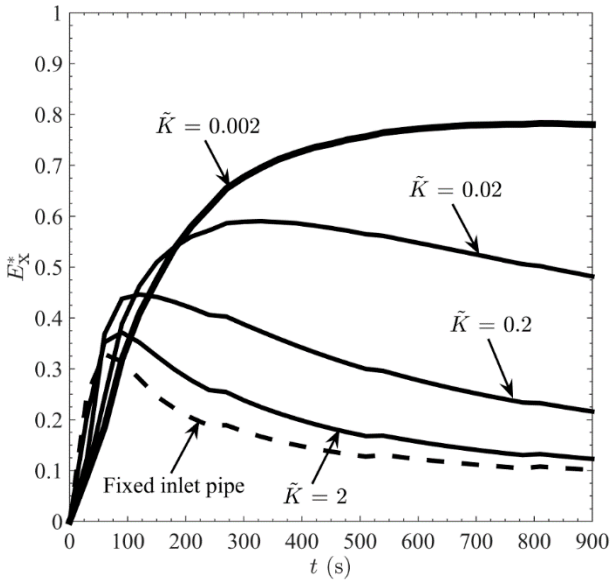

Figure 3.13. Comparison of the dimensionless exergy efficiency for the top-mounted inlet pipe and porous manifolds of varying permeability during top charging

3.3.2 Parametric Study

Figure 3.14 compares the radial velocity distributions predicted for the base case by the 1-D and 2-D models for $\tilde{K} = 0.02$ and $\tilde{K} = 0.2$. There are small differences in the curves because the 1-D model is not able to capture the 2-D flow within the manifold. However, the 1-D model accurately predicts the relative effect of permeability and is thus a valuable tool to recommend permeability for both modes of operation.

For intermediate charging, we recommend the highest value of $\tilde{K}$ for which suction is eliminated. This approach is supported by results of the 2-D CFD model. The dimensionless exergy efficiency E_x^* is highest at the dimensionless permeability $\tilde{K}$ for which suction is eliminated and the manifold fluid is released in a narrow region at the level of neutral buoyancy. If the dimensionless permeability is higher than the

recommended value, more fluid is sucked into the manifold. If the dimensionless permeability is lower than the recommended, the axial distribution of u_r becomes more uniform and the manifold releases a larger portion of the incoming fluid at the wrong height, much like a diffuser.

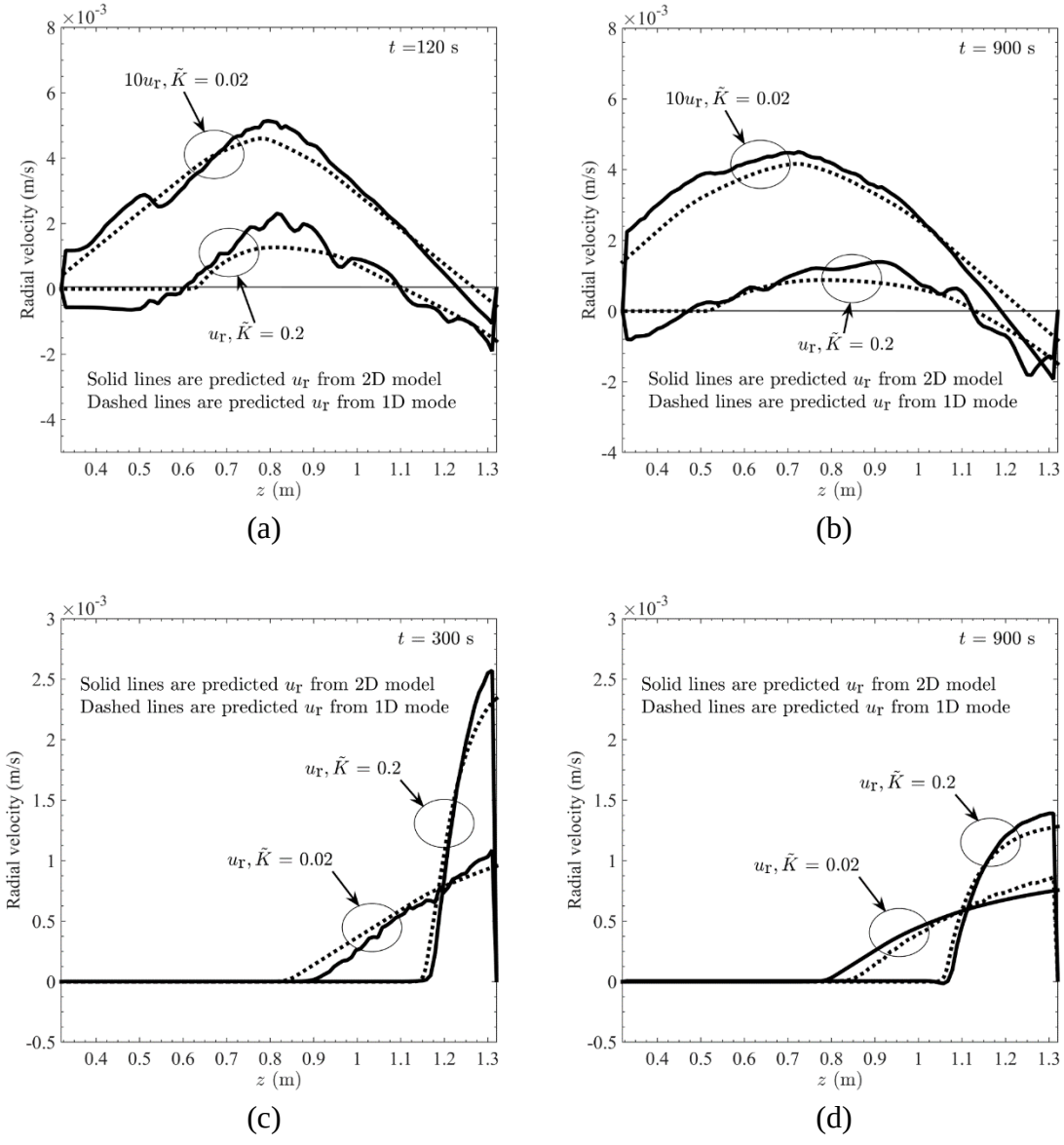

Figure 3.14. Comparison of the radial velocity distributions predicted by the 2-D model and 1-D models: (a) intermediate charging at t = 120 s; (b) intermediate charging at t = 900 s; (c) top charging at t = 300 s; (d) top charging at t = 900 s.

For top charging, we recommend the value of $\tilde{K}$ which ensures that all of the incoming warm fluid is released at a height at or above 95% of the tank height. This value is recommended so as to release the inlet fluid at a depth similar to that of fluid entering the tank through a top-mounted inlet pipe (as a free buoyant jet). As the permeability is increased, the depth of the release will approach the penetration depth for a free buoyant jet, which can be predicted from an empirical correlation developed by Turner, 1966):

$$\frac{z_L}{D} = 1.74\left(\frac{1}{Ri_D}\right)^{0.5} = 1.74\left(\frac{L}{DRi_L}\right)^{0.5} \tag{3.31}$$

For $100 \le Ri_L \le 1000$, z_L is about 1.5 to 4.8% of the tank height. Practically, the benefit of increasing the permeability of the manifold beyond the recommended value becomes marginal as the volume of warm water at the top of the tank grows during charging.

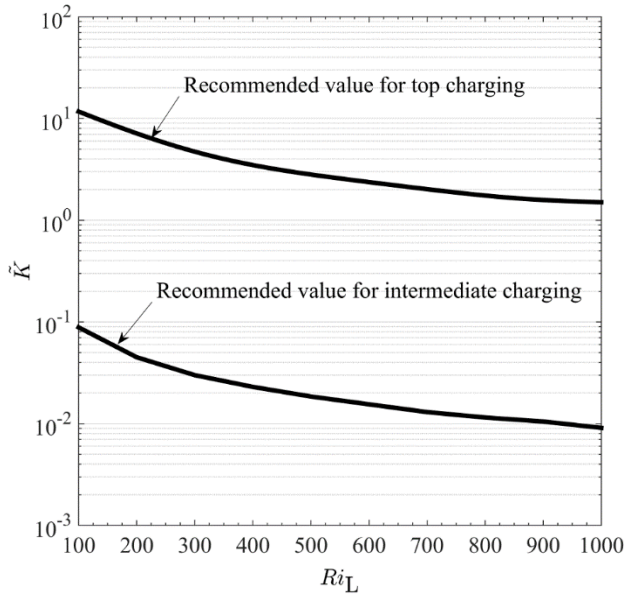

Figure 3.15. Recommended dimensionless permeability for intermediate and top charging over $100 \le Ri_L \le 1000$

The recommended dimensionless permeability is presented in Figure 3.15 for $100 \leq Ri_L \leq 1000$. In agreement with the 2-D model, the recommended permeability depends strongly on charging mode. For all Richardson numbers, lower dimensionless permeability of the order 10^{-2} is recommended for intermediate charging to prevent suction above the thermocline. Dimensionless permeability of order one is recommended for top charging to distribute the incoming fluid to the top of the tank. In general, the recommended values of $\tilde{K}$ decrease with increasing Richardson number, with lower sensitivity to changes in $\tilde{K}$ for $500 \leq Ri_L \leq 1000$. For example, at $Ri_L = 500$, the recommended $\tilde{K}$ for intermediate charging is 0.02 and for top charging the recommended $\tilde{K}$ is 3. At $Ri_L = 1000$, recommended values are 0.009 and 1.5, respectively. In summary, these results demonstrate that the porous manifold is a promising approach to maintain thermal stratification but it is important to consider the operating condition when selecting the design.

3.4. Conclusion

In this study, we investigated the impact of the permeability of a porous manifold on thermal stratification in a water storage tank in comparison to a top-mounted inlet pipe. The performance of the manifold is explored for both intermediate charging and top charging of the tank. Transient distributions of temperature and velocity were predicted for operating conditions and a tank geometry representative of solar domestic hot water systems using a transient two-dimensional CFD model. A one-dimensional model of the manifold allowed parametric study of the effect of permeability for Richardson numbers from 100 to 1000. To ensure operation of the manifold in the buoyancy driven flow

regime, the diameter of a manifold should be selected to ensure Richardson number is greater than 100 for the operating flow rate through the system.

There are two primary findings. First, the porous manifold improves thermal stratification for intermediate charging, regardless of the choice of permeability. Over a large range of Richardson numbers, the manifold is most effective for $\tilde{K} \approx 0.02$. Such a manifold will deliver the fluid to the tank in a narrow band at the vertical position of neutral buoyancy and will prevent suction of warmer fluid stored at the top of the tank into the manifold. Second, for top charging the porous manifold is comparable in performance to a well-designed inlet pipe. This finding is consistent with prior work [9]. Note however that this conclusion assumes that the inlet pipe is adequately large to ensure operating Richardson numbers of the order of at least 100. Alternatively, a conventional inlet pipe may be fitted with a larger diameter distribution manifold to ensure buoyancy driven flow.

In practice, solar storage tanks operate under a range of conditions due the intermittent nature of solar irradiation and hot water use. For this reason, the difference in the impact of permeability on the performance of a porous manifold for intermediate charging and top charging leads to a conundrum for selection of a porous material for this application. Top charging will occur when the energy in the tank has been depleted, but it is highly likely that intermediate charging will occur over much of the day for the collector loop. One choice is to design the manifold to achieve a high dimensionless permeability ($\tilde{K} \sim 0.2$). This choice will always result in an improvement in thermal stratification compared to a top-mounted inlet pipe but will not produce the best results during intermediate charging. If intermediate charging is the dominant mode of

operation, we recommend $\tilde{K}$ on the order of 0.02. Intermediate charging is likely to be the most common mode of operation during solar charging if the tank is adequately sized for the load. It is also a common mode of operation for load side heat exchangers.

Porous plastic or fabric materials are preferred as materials of construction to reduce conduction through the manifold wall and to maintain low thermal mass. Plastic pipes are already used as drop tubes in water storage tanks and there are a number of materials that are certified by the NSF (National Sanitary Foundation) for use with potable water and that are mechanically stable in hot chlorinated water [58]. Sintered porous plastic, reticulated open cell plastic foams, and fabrics are available to provide the recommended permeability. Moreover, plastics do not corrode, rust, and are there is some evidence that scale is less likely to adhere to the surface.

One potential issue of employing the porous-tube manifold in the solar hot water system is that particulates in the water might be trapped in the pores and eventually alter the permeability of the manifold. One possible solution is to install an inline filter upstream of the manifold inlet. This external filter can be replaced periodically if necessary.

Chapter 4

Characterization of a Rigid Porous-tube Stratification Manifold in Comparison to Conventional Inlets

Abstract:

Achieving thermal stratification of storage tanks has well documented advantages for increasing the efficiency and quality of delivered energy of solar heating systems. The present work presents experimental characterization of a porous tube manifold during charging of a water tank under conditions typical of solar hot water systems. Measurements of vertical temperature distributions are used to evaluate the dimensionless exergy efficiency of the manifold in comparison to a conventional inlet pipe and a diffuser. Particle image velocimetry measurements illustrate the fluid dynamic behavior of the three inlet configurations. Results demonstrate that the manifold is superior to the other inlets. It releases the incoming flow at the level of neutral buoyancy, and prevents suction of tank fluid into the manifold at other vertical levels.

Keywords: Thermal stratification, manifold, water heating, storage, porous

4.1. Introduction

Achieving thermal stratification of storage tanks has well documented advantages to increase the efficiency and quality of delivered energy of solar heating systems.

Note: The content of this chapter was published as in Ref. [22]

Stratification of water storage tanks can increase the annual solar fraction of combined solar water/space heating systems (combi-systems) and solar hot water systems by 6 to 38% depending on the design and operating conditions of the system [3,14].

The design of the inlet to the tank has a profound impact on thermal stratification during charging. The major causes of mixing and destratification are jet mixing and plume entrainment [1]. Jet mixing is most prevalent during top charging when the fluid entering the tank is warmer than the fluid stored in the tank. For conventional inlet pipes and flow rates, the Richardson number, which is the ratio of the buoyancy to inertial forces, is less than unity and the inlet jet penetrates deep into the tank and mixing is extensive. Jet mixing is reduced in low flow systems [1] and in tanks with large diameter inlet pipes or diffusers that slow the velocity of the fluid entering the tank. Plume entrainment occurs when the inlet fluid is cooler than the fluid stored at the top of the tank but warmer than the fluid stored at the bottom, referred to as intermediate charging. In this situation, a stratification manifold is beneficial. An effective manifold releases the inlet fluid to the tank at the vertical position where the temperatures are equal (the level of neutral buoyancy) and prevents flow into or out of the manifold elsewhere.

Designing a manifold for variable operating conditions has proven challenging. Over the past 30 years, a number of distribution manifolds have been proposed. The designs include the rigid porous manifold [10,21], the rigid porous manifold with vertical hydraulic resistance elements [4–6,16], flexible porous manifolds [5–7,20], and the rigid pipe with check valves [8,18]. Arguably, the simplest of these designs is a rigid porous-tube manifold. The rigidity of the tube prevents the manifold from collapse, which would encourage suction of tank fluid into the manifold because of the Bernoulli effect in a

flexible porous channel [20]. The porous wall acts as a barrier to reduce shear between the incoming flow and the surrounding tank fluid and allows fluid to flow from the tube at the proper vertical position. The tube can be attached to an inlet diffuser to condition the inlet flow. The present authors applied results of a computational fluid dynamic model of such a manifold to develop design guidelines [21]. The diameter of the tube should be large enough to slow the average velocity into the tube, *U*, to achieve a Richardson number of 100 or higher. The Richardson number is defined as

$$Ri_{\mathrm{L}} = \frac{gL\beta\left(T_{\mathrm{H}} - T_{\mathrm{C}}\right)}{U^2}. \tag{4.1}$$

The relevant scales are the height of the tank, *L*, and the average inlet velocity, *U*. For selection of the porosity and pore structure of the tube, the key design parameter is the dimensionless permeability [20,21], defined by eqn. (4.2), which is the ratio of the radial pressure drop and the vertical pressure drop in the tube.

$$\tilde{K} = \frac{16L\dot{m}}{\pi\mu D_{\mathrm{i}}^3}\frac{K}{\delta} \tag{4.2}$$

Here, *K* is the permeability of the porous tube, δ is the thickness of the tube wall, and D_i is the inner diameter of the tube. Figure 4.1 shows the recommended design values of for $100\text{-} \leq Ri_{\mathrm{L}} \leq 1000$ for top and intermediate charging [21]. For intermediate charging, the optimum $\tilde{K}$ ensures fluid flows into the tank at the height of neutral buoyancy and eliminates suction into the manifold. A higher will allow suction of warmer tank fluid stored at the top of the tank into the manifold, whereas a lower $\tilde{K}$ will allow release of the inlet fluid over a larger region, both above and below the height of neutral buoyancy. In the limit, if $\tilde{K}$ is too low, the manifold will act as a diffuser releasing fluid over the

entire height of the tank. For top charging, the recommended $\tilde{K}$ will ensure release of fluid in the top 20% of the tank. We recommend a value of $\tilde{K}$ that falls between the two curves to balance performance for top and intermediate charging. The difference between the recommended values of $\tilde{K}$ becomes smaller as Richardson number is increased.

In the present work, we extend our prior computational work to design and demonstration of a porous-tube manifold for both top and intermediate charging of a water storage tank. The performance of the manifold is compared to that of a conventional inlet pipe, and an inlet diffuser at conditions typical of solar hot water systems. A dimensionless exergy efficiency based on measured temperature distributions quantifies stratification. The fluid dynamic behavior, specifically plume entrainment and suction into the manifold, is interpreted from particle image velocimetry (PIV) measurements of the velocity field.

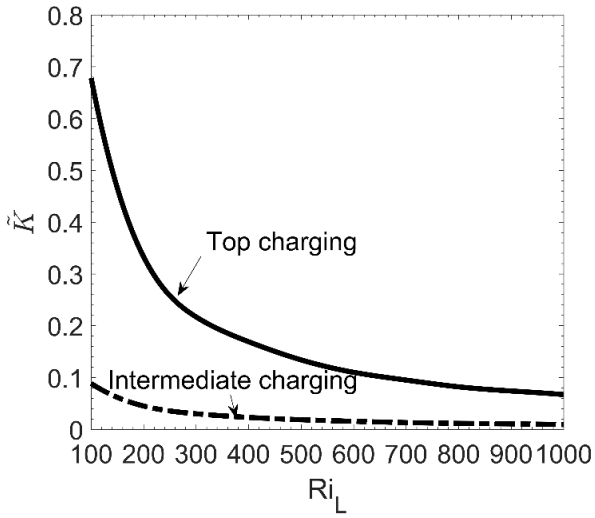

Figure 4.1 Guideline for selection of the dimensionless permeability versus Richardson number

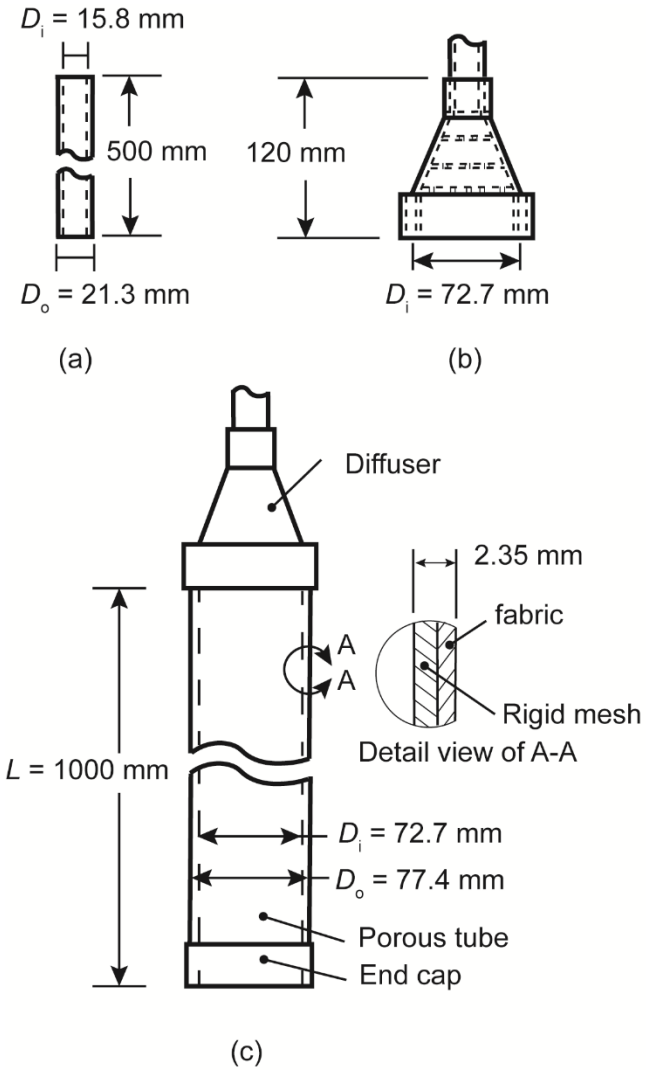

Figure 4.2 Inlet configurations: (a) inlet pipe, (b) inlet pipe with diffuser, (c) porous-tube manifold (Not to scale)

4.2. Experimental Method

4.2.1 Inlet Configurations

Figure 4.2 shows the three inlet configurations. The inlet pipe (Figure 4.2 (a)) is a schedule 40 PVC pipe with D_i = 15.8 mm and D_o = 21.3 mm, typical of a conventional

system. The pipe is approximately 500 mm long upstream of the tank to ensure fully developed flow into the tank.

The inlet diffuser (Figure 4.2(b)) provides a transition from the inlet pipe to a larger outlet diameter, D_i = 72.7 mm. It slows the jet into the tank and provides a uniform velocity profile. It was 3-D printed of acrylonitrile butadiene styrene (ABS). (A material with greater chemical resistance to chlorinated water would be required in practice.) The diverging section of the manifold contains three perforated plates, each with 3.175 mm diameter circular perforations and 30% open area, to provide a uniform velocity profile. The ability of the diffuser to provide a uniform velocity profile was evaluated with PIV at 20 ^{o}C at the same inlet mass flow rate as the charging experiments (0.07 kg/s). The velocity profile is nearly Gaussian, typical of round jets [59]. The mean velocity is 0.02 m/s.

The porous-tube manifold includes the inlet diffuser (Figure 4.2(c)). The 1 m long porous tube is a rigid polypropylene (PP) mesh tube covered with 0.1 mm thick acrylic plain weave fabric (style 864 with spun Orlon Type 75 acrylic yarn) [60]. The outer diameter, D_o, is 77.4 mm and the inner diameter is 72.7 mm. The PP mesh provides supports the fabric and prevents the tube from collapsing. The mesh has a 50% open area and 1.5 mm wire diameter arranged in an isotropic square pattern in the longitudinal and circumferential directions. The weighted end cap at the bottom of the tube forces fluid to enter the tank through the porous tube and holds the manifold vertically in the tank. The dimensionless permeability of the manifold was determined from measurements of the pressure drop across a flat sample of the tube (rigid mesh with fabric) as a function of the

Darcy velocity u_D through the sample. Using the Deming regression method to fit the data to Darcy's Law (eqn. (4.3)), $K/\delta = 7.75\times10^{-8} \pm 0.39\times10^{-8}$ m/s.

$$\frac{K}{\delta} = \frac{\mu}{\Delta p} u_D \tag{4.3}$$

In eqn. (3), K is the permeability, and δ is the thickness of the porous structure, and u_D is the velocity across the porous material. For the mass flow rate used in the present study ($\dot{m} = 0.07$ kg/s). The viscosity of water was evaluated at 33 ℃.

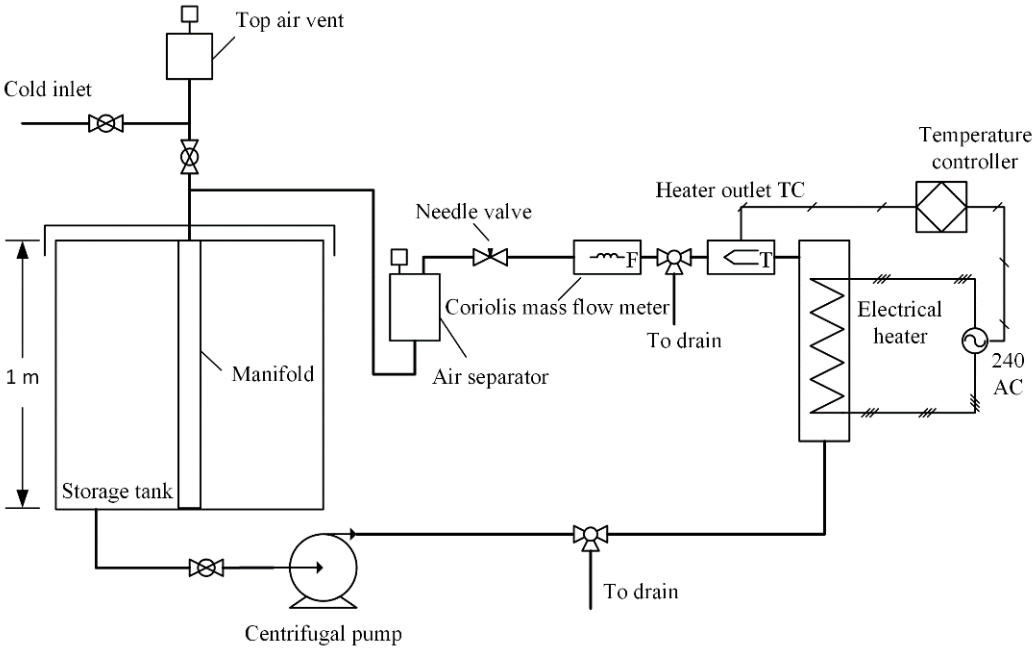

Figure 4.3 Flow loop for charging experiments. The storage tank is1 m^3. The base of the tank is 1020 mm by 1020 mm. (Not to scale)

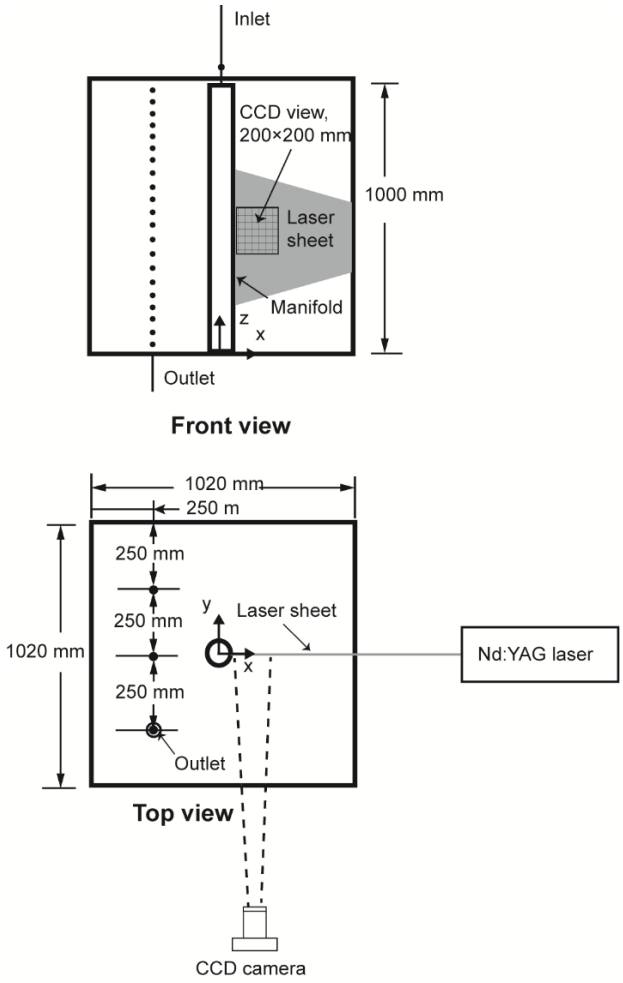

Figure 4.4 Arrangement of thermocouples and PIV system (Not to scale). Thermocouples are represented by solid dots.

4.2.2 Flow circuit and instrumentation

Figure 4.3 is a schematic of the closed flow loop for charging. Water was pumped from the bottom of the tank, heated in a PID temperature-controlled 11.3 kW inline electrical boiler, and then delivered to the inlet. The mass flow rate was monitored with a Coriolis mass flow meter (±0.001 kg/s). The 1 m^3 storage tank was constructed of 12.7 mm thick annealed glass panels. It is insulated with 50.8 mm thick extruded polystyrene foam (R-1.76 m^2 K/W) except for two small sections required for optical access of the

PIV. The overall heat loss coefficient (UA) is 5 W/K. The tank heat loss is less than 2% of the energy input through charging. The inlet is located at the center of the top of the tank. The outlet is offset from center at the bottom of the tank.

Vertical and horizontal water temperature distributions were measured by 29 thermocouples attached to three thermocouple trees (Figure 4.4). The vertical temperatures were measured with 21 T-type (copper-constantan, insulated, 36 AWG) thermocouples spaced at 50 mm vertical intervals midway between the manifold and tank wall. Horizontal temperature distributions were measured along the other two thermocouple trees at 250 mm horizontal spacing (Figure 4.4). Each of these two thermocouple tress has four thermocouples at z = 200, 400, 600, and 800 mm. For all experiments, the water temperatures were within measurement uncertainty in the horizontal plane. The inlet water temperature was monitored with a T-type thermocouple positioned in the pipe 100 mm above the diffuser. The thermocouple and the mass flow meter signals were recorded at 0.1 Hz.

The velocity field at various positions in the tank was measured using a 2-D PIV system (see Figure 4.4). During charging with the inlet pipe and the diffuser, these data elucidate the interaction of the descending inlet jet with the thermocline in the tank. For the manifold, the measurements were obtained near the top of the tank to illustrate the ability of the manifold to reduce suction from the tank into the manifold. The PIV system includes a double pulse Nd:YAG laser, laser optics, a 4 megapixel CCD camera (with a 10 nm band filter), a signal synchronizer and a computer. The vertical laser sheet was aligned with the center axis of the manifold as shown in Figure 4.4. The camera provided a field of view of 200 by 200 mm. The water was seeded with 10 μm hollow

glass spheres at a concentration of 0.8 g/m^3. Ensemble measurements over 4 seconds were taken at 7.5 Hz. The change of the tank temperature during each ensemble PIV measurement is negligible. The time-averaged velocity data of the ensemble measurement was used to calculate the key quantities such as the relative depth of penetration of the inlet jet into the thermocline and suction/entrainment rate of the manifold. PIV measurement and data processing were performed in the software—INSIGHT 3G. The recursive Nyquist scheme using a final interrogation spot size of 32 by 32 pixels and a spatial resolution of 1.7 mm is employed. For a better visual presentation of the data, the resolution of the velocity vector field was reduced to 6.8 mm. The uncertainty of the velocity is approximately 3.5% of maximum velocity measured for inlet pipe and diffuser experiments. For the manifold, the uncertainty is 10.2% of the maximum measured velocity.

4.2.3 Charging Procedure

Table 4.1 lists the operating conditions and dimensionless parameters for each test. The test conditions are representative of the flow rates and temperatures of conventional domestic solar hot water systems. The inlet mass flow rate was 0.07 kg/s based on 0.015 kg/s/m^2 for a collector area of 4.7 m^2, typical for a single family. For intermediate charging, the tank was thermally stratified in two equal volumes with T_H = 46 °C and T_C = 20 °C. The initial thermocline between these layers was 300 mm thick between 400 mm $\leq z \leq$ 700 mm. The inlet fluid temperature was T_{in} = 33 °C. For top charging, the tank was initially isothermal at T_C = 20 °C and T_{in} = 46 °C (T_H). Charging continued over 1.5 to 2 hours until the tank was fully mixed or half of the volume stored in the tank was displaced by the incoming flow.

Table 4.1 Operating condition of top and intermediate charging

Charging mode	$\dot{m}_{in}$ (kg/s)	T_{in} (°C)	T (°C)	Re_D[1]			Ri_L[1]		
				Pipe	Diffuser	Manifold	Pipe	Diffuser	Manifold
Inter-mediate	0.07	33	T_C=20; T_H=46	7730	1680	1680	0.5	292	292
Top	0.07	46	20	7730	1680	1680	0.5	292	292

[1] Fluid properties are evaluated at $(T_C + T_H)/2$

4.2.4 Performance Metrics

Thermal stratification is quantified by the exergy efficiency [54–56]. The specific exergy carried by the fluid neglecting the kinetic and potential exergy is

$$\begin{aligned} e_x &= (h - h_o) - T_o (s - s_o) \\ &= c_p \left[(T - T_o) - T_o \ln\left(\frac{T}{T_o}\right) \right] \end{aligned} \tag{4.4}$$

where T_o is the dead state temperature set to an assumed supply temperature of 20 °C. The exergy of the water stored in the tank was determined by trapezoidal numerical integration of the vertical temperatures. This approach is justified since temperatures in the horizontal planes were uniform.

$$E_x = \iiint_{CV} e_x dv = A \int_{z=0}^{z=L} e_x dz = \frac{1}{2} \sum_{i=1}^{N=22} (z_{i+1} - z_i) \left[e_{x,i} + e_{x,i+1} \right] \tag{4.5}$$

The dimensionless exergy efficiency provides a measure of exergy relative to two extreme conditions, one of perfect stratification ($E_{x,st}$) and the other of a fully mixed tank ($E_{x,\,mix}$).

$$E_x^* = 1 - \frac{E_{x,st} - E_x}{E_{x,st} - E_{x,mix}} \tag{4.6}$$

The fully mixed tank temperature is based an overall energy balance of the tank.

$$T_{\text{mix}} = \frac{\int_{z=0}^{z=L} \rho c_p T dz}{L \rho_{mix} c_{p,mix}} \tag{4.7}$$

$E_{\text{x,st}}$ is calculated using the ideal tank temperature distribution predicted by a plug flow model [57]. In the ideal plug flow model, the tank is partitioned into segments of uniform temperatures. Fluid enters the tank at the level of neutral buoyancy without mixing. The positions of all existing segments between inlet and outlet are then shifted into segments of equal temperature. $E_{\text{x}}^{*} = 1$ is the maximum possible stratification efficiency, and $E_{\text{x}}^{*} = 0$ indicates the tank is completely mixed.

The thermocline is a visual indicator of the degree of stratification. The upper and lower boundaries of the thermocline are defined as the height at which dT/dz equals 5% of the maximum dT/dz within the tank.

The velocity data obtained from PIV measurement are analyzed to quantify the relative entrainment rate ($M_{\text{e,pipe}}$, $M_{\text{e,diffuser,}}$ and $M_{\text{e,manifold}}$) under intermediate charging. The relative entrainment rate represents the mass flow rate of fluid above the thermocline that is mixed with the incoming flow. For the inlet pipe and diffuser, tank fluid is entrained into the descending plume. The relative entrainment rates $M_{\text{e,pipe}}$ and $M_{\text{e,diffuser}}$ are calculated using the vertical velocity distribution $w(r)$ at the upper boundary of the thermocline, z_{up}. The edge of the plume is at r_{e}. The net entrainment rate is obtained by subtracting the inlet mass flow rate $\dot{m}$ from the mass flow rate of the descending plume as indicated by eqn. (4.8).

$$M_{e,pipe/diffuser} = \frac{2\pi \int_0^{r_e} \rho w(r) r dr - \dot{m}}{\dot{m}} \tag{4.8}$$

For the manifold, the suction velocity in the radial direction (u) at $r = D_o/2$ is assumed to be uniform circumferentially.

$$M_{e,manifold} = \frac{\pi D_o \int_{z_{up}}^{L} -\rho u dz}{\dot{m}} \tag{4.9}$$

4.3. Results

The transient behaviors of the three inlet options during intermediate and top charging are presented for the operating conditions listed in Table 4.1.

4. 3.1 Intermediate charging

Figure 4.5 compares the evolution of the vertical distribution of water temperature of the inlet pipe (Fig. 4.5(a)), the diffuser (Fig. 4.5(b)), and the manifold (Fig. 4.5(c)) during intermediate charging. On the ordinate, z = 0 mm is the bottom of the tank and z = 1000 mm is the top. To put these data in perspective, dashed lines indicate the temperature distribution that would be achieved for an idealized plug flow for 30 and 90 minutes. Initially, the tank was stratified with the upper portion of the tank at 46 ^{o}C and the lower portion at 20 ^{o}C. The thermocline extended vertically over 400 mm $\leq z \leq$ 700 mm.

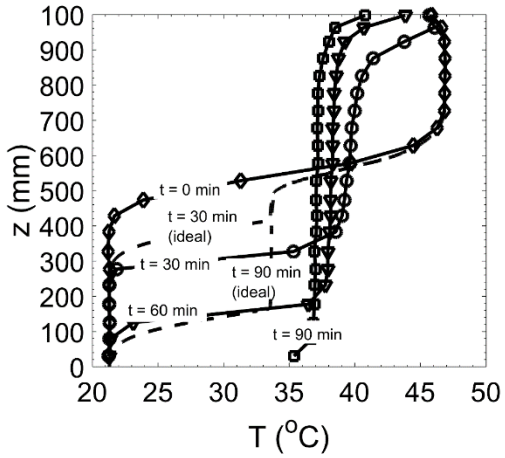

(a)

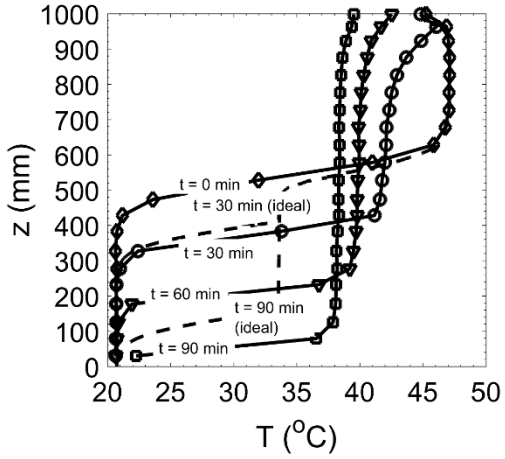

(b)

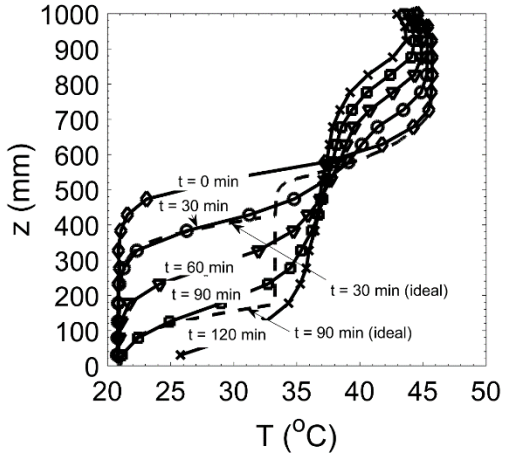

(c)

Figure 4.5. Temperature distributions for intermediate charging: (a) inlet pipe, (b) diffuser, (c) manifold

First we consider the temperature and velocity distributions for the inlet pipe. Water enters the tank at 33 ^{o}C. The average inlet velocity is 0.36 m/s, corresponding to Ri_L = 0.5. For this Richardson number, inertial forces are greater than buoyancy forces. As the jet descends, it mixes with the warmer water stored in the upper portion of the tank. Water below the thermocline remains at the initial temperature of 20 ^{o}C. The restriction of mixing to the warmer region of fluid above the thermocline indicates the descending inlet plume does not destroy the thermocline. However, as will be shown by the PIV data, the jet penetrates the upper boundary spreads horizontally within the thermocline. Consequently, the thermocline thins as charging proceeds. The temperature gradient across the thermocline remains at approximately 180 ^{o}C/m throughout charging. The test was terminated at t = 90 minutes when the thermocline had been pushed to the bottom of the tank. At this time, the tank was nearly isothermal at 37 ^{o}C. In the ideal scenario captured by the plug flow model, the tank would remain thermally stratified with a fluid layer at 33 ^{o}C growing from z = 480 mm towards the bottom of the tank.

The impact of adding a diffuser on the transient temperature distribution is shown in Figure 4.5(b). The diffuser reduces the inlet velocity to 0.018 m/s and Ri_L = 292. Buoyant forces dominate the behavior of the descending plume. Mixing above the thermocline slows compared to that observed with the inlet pipe. Again, there is no mixing below the thermocline. At t = 30 minutes, the top 700 mm of the tank is mixed. At t = 90 minutes, the fully mixed region extends over 90% of the height of the tank. The test was terminated at t = 105 minutes when the tank was fully mixed at 38 ^{o}C.

The porous manifold provides a dramatic improvement in thermal stratification. The inlet velocity and Richardson number are identical to those values for the diffuser.

The temperature data illustrate the two important functions of the manifold: i) the inlet fluid is released at the appropriate height within the thermocline, and ii) direct mixing of the inlet fluid and the tank fluid is minimized. As shown in Figure 4.5(c), as charging proceeds, the thickness of the thermocline expands toward both the top and the bottom of the tank. This thickening is due to the flow of water from the manifold between the warmer and cooler layers in the tank. Very little fluid is sucked (entrained) into the manifold. Suction is discussed in more detail in the presentation of the PIV data, but the temperature data support our finding of low suction rates. Over the course of charging, fluid in the upper portion of the tank cools only slightly, from 45-46 ^{o}C to 43 ^{o}C. At t = 30 minutes, the fluid at the top of the tank (800 mm $\leq$ z $\leq$ 1000 mm) remains at the initial temperature. At t = 90 minutes, water in the top of the tank (800 mm $\leq$ z $\leq$ 1000 mm) is 44 ^{o}C compared to 37 to 39 ^{o}C for the inlet pipe and diffuser. The tank remains stratified for 120 minutes compared to 90 minutes for the inlet pipe and diffuser.

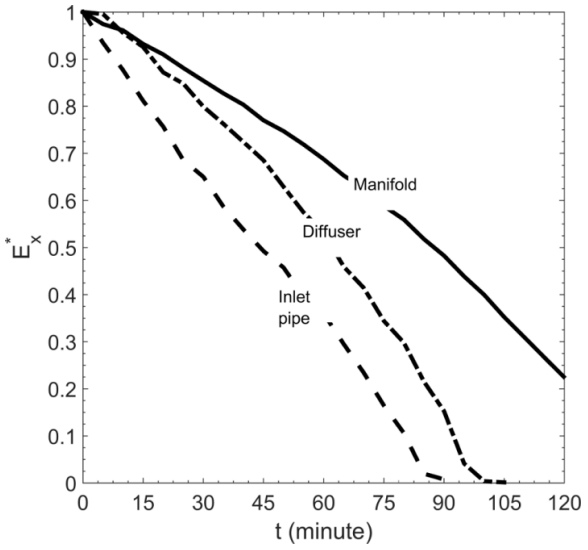

Figure 4.6 Exergy efficiency of the inlet pipe, diffuser, and manifold for intermediate charging

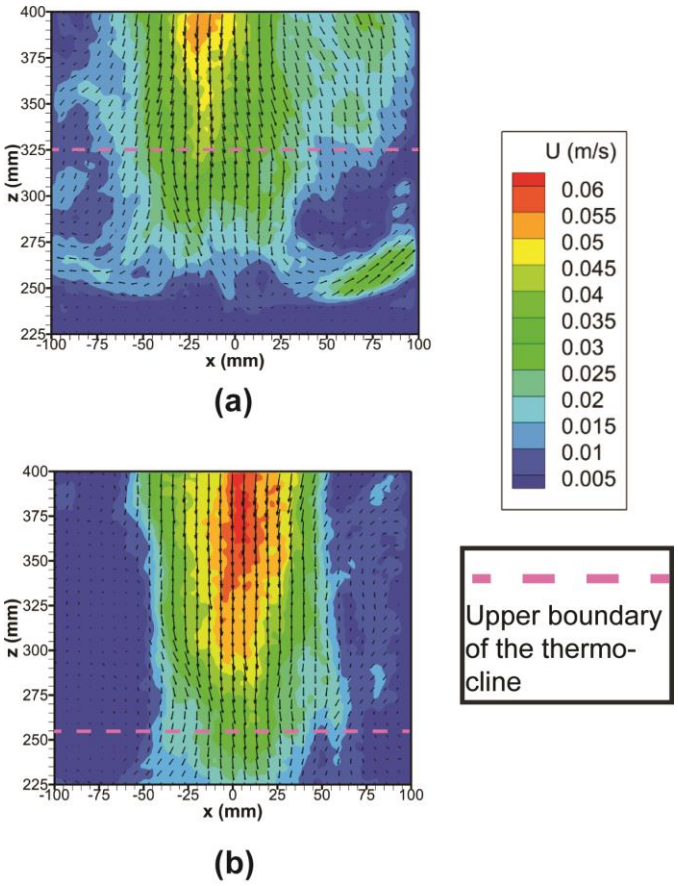

Figure 4.7 Velocity field of the inlet pipe shown in the region of the thermocline: (a) t = 45 min; (b) t = 60 min. Arrows indicate the velocity vectors and the color contours represent the velocity magnitude. The dashed (pink) horizontal line represents the upper boundary of the thermocline and the solid pink line represents the upper boundary of the thermocline.

A quantitative comparison of the performance of the three inlet configurations is provided by the dimensionless exergy efficiency, which is plotted versus charging time in Figure 6. In the ideal case, represented by the plug flow, the exergy efficiency is unity. For the actual situation, exergy efficiency decreases from E_x^* = 1 as the tank is charged to a fractional value bounded by zero, representing a fully mixed isothermal tank. The manifold provides the best performance with the slowest rate of decline in exergy

efficiency. After one hour, exergy efficiency is 0.7 and at the end of the two-hour charging experiment, the exergy efficiency is 0.22. The exergy efficiency of the diffuser decreases more rapidly; E_x^* = 0.55 at t = 60 minutes and E_x^* = 0 at t =100 minutes. The inlet pipe has the poorest performance; E_x^* = 0.35 at t = 60 minutes and E_x^* = 0 at t = 90 minutes.

The velocity fields are presented in Figures 4.7 through 4.9. First consider the inlet pipe (Figure 4.7). The field of view, $225 \leq z \leq 400$ mm, illustrates the interaction of the inlet jet and the thermocline. At t = 45 minutes, the inlet jet penetrates the upper surface of the thermocline at z = 325 mm (indicated by a horizontal dashed line). The mean velocity of the jet slows from 0.36 m/s to 0.02 m/s as the jet spreads laterally. Mixing due to the lateral spread of the buoyant plume thins the thermocline. The cooler fluid lower in the thermocline is not disturbed. The lower boundary of the thermocline is at z = 130 mm (not shown). As charging process proceeds, the plume and the thermocline both move deeper in the tank. At t = 60 minutes, the upper and lower boundaries of the thermocline are z = 255 mm and z = 55 mm, respectively. Figure 4.7(b) shows the inlet jet still penetrates the thermocline at this depth. The relative entrainment rate $M_{e,pipe}$ = 4 at 45 minutes and $M_{e,pipe}$ = 3 at 60 minutes.

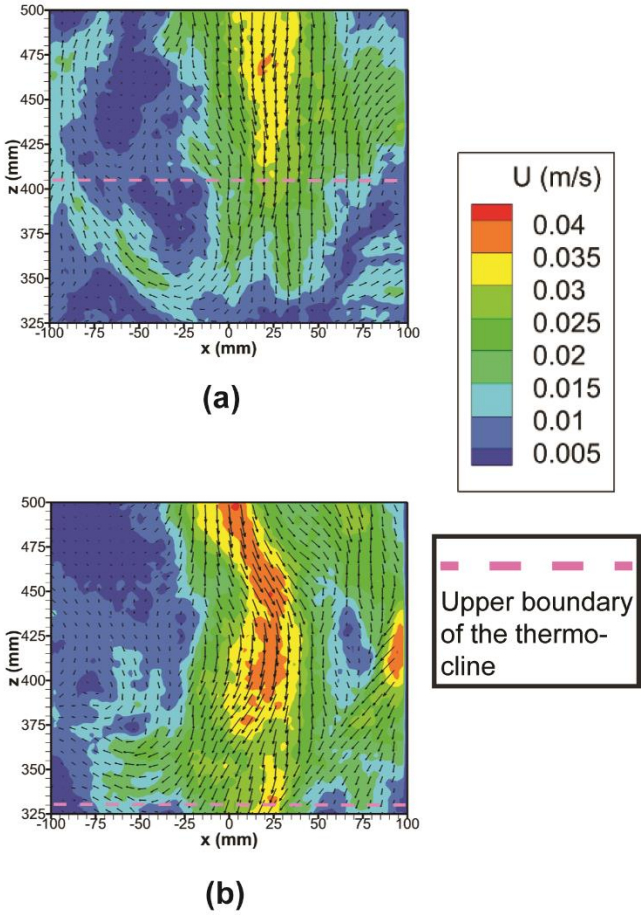

Figure 4.8 Velocity field near and above the upper boundary of thermocline for the diffuser under intermediate charging; (a) t = 45 minutes;(b) t = 60 minutes. Arrows indicate the velocity vectors and the color contours represent the velocity magnitude. The dashed (pink) horizontal line represents the upper boundary of the thermocline and the solid pink line represents the upper boundary of the thermocline.

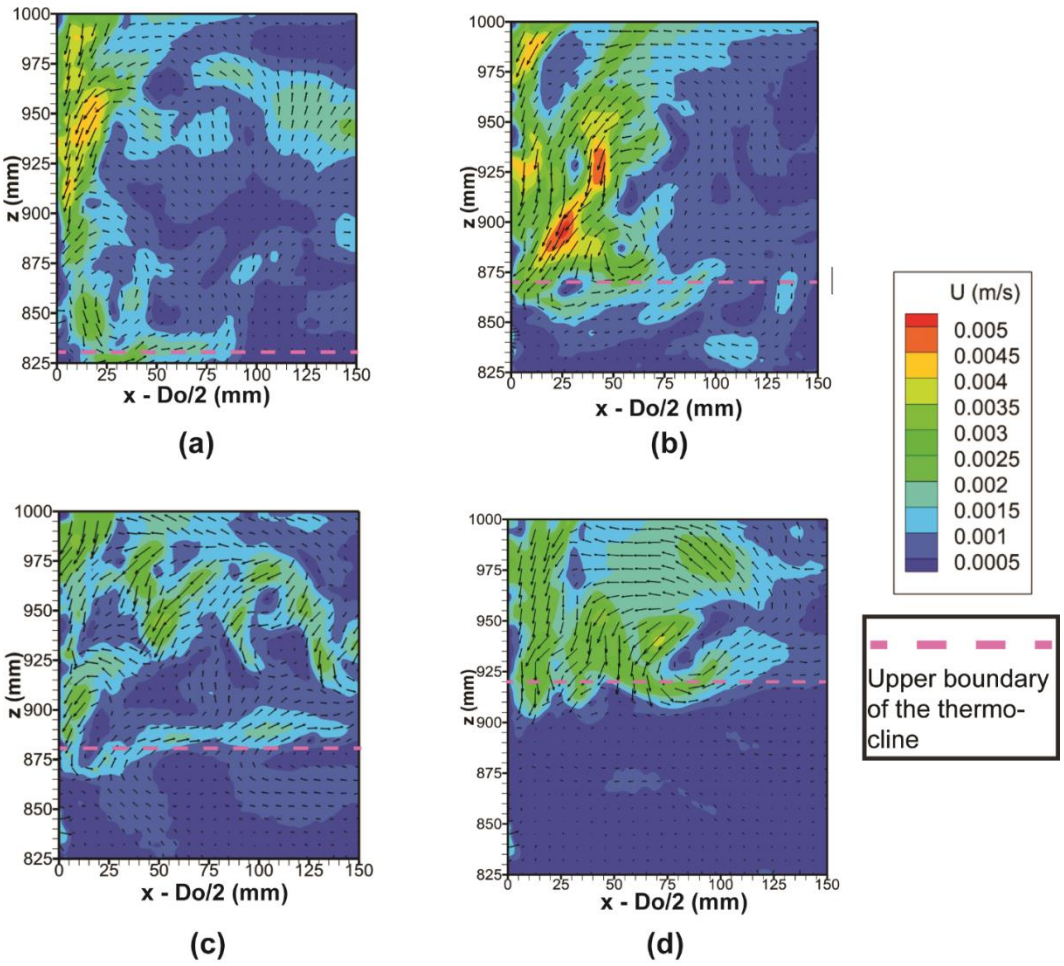

Figure 4.9 Velocity field at the top of the manifold under intermediate charging; (a) t = 30 minutes; (b) t = 45 minutes; (c) t = 60 minutes; (d) t = 90 minutes. Arrows indicate the velocity vectors and the color contours represent the velocity magnitude. The dashed (pink) horizontal line represents the upper boundary of the thermocline and the solid pink line represents the upper boundary of the thermocline.

Figure 4.8 shows the flow field for the diffuser. At t = 45 minutes, the thermocline is between 175 mm $\leq z \leq$ 410 mm. The descending buoyant plume penetrates the upper boundary and reaches z = 325 mm as it spreads laterally. At 60 minutes, the upper boundary has descended to z = 330 mm. The relative entrainment rate is about half that of the inlet pipe; at t = 45 minutes $M_{e,diffuser}$ = 1.6 and at 60 minutes, $M_{e,diffuser}$ = 1.5.

Figure 4.9 shows velocity data for the manifold for 800 mm ≤ z ≤ 1000 mm, including a portion of the thermocline. The confined buoyant flow in the manifold increases the momentum of the descending plume relative to the momentum of a free jet, leading to a pressure difference that favors suction into the manifold. However, the suction velocity is slow, on the order of 0.0001 m/s. The relative entrainment due to suction is an order of magnitude lower than with the inlet pipe or diffuser; $M_{e,manifold} = 0.2$ at 45 minutes and $M_{e,manifold} = 0.3$ at 60 minutes. Water in the upper portion of the tank flows slowly (0.001 – 0.004 m/s) along the outer surface of the manifold. This flow structure produces very little mixing. As charging process proceeds, the thermocline expands and descends as fluid continues to flow into the tank.

4.3.2 Top charging

Figure 4.10 shows the transient temperature distributions during top charging. Initially, the tank was isothermal at $T_t = 20$ °C. Again, dashed lines represent the ideal temperature distribution based on a plug flow model.

With the inlet pipe, the temperature of the upper portion of the tank (z ≥ 650 mm) reaches 33 °C at $t = 60$ minutes and 37 °C at $t = 120$ minutes. The temperatures are cooler than the incoming temperature of 46 °C, indicating strong mixing. The thermocline thickness expands from 450 ≤ z ≤ 625 mm at $t = 60$ minutes to 250 mm ≤ z ≤ 600 mm at $t = 120$ minutes. The expansion of the thermocline is due to jet mixing. The water temperature below the thermocline remains at 20 °C.

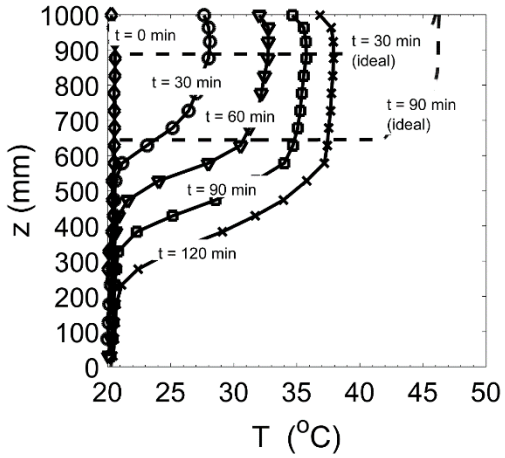

(a)

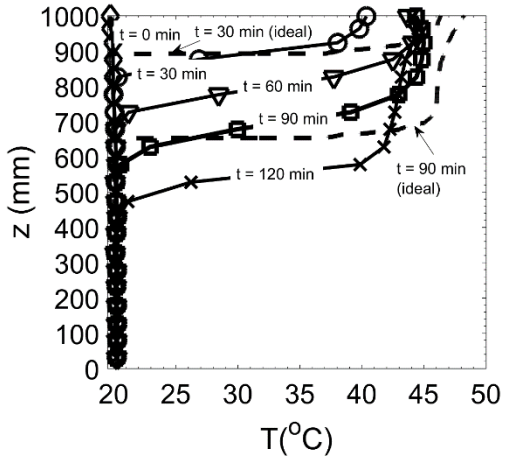

(b)

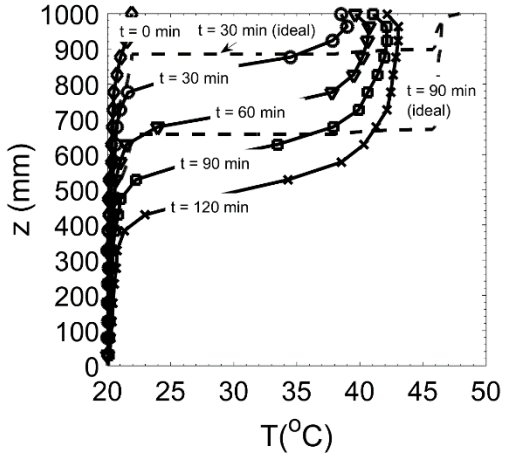

(c)

Figure 4.10 Temperature distributions for top charging: (a) inlet pipe, (b) diffuser, (c) manifold

With a much lower inlet velocity (0.018 m/s), the diffuser achieves warmer temperatures at the top of the tank. After about 30 minutes, the thermocline thickness stabilizes at ~200 mm, much thinner than that for the inlet pipe. At t = 60 minutes, $T \geq 43$ ^{o}C for z $\geq$ 850 mm. At t = 120 minutes, T = 42 - 44 ^{o}C for z $\geq$ 625 mm.

The performance of the porous-tube manifold is similar to that of the diffuser. Due to release of the hot inlet fluid slightly deeper in the tank, the thickness of the thermocline increases and the water temperature above the thermocline is about 2-3 degrees cooler. At t = 60 minutes, $T \geq 41$ ^{o}C for z $\geq$ 850 mm. At t = 120 minutes, the temperature of the tank above 700 mm is 42 ^{o}C. The thermocline is between 400 mm $\leq$ z $\leq$ 700 mm.

Figure 4.11 compares the exergy efficiency of the three inlet configurations. For each, drops from unity to a minimum value within the first few minutes, and then recovers to a higher value. The initial drop corresponds to rapid mixing at the beginning of the charging prior to establishment of a thermocline. Once established, the thermocline acts as barrier to prevent the incoming fluid from mixing with the cool fluid in the lower portion of the tank. The diffuser maintains $E_x^* > 0.6$ for $t \geq 30$ minutes. The manifold's performance is equivalent, achieving $E_x^* \geq 0.55$ for $t \geq 30$ minutes. The performance of the inlet pipe is significantly worse. After reaching a minimum of 0.03, E_x^* slowly increases to 0.3 for t $\geq$ 90 minutes.

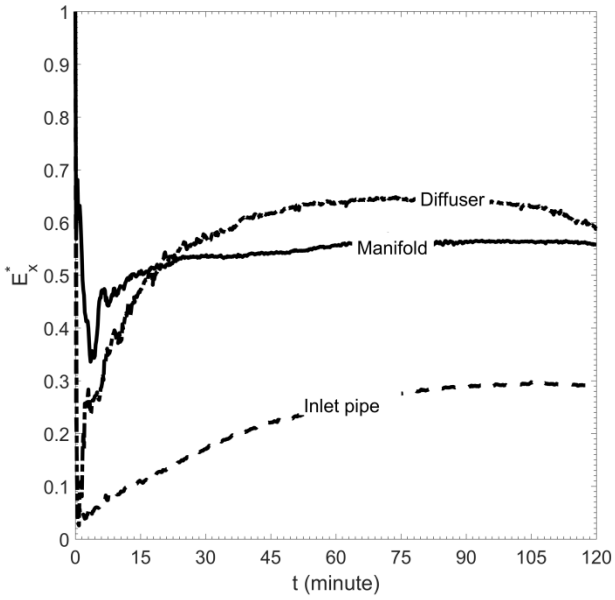

Figure 4.11 Exergy efficiency of the inlet pipe, diffuser, and manifold for top charging

The velocity fields for the three inlets are shown in Figures 4. 12-14. For the inlet pipe, velocities are presented over the region 820 mm ≤ z ≤ 960 mm ($2.5D_o$ – $11.4D_o$ from the pipe exit) to capture the behavior of the jet in the near field. At the exit of the pipe, the centerline velocity is 0.72 m/s. As the jet descends into the tank, it spreads from 15.6 mm at the exit to 40 mm at z = 820 mm and the velocity slows to 0.15 m/s. The jet has sufficient momentum to penetrate beyond the depth shown in the figure and mix with cooler fluid lower in the tank. Due to the low Richardson number, the change in transient temperature distribution does not affect the behavior of the jet. The shape and velocity profile of the incoming jet are nearly identical at t = 60 minutes (Figure 4.12(a)) and 90 minutes (Figure 4.12(b)).

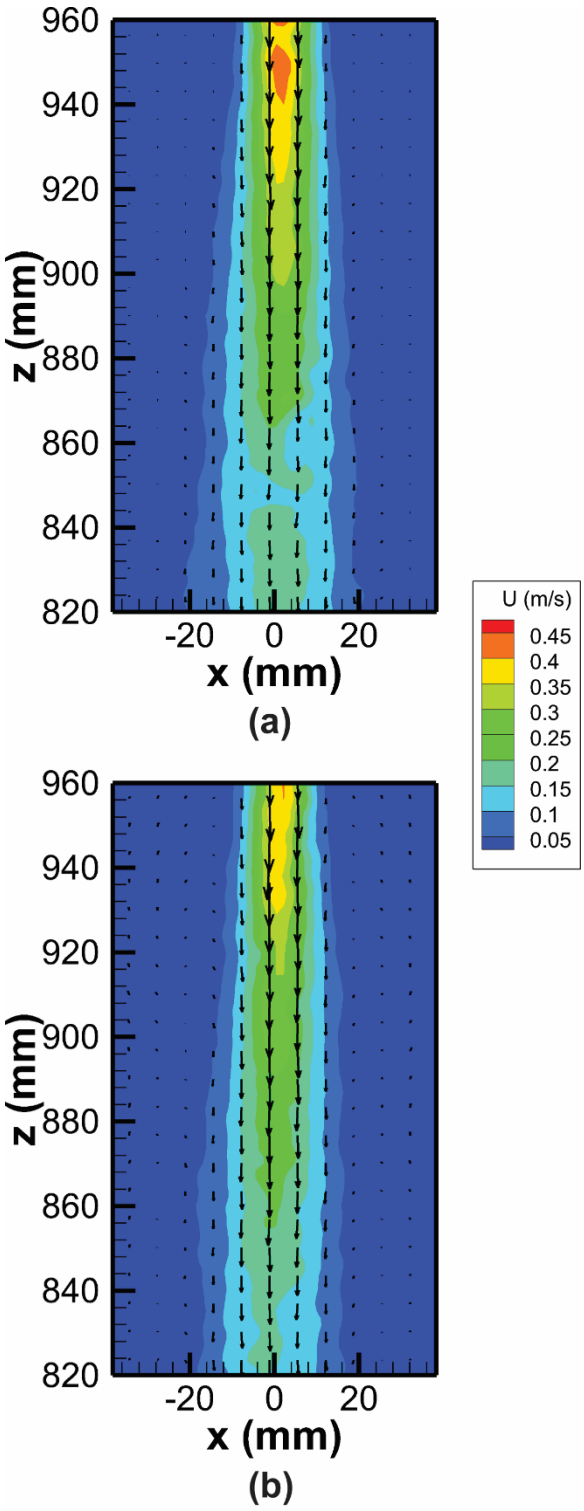

Figure 4.12 Velocity field of the inlet pipe under top charging at (a) 60 minutes and (b) 90 minutes.

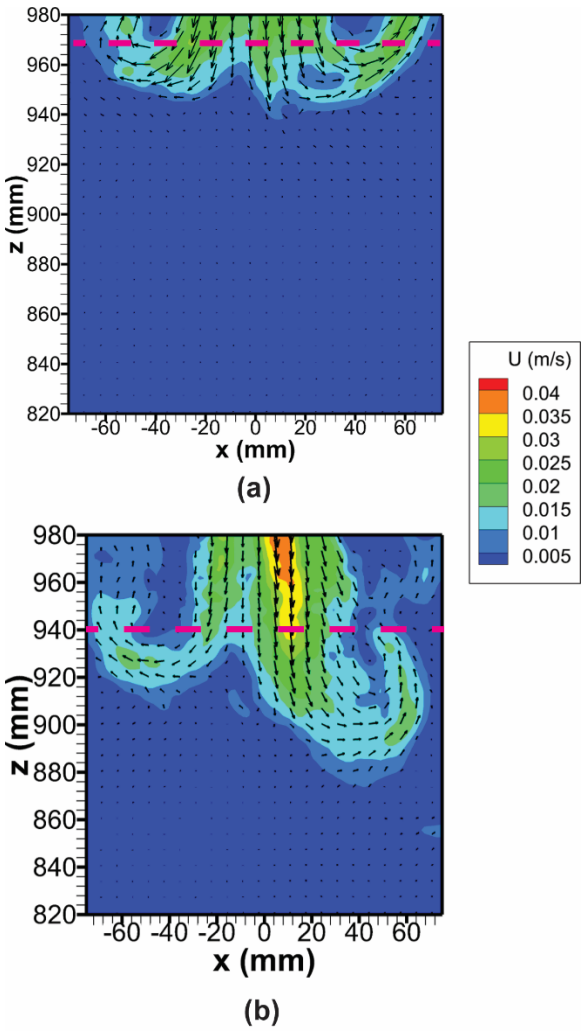

Figure 4.13 Velocity field of the diffuser under top charging at (a) 45 minutes and (b) 60 minutes.

With the diffuser, the velocity into tank is 0.018 m/s and Ri_L = 292. The buoyancy force opposes the downward trajectory of the jet. Consequently, the depth of penetration is less than that with the inlet pipe. At t = 45 minutes (Figure 4.13(a)), the depth of penetration is 60 mm. Once the jet reaches this depth, it turns upward due to buoyancy forces. As charging proceeds, the upper portion of the tank becomes warmer, reducing the buoyancy force. As a result, the incoming jet penetrates deeper into the tank, and the magnitude of the vertical velocity increases. At t = 45 minutes, the jet velocity at the

upper boundary of the thermocline (z = 970 mm) is 0.02 m/s. At t = 60 minutes, the velocity is 0.03 m/s, and the depth of penetration is 120 mm. Although the depth of penetration increases over time (i.e. the region of mixing expands), the difference between the temperature of the incoming flow and the top of the tank decreases. As a consequence, the destruction rate of exergy remains steady throughout the charging process as shown in Figure 4.11.

For the manifold, the PIV data show the velocity field adjacent to the outer wall of the tube. Figure 4.14 shows warm fluid rising along this surface. The radial component of velocity at the manifold wall is not discernable in the image but is on the order of 0.00001 m/s. The vertical component of velocity of the rising plume is 0.002 – 0.006 m/s. At 60 minutes, the fluid is released above z = 800 mm, corresponding to a depth of penetration of 200 mm. At 90 minutes, the depth of penetration is 260 mm. Because most of the incoming fluid is released in the upper portion of the tank, the overall performance of the manifold is comparable to that of the diffuser.

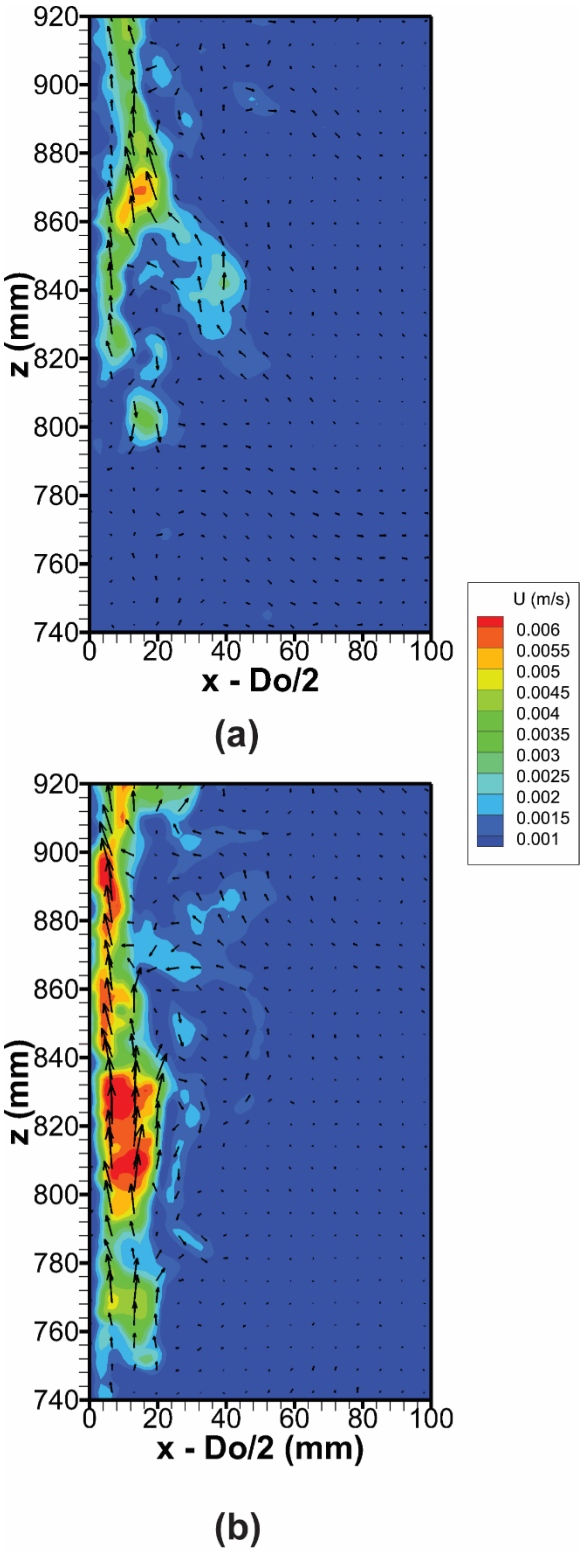

Figure 4.14 Velocity field in the mid-section of the tank under top charging with the inlet pipe at (a) 60 minutes and (b) 90 minutes

4.4. Conclusion

The rigid porous-tube manifold is a simple (no moving parts) and effective solution for stratification enhancement. The data presented in the present study quantify the ability of a rigid porous manifold to maintain thermal stratification under operating conditions typical of charging of a domestic solar hot water storage tank. The benefit of the manifold in comparison to a simple smaller diameter inlet pipe, and an inlet diffuser is proven for both intermediate and top charging. The experimental study extends and validates prior work in which computational fluid dynamics was applied to explain how the manifold works and to develop design guidelines [21]. Proper selection of the dimensionless permeability $\tilde{K}$ (see eqn. (4.2)) based on the operating condition represented by the Richardson number Ri_L is of critical importance to design a manifold.

In the present study, a rigid porous-tube manifold with = 0.1 was constructed to provide a balanced performance between intermediate charging and top charging. The manifold is combined with an inlet diffuser. It is 1 m long, approximately 73 mm in diameter, and the ratio of permeability and wall thickness is $7.75\times10^{-8} \pm 0.39\times10^{-8}$ m/s. The dimensionless permeability $\tilde{K}$ = 0.1 for an inlet mass flow rate of 0.07 kg/s. The larger diameter of the tube relative to a conventional inlet pipe slows the inlet velocity and thus produces a buoyancy driven flow with a Richardson number of 292. During intermediate charging, the manifold ensures that water enters the tank at the level of neutral buoyancy and prevents fluid in the tank from entering the manifold. These attributes are required to avoid mixing due to plume entrainment. During top charging, the manifold eliminates the jet mixing evident in the tank when a conventional inlet pipe

is used. It performs on par with the diffuser. These results demonstrate the benefit of the rigid porous-tube stratification manifold, and support the approach previously proposed to select the dimensionless permeability.

Moving from the present laboratory demonstration of the manifold to design for practice, the same design procedure should be followed along with consideration of other important attributes such as material compatibility with hot chlorinated water, method of insertion into a pressurized tank, and the impact of mineral build in open loop systems where hard water is present.

Chapter 5

Conclusion

The benefits of thermal stratification for solar thermal systems are well understood [1,12]. Thermal stratification manifolds are required to maintain and promote stratification as conventional inlets lead to large scale mixing in the tank and are ineffective particularly under intermediate charging. In the present work, two manifold designs are evaluated. The first is the flexible porous (or fabric) manifold that was originally proposed by Loehrke et al. [4]. In the original presentation as well as in later studies by Davidson [6] and Andersen [7] the behavior of the flexible manifold was poorly explained. To address this lack of information, a mathematical model for the flexible fabric manifold was developed, coupling the processes of buoyancy-driver flow, flow through the porous manifold wall, mixing in the manifold, and the deformation of the manifold. Modeling results show that the previously held hypothesis of "pressure matching", which was largely based on laboratory observation, is incorrect (Chapter 2). The collapse of the manifold, increases rather than eliminates suction. Nevertheless, for operating conditions relevant for solar storage tanks, where buoyancy dominates the fluid motion, the deformation of the manifold has insignificant impact on the effectiveness of the manifold.

A rigid porous-tube manifold offers a simpler and more effective solution for stratification enhancement. It consists of an inlet diffuser and a rigid porous tube. In the

present study, a guideline for design of such a manifold is developed based on modeling results of the charging processes in a storage tank equipped with the porous-tube manifold (Chapter 3). The design guideline is valid over a wide range of Richardson number for both top charging and intermediate charging. For solar thermal applications, the dimensionless permeability is shown to be the key parameter for design. Recommended dimensionless permeability is established as a function of the Richardson number. For intermediate charging, a low permeability is required to eliminate suction; for top charging, a higher permeability is preferred to release the incoming fluid at the top of the tank. Selection of the permeability should consider both charging modes to achieve a balanced performance.

The use of the design guidelines is illustrated through design of a rigid porous-tube manifold for conditions representative of residential solar hot water systems. The manifold was fabricated and evaluated in a 1000-liter water storage tank. Measurements of the transient water temperatures during top and intermediate charging demonstrate enhancement of stratification compared with conventional inlets. For intermediate charging, the exergy efficiency of the manifold maintains above 0.5 after one and half hours, whereas those for diffuser and inlet pipe have reduced to 0.15 and 0, respectively. For top charging, the performance of the manifold is comparable to the best performing diffuser. Data of velocity field adjacent to the manifold outer wall shows that the behavior of the manifold is consistent to the prediction of theory, validating the proposed design guideline.

To further demonstrate the benefit of the porous-tube manifold, additional prototype testing in a solar hot water system under realistic operating conditions would

be beneficial. In addition, several practical issues, for example, selection of the porous material with respect to durability for long term application in hot water should be addressed.

The work presented herein provides a general mathematical framework of the porous manifold model that can be extended to investigate the feasibility of applying porous-tube manifolds in other storage applications, for instance, chilled water storage tanks, multiphase liquid desiccant systems, molten salt storage units in large concentrated solar thermal plants, gas storage vessels, and other storage units where it is beneficial to preserve its temperature and/or species concentration gradient (i.e. stratification).

Nomenclature

a	Thermocline thickness parameter
A	Cross-sectional area of the manifold or the tank (m^2)
A^*	Dimensionless cross-sectional area
c_p	Specific heat (J/kg/K)
D	Diameter of the manifold (m)
e_x	Specific exergy (J/kg)
E	Young's modulus (Pa) and Total exergy in the tank (J)
E_x^*	Dimensionless exergy efficiency
F	Axial stretching force (N)
$\tilde{F}$	Dimensionless axial pre-stress, $\tilde{F} = F_e \rho_{in} A_o^2 / L^2 \dot{m}_{in}^2$
g	Gravity (m/s^2)
h	Specific enthalpy (J/kg)
k	Thermal conductivity (W/m/K)
k_o	Dimensionless coefficient used in effective stiffness
k_2	Dimensionless coefficient used in effective stretching force
K	Permeability (m^2)
$\tilde{K}$	Dimensionless permeability $\tilde{K} = 2\sqrt{\pi A_o} K \dot{m}_{in} L / \mu A_o^2 \delta$
$\dot{m}$	Mass flow rate (kg/s)

$\dot{m}^*$	Dimensionless mass flow rate
M	Relative entrainment rate
p	Pressure (Pa)
Δp	Pressure drop (Pa)
P^*	Dimensionless differential pressure through the manifold wall
Pe_L	Peclet number $Pe_L = \dot{m}_{in} c_p L / A_o k_f$
r	Radial coordinate (m)
R	Radius (m)
Re_D	Reynolds number $Re_D = \rho_{in} \bar{u}_{in} D / \mu_{in}$
Ri_L	Richardson number $Ri_L = gL\beta_{in}\left(T_H - T_C\right)/U^2$
s	Entropy (J/K)
S	Stiffness of the manifold
$\tilde{S}$	Dimensionless stiffness $\tilde{S} = S\rho_{in} A_o^2 / \dot{m}_{in}^2$
t	Time (s)
T	Temperature (ºC)
u	Radial velocity (m/s)
u_D	Darcy velocity (m/s)
U	Average velocity at inlet
w	Vertical velocity (m/s)
z	Vertical coordinate (m)

z^*	Dimensionless vertical coordinate

Greek symbols

ε	Porosity
β	Thermal expansion coefficient (1/K)
δ	Manifold wall thickness (m)
μ	Dynamic viscosity (m^2/s)
ρ	Density (kg/m^3)
σ	Eccentricity factor
υ	Poisson's ratio

Subscripts

b	buckling state
c	Direct contact state
C	Cold temperature in the tank
Diffuser	Diffuser
e	Effective, Entrainment, or edge of plume
eff	Effective
H	Hot temperature in the tank
i	Inflation state or inner diameter
in	Inlet
L	Tank height
mf	Manifold

Manifold	Manifold
mix	Mixed state
o	Reference state or the outer diameter
out	Outlet
pipe	Inlet pipe
r	Radial direction
s	Solid or suction
st	Stratified state
t	Tank
up	upper boundary of thermocline
z	Vertical direction

References

[1] Hollands, K. G. T., and Lightstone, M. F., 1989, “A review of low-flow, stratified-tank solar water heating systems,” Sol. Energy, **43**(2), pp. 97–105.

[2] Han, Y. M., Wang, R. Z., and Dai, Y. J., 2009, “Thermal stratification within the water tank,” Renew. Sustain. Energy Rev., **13**(5), pp. 1014–1026.

[3] Wuestling, M. D., Klein, S. A., and Duffie, J. A., 1985, “Promising Control Alternatives for Solar Water heating Systems,” J. Sol. Energy Eng. Trans. ASME, **107**(3), pp. 215–221.

[4] Loehrke, R. I., Gari, H. N., Sharp, M. K., and Haberstroh, R. D., 1978, “A Passive Technique for Enhancing Thermal Stratification in Liquid Storage Tanks,” AIAA-ASME Thermophysics & Heat Transfer Conference, Palo Alto, Calif., p. Paper No. 78-HT-50.

[5] Gari, H. N., and Loehrke, R. I., 1982, “Controlled Buoyant Jet for Enhancing Stratification in Liquid Storage Tank,” J. Fluids Eng. Trans. ASME, **104**(4), pp. 475–481.

[6] Davidson, J. H., and Adams, D. A., 1994, “Fabric stratification manifolds for solar water heating,” J. Sol. Energy Eng. Trans. ASME, **116**(3), pp. 130–136.

[7] Andersen, E., Furbo, S., and Fan, J., 2007, “Multilayer fabric stratification pipes for solar tanks,” Sol. Energy, **81**(10), pp. 1219–1226.

[8] Andersen, E., Furbo, S., Hampel, M., Heidemann, W., and Müller-Steinhagen, H., 2008, “Investigations on stratification devices for hot water heat stores,” Int. J. Energy Res., **32**(3), pp. 255–263.

[9] Yee, C. K., and Lai, F. C., 2001, “Effects of a porous manfold on thermal stratification in a liquid storage tank,” Sol. Energy, **71**(4), pp. 241–254.

[10] Brown, N. M., and Lai, F. C., 2011, “Enhanced thermal stratification in a liquid storage tank with a porous manifold,” Sol. Energy, **85**(7), pp. 1409–1417.

[11] Pinel, P., Cruickshank, C. A., Beausoleil-Morrison, I., and Wills, A., 2011, “A review of available methods for seasonal storage of solar thermal energy in residential applications,” Renew. Sustain. Energy Rev., **15**(7), pp. 3341–3359.

[12] Han, Y. M., Wang, R. Z., and Dai, Y. J., 2009, “Thermal stratification within the water tank,” Renew. Sustain. Energy Rev., **13**(5), pp. 1014–1026.

[13] Furbo, S., Vejen, N. K., and Shah, L. J., 2005, “Thermal Performance of a Large Low Flow Solar Heating System With a Highly Thermally Stratified Tank,” J. Sol. Energy Eng., **127**(1), pp. 15–20.

[14] Andersen, E., and Furbo, S., 2007, “Theoretical comparison of solar water/space-heating combi systems and stratification design options,” J. Sol. Energy Eng. Trans. ASME, **129**(4), pp. 438–448.

[15] Zurigat, Y. H., Liche, P. R., and Ghajar, A. J., 1991, “Influence of inlet geometry on mixing in thermocline thermal energy storage,” Int. J. Heat Mass Transf., **34**(1),

pp. 115–125.
[16] Sharp, M. K., and Loehrke, R. I., 1979, “Stratified Thermal Storage in Residential Solar Energy Applications,” J Energy, **3**(2), pp. 106–113.
[17] Gari, H. N., Loehrke, R. I., and Holzer, J. C., 1979, “Performance of an Inlet Manifold for a Stratification Storage Tank,” 79-HT-67, Joint ASME/AICE 18th National Heat Transfer Conference, San Diego, Calif., Aug. 6-8, 1979.
[18] Shah, L. J., Andersen, E., and Furbo, S., 2005, “Theoretical and experimental investigations of inlet stratifiers for solar storage tanks,” Appl. Therm. Eng., **25**(14–15), pp. 2086–2099.
[19] Furbo, S., Vejen, N. K., and Shah, L. J., 2005, “Thermal performance of a large low flow solar heating system with a highly thermally stratified tank,” J. Sol. energy Eng., **127**(1), pp. 15–20.
[20] Wang, S., and Davidson, J. H., 2015, “Fluid–Structure Interaction in the Flexible Porous Stratification Manifold,” J. Sol. Energy Eng., **138**(1), p. 11005.
[21] Wang, S., and Davidson, J. H., 2015, “Selection of permeability for optimum performance of a porous tube thermal stratification manifold,” Sol. Energy, **122**, pp. 472–485.
[22] Wang, S., and Davidson, J. H., 2016, “Characterization of a Rigid Porous-tube Stratification Manifold in Comparison to Conventional Inlets,” Unpublished, under review.
[23] Whittaker, R. J., Heil, M., Jensen, O. E., and Waters, S. L., 2010, “A rational derivation of a tube law from shell theory,” Q. J. Mech. Appl. Math., **63**(4), pp. 465–496.
[24] Hazel, A. L., and Heil, M., 2003, “Steady finite-Reynolds-number flows in three-dimensional collapsible tubes,” J. Fluid Mech., (486), pp. 79–103.
[25] Wang, S., and Davidson, J. H., 2014, “Performance of Rigid Porous Stratification Manifolds With Interpretation for Off-Design Operation,” J. Sol. Energy Eng. Trans. ASME, **136**(2), p. 21021.
[26] Gari, H. N., 1983, “Stratification Enhancement in Solar Liquid Thermal Storage Tanks: Analysis and Test of Inlet Manifolds,” Colorado State University.
[27] Hughes, T. J. R., and Lubliner, J., 1973, “On the one dimensional theory of blood flow in the larger vessels,” Math. Biosci., **18**(1–2), pp. 167–170.
[28] Gebart, B. R., 1992, “Permeability of unidirectional reinforcements for RTM,” J. Compos. Mater., **26**(8), pp. 1100–1133.
[29] Belov, E. B., Lomov, S. V, Verpoest, I., Peters, T., Roose, D., Parnas, R. S., Hoes, K., and Sol, H., 2004, “Modelling of permeability of textile reinforcements: lattice Boltzmann method,” Compos. Sci. Technol., **64**(7), pp. 1069–1080.
[30] Chen, Z.-R., Ye, L., and Lu, M., 2009, “Permeability predictions for woven fabric preforms,” J. Compos. Mater.
[31] Tamayol, A., and Bahrami, M., 2011, “Transverse permeability of fibrous porous media,” Phys. Rev. E, **83**(4), p. 46314.
[32] Shapiro, A. H., 1977, “Steady Flow in Collapsible Tubes,” J Biomech Eng Tran

ASME, **99 Ser K**(3), pp. 126–147.
[33] Bertram, C. D., 2009, “Fluid flow in distensible vessels,” Clin. Exp. Pharmacol. Physiol., **36**(2), pp. 206–216.
[34] Elad, D., Sahar, M., Avidor, J. M., and Einav, S., 1992, “Steady flow through collapsible tubes: Measurements of flow and geometry,” J. Biomech. Eng., **114**(1), pp. 84–91.
[35] Kececioglu, I., McClurken, M. E., Kamm, R. D., and Shapiro, A. H., 1981, “Steady, Supercritical Flow in Collapsible Tubes -1. Experimental Observations.,” J. Fluid Mech., **109**, pp. 367–389.
[36] McClurken, M. E., Kececioglu, I., Kamm, R. D., and Shapiro, A. H., 1981, “Steady, Superctrical Flow in Collapsible Tubes - 2. Theoretical Studies.,” J. Fluid Mech., **109**, pp. 391–415.
[37] Perry, R. H., 1997, Perry’s chemical engineers’ handbook, McGraw-Hill, New York, San Francisco, Washington, D.C.
[38] Jinyun, Z., Yi, L., Lam, J., and Xuyong, C., 2010, “The Poisson Ratio and Modulus of Elastic Knitted Fabrics,” Text. Res. J., **80**(18), pp. 1965–1969.
[39] Derek B. Purchas, K. S., 2002, Handbook of Filter Media (Second Edition), Elsevier Science & Technology, Oxford.
[40] Duffie, J. A., and Beckman, W. A., 2013, Solar Engineering of Thermal Processes, John Wiley & Sons, Ltd, Hoboken, New Jersey.
[41] Lin, J.-J., 2010, Prediction of Elastic Properties of Plain Weave Fabric Using Geometrical Modeling, Woven Fabric Engineering, Polona Dobnik Dubrovski (Ed.), Sciyo.
[42] List, E. J., 1982, “Turbulent jets and plumes,” Annu. Rev. Fluid Mech., **14**(1), pp. 189–212.
[43] Turner, J. S., 1986, “Turbulent entrainment: the development of the entrainment assumption, and its application to geophysical flows,” J. Fluid Mech., **173**, pp. 431–471.
[44] Phillips, W. F., and Pate, R. A., 1977, “Mass and Energy Transfer in A Hot Liquid Energy Storage System,” Proc Annu Meet - Am Sect Int Sol Energy Soc, Orlando, Fla, p. 17–6 to 17–10.
[45] Loehrke, R. I., Holzer, J. C., Gari, H. N., and Sharp, M. K., 1979, “Stratification Enhancement in Liquid Thermal Storage Tanks.,” J. Energy, **3**(3), pp. 129–130.
[46] Brown, N. M., and Lai, F. C., 2006, “Measurement of permeability and slip coefficient of porous tubes,” J. Fluids Eng., **128**(5), pp. 987–992.
[47] Ievers, S., and Lin, W., 2009, “Numerical simulation of three-dimensional flow dynamics in a hot water storage tank,” Appl. Energy, **86**(12), pp. 2604–2614.
[48] Ma, Y., and Shishoo, R., 1999, “Permeability characterization of different architectural fabrics,” J. Compos. Mater., **33**(8), pp. 729–750.
[49] Chen, Z. R., Ye, L., and Lu, M., 2010, “Permeability Predictions for Woven Fabric Preforms,” J. Compos. Mater., **44**(13), pp. 1569–1586.
[50] Cardarelli, F., 2008, Materials Handbook, A Concise Desktop Reference,

Springer-Verlag London Limited, London.
[51] Kaviany, M., 1991, Principles of heat transfer in porous media, Springer-Verlag New York Inc., New York.
[52] COMSOL Inc., 2013, “COMSOL Multiphysics.”
[53] Beckermann, C., Ramadhyani, S., and Viskanta, R., 1987, “Natural convection flow and heat transfer between a fluid layer and a porous layer inside a rectangular enclosure,” J. Heat Transfer, **109**(2), pp. 363–370.
[54] Haller, M. Y., Cruickshank, C. A., Streicher, W., Harrison, S. J., Andersen, E., and Furbo, S., 2009, “Methods to determine stratification efficiency of thermal energy storage processes–Review and theoretical comparison,” Sol. Energy, **83**(10), pp. 1847–1860.
[55] Consul, R., Rodrıguez, I., Perez-Segarra, C. D., and Soria, M., 2004, “Virtual prototyping of storage tanks by means of three-dimensional CFD and heat transfer numerical simulations,” Sol. Energy, **77**(2), pp. 179–191.
[56] Kaloudis, E., Grigoriadis, D. G. E., Papanicolaou, E., and Panidis, T., 2013, “Large eddy simulations of turbulent mixed convection in the charging of a rectangular thermal storage tank,” Int. J. Heat Fluid Flow, **44**, pp. 776–791.
[57] Klein, S. A., 2010, “TRNSYS 17, Standard Component Library Overview,” **3**.
[58] Raman, R., Mantell, S., Davidson, J., Wu, C., and Jorgensen, G., 2000, “A review of polymer materials for solar water heating systems,” J. Sol. Energy Eng., **122**(2), pp. 92–100.
[59] O’Neill, P., Soria, J., and Honnery, D., 2004, “The stability of low Reynolds number round jets,” Exp. Fluids, **36**(3), pp. 473–483.
[60] Testfabrics Inc., 2016, “Style 864 plain weave fabric” [Online]. Available: http://www.testfabrics.com/product-detail.php?id=TVRRMA==&pid=144. [Accessed: 10-Sep-2016].

Appendix

Mathematical Derivation of the One-Dimensional Model for Rigid and Flexible Manifolds

Normally, the Reynolds transport theorem is applied to a control volume with fixed mass (i.e. the material control volume) to derive the conservation equation of mass, momentum and energy. It can also be applied to an arbitrary control volume V that fluids can pass through its boundary:

$$\begin{aligned}\frac{\mathrm{D}}{\mathrm{D}t}\int_V \phi \mathrm{d}V &= \int_V \frac{\partial \phi}{\partial t}\mathrm{d}V + \int_{\partial V} \phi \mathbf{u}\cdot\mathbf{n}\mathrm{d}a \\ &= \int_V \left[\frac{\partial \phi}{\partial t} + \nabla\cdot(\phi\mathbf{u})\right]\mathrm{d}V\end{aligned} \tag{A-1}$$

where $\mathbf{u}$ is velocity vector of the arbitrary control volume boundary ∂V . The velocity of the fluid is **v**. $\mathbf{n}$ is unit normal vector at ∂V . ϕ represents any fluid quantity.

The deviation of the governing equations of mass, momentum, and energy follows the theory of the one-dimensional flows in flexible porous tubes. Figure A-1 shows an infinitesimal small segment of a flexible tube cut between z_1 and z_2 that are invariable with respect of time.

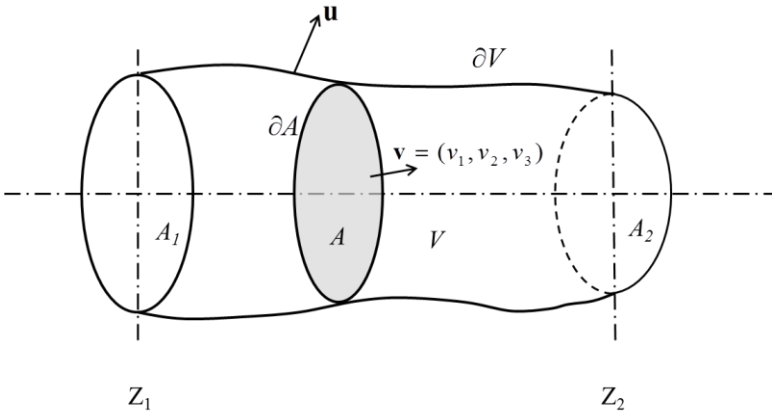

Figure A-1. An infinitesimal control volume of a segment of a flexible tube

We define $\mathbf{u}\cdot\mathbf{n} = u_n$, and the cross-sectional area averaged quantity to be $\bar{\phi} = \frac{1}{A}\int_A \phi da$.

The relative velocity **w** between the moving boundary and the fluid is defined as:

$\mathbf{w} = \mathbf{u} - \mathbf{v}$.

With above definition, the second term on the right hand side (RHS) of Eq. (A-1) can be expressed as

$$\begin{aligned}\int_{\partial V} \phi u_n \mathrm{da} &= \int_{\partial V_l + A_1 + A_2} \phi u_n \mathrm{da} \\ &= \int_{\partial V_l} \phi u_n \mathrm{da} + \int_{A_1 + A_2} \phi u_n \mathrm{da} \\ &= \int_{\partial V_l} \phi \left(w_n + v_n \right) \mathrm{da} \\ &= \int_{\partial V_l} \phi w_n \mathrm{da} + \int_{\partial V_l} \phi v_n \mathrm{da}\end{aligned} \tag{A-2}$$

Here ∂V_l represents circumferential surface of the differential segment of the tube. The surface A_1 and A_2 does not move, therefore u_n is zero on these two surfaces. Expanding

the second term on the RHS of the final expression in Eq. (A-2) and apply the divergence theorem to transform the surface integral to the volume integral,

$$\begin{aligned}\int_{\partial V_l} \phi v_n \mathrm{da} &= \int_{\partial V - A_1 - A_2} \phi v_n \mathrm{da} \\ &= \int_{\partial V} \phi v_n \mathrm{da} - \int_{A_1 + A_2} \phi v_n \mathrm{da} \\ &= \int_V \nabla \cdot (\phi \mathbf{v}) \mathrm{da} - \int_{A_1 + A_2} \phi v_n \mathrm{da}\end{aligned} \tag{A-3}$$

`Using the second fundamental theorem of calculus,

$$\begin{aligned}\int_{A_1 + A_2} \phi v_n \mathrm{da} &= \int_{A_2} \phi v_z \mathrm{da} - \int_{A_1} \phi v_z \mathrm{da} \\ &= \left(A \overline{\phi v_z} \right)_{A_2} - \left(A \overline{\phi v_z} \right)_{A_1} \\ &= \int_{z_1}^{z_2} \frac{\partial}{\partial z} \left(A \overline{\phi v_z} \right) dz\end{aligned} \tag{A-4}$$

Combining Eqs. (A1 – 4)

$$\frac{\mathrm{D}}{\mathrm{D}t} \int_V \phi \mathrm{d}V = \int_V \left(\frac{\partial \phi}{\partial t} + \nabla \cdot (\phi \mathbf{v}) \right) \mathrm{d}V + \int_{\partial V_l} \phi w_n \mathrm{da} - \int_{z_1}^{z_2} \frac{\partial}{\partial z} \left(A \overline{\phi v_z} \right) dz \tag{A-5}$$

The volume integral on the left hand side of Eq. (A-5) can be written as

$$\begin{aligned}\frac{\mathrm{D}}{\mathrm{D}t} \int_V \phi \mathrm{d}V &= \frac{D}{Dt} \int_{z_1}^{z_2} \left(A \bar{\phi} \right) dz \\ &= \int_{z_1}^{z_2} \frac{\partial}{\partial t} \left(A \bar{\phi} \right) dz\end{aligned} \tag{A-6}$$

The material derivative can be moved into the integration because z_1 and z_2 are fixed in space and time. The third term on the RHS of Eq. (A-5), which represents the convective transport through the circumferential surface ∂V_l, can also be written as an integration from z_1 to z_2.

$$\int_{\partial V_l} \phi w_n \mathrm{da} = \int_{z_1}^{z_2} \left[\oint_{\partial A} (\phi w_n) \mathrm{dl} \right] dz \tag{A-7}$$

Similarly,

$$\int_V \left[\frac{\partial \phi}{\partial t} + \nabla \cdot (\phi \mathbf{v}) \right] \mathrm{d}V = \int_{z_1}^{z_2} \left\{ \int_A \left[\frac{\partial \phi}{\partial t} + \nabla \cdot (\phi \mathbf{v}) \right] da \right\} dz \tag{A-8}$$

Combining Eqs. (A5 – 8),

$$\int_{z_1}^{z_2} \frac{\partial}{\partial t} \left(A\bar{\phi} \right) dz = \int_{z_1}^{z_2} \left\{ \int_A \left[\frac{\partial \phi}{\partial t} + \nabla \cdot (\phi \mathbf{v}) \right] da \right\} dz + \int_{z_1}^{z_2} \left[\oint_{\partial A} (\phi w_n) \, \mathrm{dl} \right] dz - \int_{z_1}^{z_2} \frac{\partial}{\partial z} \left(A\overline{\phi v_z} \right) dz \tag{A-9}$$

Therefore, the transport equation for a 1-D porous flexible channel is

$$\frac{\partial}{\partial t} \left(A\bar{\phi} \right) + \frac{\partial}{\partial z} \left(A\overline{\phi v_z} \right) = \int_A \left[\frac{\partial \phi}{\partial t} + \nabla \cdot (\phi \mathbf{v}) \right] da + \oint_{\partial A} (\phi w_n) \, \mathrm{dl} \tag{A-10}$$

Applying Eq. (A-10), the conservation equation of mass, momentum, and energy and be derived.

For mass conservation,

$$\phi = \rho \tag{A-11}$$

Substituting Eq. (A-11) into Eq. (A-10), we have

$$\frac{\partial}{\partial t} \left(A\bar{\rho} \right) + \frac{\partial}{\partial z} \left(A\overline{\rho v_z} \right) = \int_A \left[\frac{\partial \rho}{\partial t} + \nabla \cdot (\rho \mathbf{v}) \right] da + \oint_{\partial A} (\rho w_n) \, \mathrm{dl} \tag{A-12}$$

Recall for mass conservation

$$\frac{\partial \rho}{\partial t} + \nabla \cdot (\rho \mathbf{v}) = 0 \tag{A-13}$$

Hence, Eq. (A-12),

$$\frac{\partial}{\partial t} \left(A\bar{\rho} \right) + \frac{\partial}{\partial z} \left(A\overline{\rho v_z} \right) = \oint_{\partial A} (\rho w_n) \, \mathrm{dl} \tag{A-14}$$

Define the crossflow term: $\varphi = -\oint_{\partial A}\left(\rho w_n\right)\mathrm{dl}$

$$\frac{\partial}{\partial t}\left(A\bar{\rho}\right)+\frac{\partial}{\partial z}\left(A\overline{\rho v_z}\right)+\varphi = 0 \tag{A-15}$$

For conservation of momentum

$$\phi = \rho v_z \tag{A-16}$$

Substituting Eq. (A-16) into Eq. (A-10),

$$\frac{\partial}{\partial t}\left(A\overline{\rho v_z}\right)+\frac{\partial}{\partial z}\left(A\overline{\rho v_z v_z}\right)=\int_A\left[\frac{\partial\left(\rho v_z\right)}{\partial t}+\nabla\cdot\left(\rho v_z\mathbf{v}\right)\right]da+\oint_{\partial A}\left(\rho v_z w_n\right)\mathrm{dl} \tag{A-17}$$

To simplify Eq. (A-17), we recall the Navier-stokes equation for incompressible flow.

$$\frac{\partial\left(\rho\mathbf{v}\right)}{\partial t}+\nabla\cdot\left(\rho\mathbf{vv}\right)=-\nabla P+\nabla\cdot\left\{\mu\left[\nabla\mathbf{v}+\left(\nabla\mathbf{v}\right)^T\right]-\frac{2}{3}\mu\left(\nabla\cdot\mathbf{v}\right)\mathbf{I}\right\}+\rho\mathbf{g} \tag{A-18}$$

Assuming constant properties in each cross-sectional area, Eq. (A-18) in the z direction is

$$\frac{\partial\left(\rho v_z\right)}{\partial t}+\nabla\cdot\left(\rho v_z\mathbf{v}\right)=-\frac{\partial p}{\partial z}+\mu\nabla^2 v_z+\rho g_z \tag{A-18}$$

Substituting Eq. (A-19) for the integrand in the second term of the RHS of Eq. (A-17)

$$\begin{aligned}\int_A\left[\frac{\partial\rho v_z}{\partial t}+\nabla\cdot\left(\rho v_z\mathbf{v}\right)\right]da &= \int_A\left(-\frac{\partial p}{\partial z}+\mu\nabla^2 v_z+\rho g_z\right)da \\ &= -\int_A\frac{\partial p}{\partial z}da+\int_A\left[\mu\nabla\cdot\left(\nabla v_z\right)\right]da+\int_A\left(\rho g_z\right)da \\ &= -A\frac{\partial\bar{p}}{\partial z}+\int_{\partial A}\mu\nabla v_z\cdot\mathbf{n}dl+\int_A\mu\frac{d^2 v_z}{dz^2}da+A\bar{\rho}g_z\end{aligned} \tag{A-20}$$

And apply the divergence theorem for surface integral.

$$
\begin{aligned}
\int_A \left[\mu\nabla\cdot\left(\nabla v_z\right)\right] da &= \frac{1}{dz}\left\{dz\int_A\left[\mu\nabla\cdot\left(\nabla v_z\right)\right]da\right\} \\
&= \frac{1}{dz}\int_V\left[\mu\nabla\cdot\left(\nabla v_z\right)\right]dv \\
&= \frac{1}{dz}\int_A \mu\nabla v_z\cdot\mathbf{n}da \\
&= \frac{1}{dz}\left(\int_{A_{side}}\mu\nabla v_z\cdot\mathbf{n}da+\int_{A^+ + A^-}\mu\nabla v_z\cdot\mathbf{n}da\right) \\
&= \lim_{dz\to\infty}\left[\frac{\mu}{dz}\int_{A_{side}}\nabla v_z\cdot\mathbf{n}da+\int_A\frac{\mu}{dz}\left(\left.\frac{dv_z}{dz}\right|_{z+dz}-\left.\frac{dv_z}{dz}\right|_z\right)da\right] \\
&= \int_{\partial A}\mu\nabla v_z\cdot\mathbf{n}dl+\int_A\mu\frac{d^2v_z}{dz^2}da
\end{aligned}
\qquad \text{(A-21)}
$$

Hence the 1D momentum conservation equation in the conservative form is

$$
\frac{\partial}{\partial t}\left(A\overline{\rho v_z}\right)+\frac{\partial}{\partial z}\left(A\overline{\rho v_z v_z}\right)+A\frac{\partial\overline{p}}{\partial z}=\oint_{\partial A}\mu\left(\nabla v_z\cdot\mathbf{n}\right)dl+\int_A\mu\frac{d^2v_z}{dz^2}da+A\overline{\rho}g_z+\oint_{\partial A}\left(\rho v_z w_n\right)\mathrm{dl}
\qquad \text{(A-22)}
$$

The LHS of above equation can be simplified to the non-conservative form using the mass conservation equation derived in Eq. (A-15).

$$
\begin{aligned}
\frac{\partial}{\partial t}\left(A\overline{\rho v_z}\right)+\frac{\partial}{\partial z}\left(A\overline{\rho v_z v_z}\right) &= \frac{\partial}{\partial t}\left(A\bar{\rho}\bar{v}_z\right)+\frac{\partial}{\partial z}\left(A\bar{\rho}\overline{v_z v_z}\right) \\
&= \frac{\partial}{\partial t}\left(A\bar{\rho}\bar{v}_z\right)+\frac{\partial}{\partial z}\left(A\bar{\rho}\overline{\left(v_z\right)^2}\right)-\frac{\partial}{\partial z}\left(A\bar{\rho}\left(\bar{v}_z\right)^2\right)+\frac{\partial}{\partial z}\left(A\bar{\rho}\left(\bar{v}_z\right)^2\right) \\
&= A\bar{\rho}\frac{\partial}{\partial t}\left(\bar{v}_z\right)+\bar{v}_z\frac{\partial}{\partial t}\left(A\bar{\rho}\right)+\frac{\partial}{\partial z}\left[A\bar{\rho}\left(\bar{v}_z\right)^2\right]+\frac{\partial}{\partial z}\left\{A\bar{\rho}\left[\overline{\left(v_z\right)^2}-\left(\bar{v}_z\right)^2\right]\right\} \\
&= A\bar{\rho}\frac{\partial}{\partial t}\left(\bar{v}_z\right)+\bar{v}_z\frac{\partial}{\partial t}\left(A\bar{\rho}\right)+\bar{v}_z\frac{\partial}{\partial z}\left[A\bar{\rho}\bar{v}_z\right]+A\bar{\rho}\bar{v}_z\frac{\partial}{\partial z}\left(\bar{v}_z\right)+\frac{\partial}{\partial z}\left\{A\bar{\rho}\left[\overline{\left(v_z\right)^2}-\left(\bar{v}_z\right)^2\right]\right\} \\
&= A\bar{\rho}\left[\frac{\partial}{\partial t}\left(\bar{v}_z\right)+\left(\bar{v}_z\right)\frac{\partial}{\partial z}\left(\bar{v}_z\right)\right]-\bar{v}_z\varphi+\frac{\partial}{\partial z}\left\{A\bar{\rho}\left[\overline{\left(v_z\right)^2}-\left(\bar{v}_z\right)^2\right]\right\} \\
&= A\bar{\rho}\left[\frac{\partial}{\partial t}\left(\bar{v}_z\right)+\left(\bar{v}_z\right)\frac{\partial}{\partial z}\left(\bar{v}_z\right)\right]+\frac{\partial}{\partial z}\left\{A\bar{\rho}\left[\overline{\left(v_z\right)^2}-\left(\bar{v}_z\right)^2\right]\right\}+\bar{v}_z\oint_{\partial A}\left(\rho w_n\right)\mathrm{dl} \\
&= A\bar{\rho}\left[\frac{\partial}{\partial t}\left(\bar{v}_z\right)+\left(\bar{v}_z\right)\frac{\partial}{\partial z}\left(\bar{v}_z\right)\right]+\frac{\partial}{\partial z}\left\{A\bar{\rho}\left[\overline{\left(v_z\right)^2}-\left(\bar{v}_z\right)^2\right]\right\}+\oint_{\partial A}\left(\rho\overline{v_z w_n}\right)\mathrm{dl}
\end{aligned}
\tag{A-23}
$$

Combining Eq. (A-23) with Eq. (A-22),

$$
\begin{aligned}
&\bar{\rho}\left[\frac{\partial}{\partial t}\left(\bar{v}_z\right)+\bar{v}_z\frac{\partial}{\partial z}\left(\bar{v}_z\right)\right]+\frac{1}{A}\frac{\partial}{\partial z}\left\{A\bar{\rho}\left[\overline{\left(v_z\right)^2}-\left(\bar{v}_z\right)^2\right]\right\}+\frac{\partial\bar{p}}{\partial z} \\
&=\frac{1}{A}\oint_{\partial A}\left[\mu\nabla v_z\cdot\mathbf{n}+\rho w_n\left(v_z-\bar{v}_z\right)\right]dl+\int_A\mu\frac{d^2v_z}{dz^2}da+\bar{\rho}g_z
\end{aligned}
\tag{A-24}
$$

Following similar procedure, to obtain the energy conservation equation, we define

$$
\phi=\rho\left(e+\frac{1}{2}\mathbf{v}\cdot\mathbf{v}\right) \tag{A-25}
$$

where *e* is the internal energy carried by the fluid, and $\mathbf{v}\cdot\mathbf{v}/2$ is the kinetic energy.

$$\frac{\partial}{\partial t}\left[\overline{A\rho\left(e+\frac{1}{2}\mathbf{v}\cdot\mathbf{v}\right)}\right]+\frac{\partial}{\partial z}\left[\overline{A\rho\left(e+\frac{1}{2}\mathbf{v}\cdot\mathbf{v}\right)v_z}\right]$$
$$=\int_A\left\{\frac{\partial\rho\left(e+\frac{1}{2}\mathbf{v}\cdot\mathbf{v}\right)}{\partial t}+\nabla\cdot\left[\rho\left(e+\frac{1}{2}\mathbf{v}\cdot\mathbf{v}\right)\mathbf{v}\right]\right\}da+\oint_{\partial A}\left[\rho\left(e+\frac{1}{2}\mathbf{v}\cdot\mathbf{v}\right)w_n\right]\mathrm{dl} \quad \text{(A-26)}$$

The first term on the RHS of the Eq. (A-26) can be substituted using the general energy conservation equation for incompressible flow without heat generation as follows

$$\frac{\partial}{\partial t}\left(\rho e+\frac{1}{2}\rho v_j v_j\right)+\frac{\partial}{\partial x_k}\left[\left(\rho e+\frac{1}{2}\rho v_j v_j\right)v_k\right]=\frac{\partial}{\partial x_i}\left(v_j\sigma_{ij}\right)+v_j\rho g_j-\frac{\partial q_j}{\partial x_j} \quad \text{(A-27)}$$

and

$$\int_A\left\{\frac{\partial\rho\left(e+\frac{1}{2}\mathbf{v}\cdot\mathbf{v}\right)}{\partial t}+\nabla\cdot\left[\rho\left(e+\frac{1}{2}\mathbf{v}\cdot\mathbf{v}\right)\mathbf{v}\right]\right\}da$$
$$=\int_A\left[\nabla\cdot\left(\mathbf{v}\cdot\boldsymbol{\sigma}\right)+\rho\mathbf{v}\cdot\mathbf{g}-\nabla\cdot\mathbf{q}\right]da \quad \text{(A-28)}$$
$$=\int_A\left(\rho\mathbf{v}\cdot\mathbf{g}\right)da+\oint_{\partial A}\left(\mathbf{v}\cdot\boldsymbol{\sigma}\cdot\mathbf{n}\right)dl-\oint_{\partial A}\left(\mathbf{q}\cdot\mathbf{n}\right)dl-\int_A\frac{dq_n}{dz}da$$
$$=\int_A\left(\rho\mathbf{v}\cdot\mathbf{g}\right)da-\oint_{\partial A}\left(\mathbf{v}\cdot P\mathbf{n}\right)dl+\oint_{\partial A}\left(\mathbf{v}\cdot\boldsymbol{\tau}\cdot\mathbf{n}\right)dl-\oint_{\partial A}\left(\mathbf{q}\cdot\mathbf{n}\right)dl-\int_A\frac{dq_n}{dz}da$$

Replacing Eq. (A-28) for the first term on the RHS of Eq. (A-26), the 1D energy equation is

$$\frac{\partial}{\partial t}\left[\overline{A\rho\left(e+\frac{1}{2}\mathbf{v}\cdot\mathbf{v}\right)}\right]+\frac{\partial}{\partial z}\left[\overline{A\rho\left(e+\frac{1}{2}\mathbf{v}\cdot\mathbf{v}\right)v_z}\right]$$
$$=\int_A(\rho\mathbf{v}\cdot\mathbf{g})\,da-\oint_{\partial A}(\mathbf{v}\cdot p\mathbf{n})dl+\oint_{\partial A}(\mathbf{v}\cdot\boldsymbol{\tau}\cdot\mathbf{n})dl \qquad \text{(A-29)}$$
$$-\oint_{\partial A}(\mathbf{q}\cdot\mathbf{n})dl-\int_A\frac{dq_n}{dz}\,da+\oint_{\partial A}\left[\rho\left(e+\frac{1}{2}\mathbf{v}\cdot\mathbf{v}\right)w_n\right]_{\mathrm{w}}\ \mathrm{dl}$$

The terms on the RHS represent gravitational work, pressure work, viscous dissipation, heat flux though the circumferential boundary, axial conduction, and convection (cross-flow) through the circumferential boundary.

In summary, Eqs. (A-15, A-22, A-29) are the governing equations for mass, momentum, and energy for 1-D flows in flexible porous channels.

1-D model for flexible porous manifolds

The 1-D model for flexible porous manifolds is steady state. The flow direction and gravity direct are aligned with z-axis. In addition, the velocity, pressure, and temperature are uniform within each cross-section. The Boussinesq approximation is employed.

Employing the Darcy's law for the crossflow (flow in the radial direction),

$$\begin{aligned} w_n &= u_n - v_n \\ &= 0 - v_n \\ &= -\frac{K}{\mu}\frac{(p-p_t)}{\delta} \\ &= -\frac{K}{\mu}\frac{\Delta p}{\delta} \end{aligned} \qquad \text{(A-30)}$$

Here p is the pressure inside the manifold and p_t is the pressure in the tank. K is the permeability of the manifold and δ is the wall thickness. The positive direction of the

radial flow is normal to the outer surface of the manifold (i.e. leaving the manifold). Assuming the radial flow is uniform circumferentially, the mass conservation in the flow direction *z* is

$$\frac{d}{dz}\left(A\rho_{in}v_z\right)=\oint_{\partial A}\left(\rho w_n\right)\mathrm{dl}=-2\sqrt{\pi A}\,\frac{\rho_{in}K}{\mu}\,\frac{\Delta p}{\delta} \tag{A-31}$$

Written in terms of the axial mass flow rate ($\dot{m}=A\rho_{in}v_z$)

$$\frac{d\dot{m}}{dz}=-2\sqrt{\pi A}\,\frac{\rho_{in}K}{\mu}\,\frac{\Delta p}{\delta} \tag{A-32}$$

The momentum conservation equation (Eq. (A-22)) can be simplified to

$$\rho_{in}v_z\frac{\partial}{\partial z}v_z+\frac{\partial p}{\partial z}=\frac{1}{A}\oint_{\partial A}\left[\mu\frac{\partial v_z}{\partial z}\mathbf{e}_z\left(0,0,1\right)\cdot\mathbf{n}\left(x,y,0\right)\right]dl+\rho_{in}g \tag{A-33}$$

and

$$\rho_{in}v_z\frac{d}{dz}v_z+\frac{dp}{dz}=\rho_{in}g \tag{A-34}$$

In the tank, the hydrostatic pressure obeys following equation

$$\frac{dp_t}{dz}=\rho_t gz \tag{A-35}$$

Combining Eqs. (A-34 and A-35), and substitute v_z with $\dot{m}$,

$$\frac{d\Delta p}{dz}=\left(\rho-\rho_t\right)g-\frac{\dot{m}}{\rho_{in}A^2}\frac{d\dot{m}}{dz}+\frac{\dot{m}^2}{\rho_{in}A^3}\frac{dA}{dz} \tag{A-36}$$

For the energy conservation equation in this application, the only significant term on the RHS of Eq. (A-29) is the internal energy flux term represents the radial flow. However, for the axial conduction is included to raise the order of the equation, so that additional

boundary condition can be applied, allowing a more convenient numerical scheme. Thus, Eq. (A-29) can be simplified to

$$\frac{\partial}{\partial z}\left(A\rho_{in}ev_z\right)=\begin{cases}-\int_A \frac{d\dot{q}_n''}{dz}da+\oint_{\partial A}\left(\rho_{in}ew_n\right)\mathrm{dl}, & \Delta p<0\\ -\int_A \frac{d\dot{q}_n''}{dz}da, & \Delta p\geq 0\end{cases} \tag{A-37}$$

For incompressible fluid, $e = c_p T$. The heat flux term in the axial direction is

$$\dot{q}_n''=-k_f\frac{dT}{dz} \tag{A-38}$$

Again, rewrite the energy conservation equation in terms of axial flow rate,

$$\frac{dT}{dz}=\begin{cases}\frac{Ak_f}{\dot{m}c_p}\frac{d^2T}{dz^2}, & \Delta p\geq 0\\ -\frac{\left(T-T_t\right)}{\dot{m}}\frac{d\dot{m}}{dz}+\frac{Ak_f}{\dot{m}c_p}\frac{d^2T}{dz^2}, & \Delta p<0\end{cases} \tag{A-39}$$

Finally, the functional relationship between the cross-sectional area A and the differential pressure Δp is described by the "tube law".

$$\Delta p=\mathrm{P}\left(A\right)-F_o\frac{d^2A}{dz^2} \tag{A-40}$$

where P(A) is the local tube law that governs the transvers deformation of the manifold. F_o is the axial pre-stretching force.

In summary, Eqs. (A-32, A-36, A-39, A-40) is the 1-D model for the flexible porous manifold that consists of conservation of mass, momentum, energy, and the tube law.

1-D model for rigid porous manifolds

The 1-D model for rigid porous manifold with hydraulic resistance element can also be obtained from this framework.

If the porous wall for the rigid manifold is made of perforation, the equation for flow through orifice plate is more appropriate in determining the radial flow rate. Thus,

$$A\frac{\partial}{\partial z}\left(\rho_{in}v_z\right) = -\oint_{\partial A}\left[\rho_{in}\left(C_D\sqrt{2\frac{\left(p-p_t\right)}{\rho_{in}}}\right)\right]\mathrm{dl} = -\varepsilon\pi DC_D\sqrt{2\rho_{in}\Delta p} \tag{A-41}$$

where ε is the surface porosity (i.e. open area/total surface area). C_D is the loss coefficient for the orifice. In terms of axial flow rate.

$$\frac{d\dot{m}}{dz} = -\varepsilon\pi DC_D\sqrt{2\rho_{in}\Delta p} \tag{A-42}$$

The momentum conservation equation is similar to Eq. (A-36) expect that the term represents the change of A is dropped, and the additional pressure drop due to hydraulic resistance is added.

$$\frac{d\Delta p}{dz} = \left(\rho-\rho_t\right)g - \frac{\dot{m}}{\rho_{in}A^2}\frac{d\dot{m}}{dz} - \frac{2f\dot{m}^2}{\rho_{in}DA^2} \tag{A-43}$$

where f is the equivalent Fanning friction coefficient.

For the energy conservation equation, if the axial conduction is neglected,

$$\frac{dT}{dz} = \begin{cases} 0, & \Delta p > 0 \\ \dfrac{T_t - T}{\dot{m}}\dfrac{d\dot{m}}{dz}, & \Delta p \le 0 \end{cases} \tag{A-44}$$

Proof of Eq. (A-1)

The validation of Eq. A-1 can be proved as following: the total amount of change for an arbitrary quantity $\phi(\mathbf{x},t)$ within V can be expressed as $\frac{\mathrm{D}}{\mathrm{D}t}\int_V \phi \mathrm{d}V$. At initial time t = 0, the original position of an observer on the moving boundary is at ξ, and the position of the observer at any time is $\mathbf{x}(\xi,t)$, which is a function of the original position ξ, and time t. The original volume is $V_o(\xi)$.

$$
\begin{aligned}
\frac{\mathrm{D}}{\mathrm{D}t}\int_V \phi(\mathbf{x},t)\,\mathrm{d}V &= \frac{\mathrm{D}}{\mathrm{D}t}\int_{V_{o,\xi}} \phi(\xi,t)\,J_\xi \mathrm{d}V_{o,\xi} \\
&= \int_{V_{o,\xi}} \frac{\mathrm{D}}{\mathrm{D}t}\left[\phi(\xi,t)\,J_\xi\right]\mathrm{d}V_{o,\xi} \\
&= \int_{V_{o,\xi}} J_\xi \frac{\mathrm{D}}{\mathrm{D}t}\phi(\xi,t)+\phi(\xi,t)\frac{\mathrm{D}}{\mathrm{D}t}J_\xi \mathrm{d}V_{o,\xi} \\
&= \int_{V_{o,\xi}} \left\{ J_\xi\left(\frac{\partial}{\partial t}\phi(\xi,t)+\mathbf{u}\cdot\nabla\phi(\xi,t)\right)+\phi(\xi,t)\,J_\xi\nabla\cdot\mathbf{u}\right\}\mathrm{d}V_{o,\xi} \\
&= \int_{V_{o,\xi}} \left\{\frac{\partial}{\partial t}\phi(\xi,t)+\nabla\cdot\left[\phi(\xi,t)\mathbf{u}\right]\right\} J_\xi \mathrm{d}V_{o,\xi} \\
&= \int_V \left\{\frac{\partial}{\partial t}\phi(\xi,t)+\nabla\cdot\left[\phi(\xi,t)\mathbf{u}\right]\right\}\mathrm{d}V
\end{aligned}
\tag{A-45}
$$